

**Phase separation of biomimetic
membranes:
Influence of glycosphingolipid structure
and substrate adhesion**

Dissertation

for the award of the degree

Doctor rerum naturalium

of the Georg-August University Göttingen

within the doctoral program

Chemistry of the Georg-August University School of Science (GAUSS)

submitted by

Jeremias Sibold

from Donaueschingen

Göttingen 2019

Members of the Thesis Committee:

Prof. Dr. Claudia Steinem (Reviewer),
Institute of Organic and Biomolecular Chemistry,
Georg-August University Göttingen

Prof. Dr. Jörg Enderlein,
Third Institute of Physics,
Georg-August University Göttingen

Members of the Examination Board:

Prof. Dr. Claudia Steinem (Reviewer),
Institute of Organic and Biomolecular Chemistry,
Georg-August University Göttingen

Prof. Dr. Jörg Enderlein,
Third Institute of Physics,
Georg-August University Göttingen

Further members of the Examination Board:

apl. Prof. Dr. Burkhard Geil,
Institute of Physical Chemistry,
Georg-August University Göttingen

Prof. Dr. Marcus Müller,
Institute for Theoretical Physics,
Georg-August University Göttingen

apl. Prof. Dr. Bert L. de Groot,
Institute for Computational Biomolecular Dynamics,
Max Planck Institute for Biophysical Chemistry

Prof. Dr. Sarah Köster,
Institute for X-Ray Physics,
Georg-August University Göttingen

Date of oral examination:

14.10.2019

Declaration

I, Jeremias Sibold, hereby certify, that this thesis has been written independently and there was no use of other sources than quoted.

Göttingen, 2019

Jeremias Sibold

- *Meiner Familie* -

„Verzicht auf Denken ist geistige Bankrotterklärung.“

Albert Schweizer

Abstract

The bacterium enterohemorrhagic *Escherichia coli* (EHEC) is one of the main causes of food borne illness. The toxin of this bacteria is shiga toxin (STx) which inhibits the protein biosynthesis of cells. Approaching the cells B-subunit of STx (STxB) binds to the receptor lipid globotriaosyl ceramide (Gb₃) which is heterogeneous distributed in the outer membrane of human cells. Such a cellular membrane is itself very heterogeneous and has regions of higher and lower ordering which influences Gb₃ distribution. Furthermore, the cellular membrane is heterogeneously connected either to the cytoskeleton in the inside or to the surfaces on the outside of the cell, inducing different adhesional properties in the cell membrane (adhered membranes and non-adhered membranes). As postulated in a theory of Lipowsky *et al.*^[1] this is assumed to influence ordering and lipid distribution in lipid membranes.

In this work, the phase distribution of the Gb₃ is analyzed in biomimetic model membranes as a function of the creamide backbone harboring different fatty acids. Fatty acid labeled Gb₃s showed unnatural phase preference of STxB Gb₃ binding. Fluorescently head group labeled Gb₃s were investigated to study the influence of different fatty acids in liquid ordered (l_o)/liquid disordered (l_d) phase-separated giant unilamellar vesicles. Gb₃s with the saturated fatty acid is preferentially distributed in the l_o phase, while the Gb₃s with the unsaturated fatty acid prefer the l_d phase. An α -hydroxylation at the fatty acid had no effect of the distribution of Gb₃. In contrast different sphingomyelins (SMs) influence the partitioning of Gb₃.

The influence of heterogeneous membrane adhesion to biomimic membranes was analyzed using pore-spanning membranes (PSMs) on SiO_x functionalized substrates. The heterogeneous membrane adhesion influences the measured phase diagram. A membrane composed of DOPC/SM/cholesterol (Chol) (1:1:2) is still phase-separated with the l_d phase in the solid supported PSM (s-PSM) and the l_o phase in the freestanding PSM (f-PSM). Phase diagrams of homogeneous membrane adhesion were reported to have no phase separation at the same Chol content which verifies the theory of Lipowsky *et al.*^[1] for the analyzed lipid compositions.

Abbreviations

²H-NMR	deuterium nuclear magnetic resonance
AFM	atomic force microscopy
ATTO488-DOPE	ATTO488-1,2-dioleoyl- <i>sn</i> -glycero-3-phosphoethanolamin
ATTO488-DPPE	ATTO488-1,2-dipalmitoyl- <i>sn</i> -glycero-3-phosphoethanolamin
ATTO532-DOPE	ATTO532-1,2-dioleoyl- <i>sn</i> -glycero-3-phosphoethanolamin
ATTO647N-DOPE	ATTO647N-1,2-dioleoyl- <i>sn</i> -glycero-3-phosphoethanolamin
ATTO655-DOPE	ATTO655-1,2-dioleoyl- <i>sn</i> -glycero-3-phosphoethanolamin
BODIPY	boron-dipyrromethene
BODIPY 500/510-PC	2-(4,4-difluoro-5-octyl-4-bora-3a,4a-diaza- <i>s</i> -indacene-3-pentanoyl)-1-hexadecanoyl- <i>sn</i> -glycero-3-phosphocholine
BODIPY-Chol	23-(dipyrrometheneboron difluoride)-24-norcholesterol
BODIPY-PC	2-(4,4-difluoro-5,7-dimethyl-4-bora-3a,4adiaza- <i>s</i> -indacene-3-pentanoyl)-1-hexadecanoyl- <i>sn</i> -glycero-3-phosphocholine
BSA	bovine serum albumin
cb-DOPE	1,2-dioleoyl- <i>sn</i> -glycero-3-phosphoethanolamine-N-cap-biotinyl
Chol	cholesterol
CLSM	confocal laser scanning microscope
CPEO3	<i>O</i> -cholesteryl <i>N</i> -(8'-mercapto-3',6'-dioxaoctyl)carbamate
CTx	cholera toxin
CTxB	B-subunit of cholera toxin
CVE	covariance-based estimation
Cy3	cyanine dye 3
<i>D</i>	diffusion coefficient
DiD-C₁₈	DiOctadecyl-3,3,3',3'-tetramethylindodicarbocyanine perchlorate
DiI-C₁₈	1,1'dioctadecyl-3,3,3',3'-tetramethylindodicarbocyanine perchlorate
DLPC	1,2-dilauroyl- <i>sn</i> -glycero-3-phosphatidylcholine

DMPC	1,2-dimiristeoyl- <i>sn</i> -glycero-3-phosphatidylcholine
DOPC	1,2-dioleoyl- <i>sn</i> -glycero-3-phosphatidylcholine
DOPE	1,2-dioleoyl- <i>sn</i> -glycero-3-phosphatidylethanolamine
DPhPC	1,2-diphytanoyl- <i>sn</i> -glycero-3-phosphatidylcholine
DPPC	1,2-dipalmitoyl- <i>sn</i> -glycero-3-phosphatidylcholine
DPPE	1,2-dipalmitoyl- <i>sn</i> -glycero-3-phosphatidylethanolamine
DPPE-KK114	KK114-1,2-dipalmitoyl- <i>sn</i> -glycero-3-phosphoethanolamin
DRM	detergent resistant membrane
DSC	differential scanning calorimetry
DSPE	1,2-stearoyl- <i>sn</i> -glycero-3-phosphatidylethanolamine
DSPE-KK114	KK114-1,2-distearoyl- <i>sn</i> -glycero-3-phosphoethanolamin
DSPE-PEG-KK114	KK114-PEG ₄₅ -1,2-distearoyl- <i>sn</i> -glycero-3-phosphoethanolamin
Dy731-DOPE	Dy731-PEG ₂₅ -1,2-dioleoyl- <i>sn</i> -glycero-3-phosphoethanolamin
EHEC	enterohemorrhagic <i>Escherichia coli</i>
FCS	fluorescence correlation spectroscopy
f-PSM	freestanding pore-spanning membrane
FRAP	fluorescence recovery after photobleaching
FRET	fluorescence resonance energy transfer
GalCer	galactosylceramide
Gb₃PH	globotriaosyl ceramid phenyl-modified fatty acid
Gb₃porc	porcine erythrocytes globotriaosyl ceramide
Gb₃TT	globotriaosyl ceramid thienothienyl-modified fatty acid
Gb₃	globotriaosyl ceramide
Gb₃PEG₁₃C_{24:0}H	BODIPY labeled lignoceroyl globotriaosyl ceramid with 13 PEG units
Gb₃PEG₁₃C_{24:0}OH	BODIPY labeled 2-R-hydroxyl-lignoceroyl globotriaosyl ceramid with 13 PEG units
Gb₃PEG₁₃C_{24:1}H	BODIPY labeled lignoceroyl nervonoyl ceramid with 13 PEG units
Gb₃PEG₁₃C_{24:1}OH	BODIPY labeled 2-R-hydroxyl-nervonoyl globotriaosyl ceramid with 13 PEG units
Gb₃PEG₃C_{24:0}H	BODIPY labeled lignoceroyl globotriaosyl ceramid with 3 PEG units
Gb₃PEG₃C_{24:0}OH	BODIPY labeled 2-R-hydroxyl-lignoceroyl globotriaosyl ceramid with 3 PEG units

Gb₃PEG₃C_{24:1}H	BODIPY labeled lignoceroyl nervonoyl ceramid with 3 PEG units
Gb₃PEG₃C_{24:1}OH	BODIPY labeled 2-R-hydroxyl-nervonoyl globotriaosyl ceramid with 3 PEG units
GM₁	pentasaccharide ganglioside
GNP	gold nano particle
GPMV	giant plasma-membrane vesicle
GUV	giant unilamellar vesicle
HeLa cells	cervical cancer cells from Henrietta Lacks ^[2]
HUS	haemolytic uraemic syndrome
iSCAT	interferometric scattering microscopy
ITO-slide	Indium Tin Oxide coated slide
K_d	dissociation constant
laser	light amplification by stimulated emission of radiation
l_β	gel like
l_d	liquid disordered
LED	light-emitting diode
L-scan FCS	line-scan fluorescence correlation spectroscopy
LMM	linear mixed-effects model
l_o	liquid ordered
%l_o	liquid ordered phase distribution
LUV	large unilamellar vesicle
MD	molecular dynamics simulation
12MDD	12-mercapto-1-dodecanol
2ME	2-mercapto-1-ethanol
2ME-Au	2-mercapto-1-ethanol on gold
6MH	6-mercapto-1-hexanol
6MH-Au	6-mercapto-1-hexanol on gold
16MHD	16-mercapto-1-hexadecanol
16MHD-Au	16-mercapto-1-hexadecanol on gold
MLV	multi-lamellar vesicle
8MO	8-mercapto-1-octanol
8MO-Au	8-mercapto-1-octanol on gold
11MUD	11-mercapto-1-undecanol
11MUD-Au	11-mercapto-1-undecanol on gold
N	numbers of measurements
naphthopyrene	naphtho[2,3-a]pyrene

NBD	7-nitrobenz-2-oxa-1,3-diazol-4-yl
OT	octan-1-thiol
OT-Au	octan-1-thiol on gold
PBS	phosphate-buffered saline
PC	phosphatidylcholine
PE	phosphatidylethanolamine
PEG	polyethylene glycol
pHBMEC	primary human blood microvascular endothelial cells
PIP	phosphatidylinositolphosphate
POPC	1-palmitoyl-2-oleoyl- <i>sn</i> -glycero-3-phosphatidylcholine
POPE	1-palmitoyl-2-oleoyl- <i>sn</i> -glycero-3-phosphatidylethanolamine
POPS	1-palmitoyl-2-oleoyl- <i>sn</i> -glycero-3-phosphatidy-L-serine
PS	phosphatidylserine
PSF	point spread function
p-Si₃N₄	plasma cleaned silicon nitride
PSM	pore-spanning membrane
QI	quantitative imaging
Rhod-DOPE	1,2-dioleoyl- <i>sn</i> -glycero-3-phosphoethanolamine-N-(lissamine rhodamine B sulfonyl)
SAM	self-assembled monolayer
SEM	scanning electron microscopy
Si₃N₄	silicon nitride
σ	membrane tension
SiO	silicon monoxide
SiO₂	silicon dioxide
SiO_x	silicon oxide
SM	sphingomyelin
SM C_{16:0}	palmitoyl sphingomyelin
SM C_{18:0}	stearoyl sphingomyelin
SM C_{20:0}	arachidoyl sphingomyelin
SM C_{22:0}	behenoyl sphingomyelin
SM C_{24:0}	lignoceroyl sphingomyelin
SM C_{24:1}	nervonoyl sphingomyelin
SM_{egg}	egg sphingomyelin
SM_{porc}	porcine brain sphingomyelin
SPR	surface plasmon resonance
s-PSM	solid supported pore-spanning membrane

SPT	single particle tracking
SSM	solid supported membrane
STx	shiga toxin
STxA	A-subunit of shiga toxin
STxB	B-subunit of shiga toxin
SUV	small unilamellar vesicle
<i>T</i>	temperature
TexasRed-DHPE	sulforhodamine-1,2-dihexanoyl- <i>sn</i> -glycero-3-phosphoethanolamine
T_M	transition temperature
Triton X-100	polyethylene glycol p-(1,1,3,3-tetramethylbutyl)-phenyl ether
UK	United Kingdom
US	United States
UV	ultraviolet light
vis	visible light
Z-scan FCS	Z-scan fluorescence correlation spectroscopy

Table of contents

Abstract	i
Abbreviations	iii
1. Introduction	1
1.1. Enterohemorrhagic <i>Escherichia coli</i>	1
1.2. Shiga toxin	2
1.3. Cell membranes and their properties	5
2. Scope of the thesis	9
3. Materials and methods	11
3.1. Used materials	11
3.1.1. Matrix lipids	11
3.1.2. Membrane fluorescent probes	13
3.1.3. Globotriaosyl ceramide	16
3.1.4. B-subunit of shiga toxin	18
3.2. Preparative methods	19
3.2.1. Preparation of vesicles	19
3.2.2. Functionalization of porous substrates	21
3.2.3. Preparation of pore-spanning membranes (PSMs)	22
3.3. Biophysical methods	23
3.3.1. Fluorescence microscopy	23
3.3.2. Interferometric scattering microscopy	26
3.3.3. Atomic force microscopy	27
3.3.4. Surface plasmon resonance	28
3.4. Data evaluation	30
3.4.1. Phase distribution in GUVs	30
3.4.2. Phase separation on PSMs	32
4. Phase behavior of globotriaosyl ceramide (Gb₃)	37
4.1. Binding studies of STxB to its receptor lipid Gb ₃	37

4.2.	Analysis of the phase preference of labeled Gb ₃ s	40
4.2.1.	Fluorescent properties of labeled Gb ₃ s	41
4.2.2.	Preference of fatty acid labeled Gb ₃ s in phase-separated GUVs	46
4.2.3.	Preference of head group labeled Gb ₃ s in phase-separated GUVs	49
4.3.	Conclusion of phase behavior of Gb ₃	61
5.	Pore-spanning membranes (PSMs)	63
5.1.	Different functionalization strategies and their effects on PSMs . . .	64
5.1.1.	Visualization of PSMs	65
5.1.2.	Membrane tension modulation of PSMs	71
5.1.3.	Diffusion in PSMs	76
5.2.	Phase separation in PSMs	82
5.3.	Conclusion of PSMs	91
6.	Conclusion	93
7.	References	95
A.	Appendix	123
A.1.	List of figures	123
A.2.	List of schemes	124
A.3.	List of tables	125
A.4.	Lipid diffusion constants	126
A.5.	Membrane tension of pore-spanning membranes	128
A.6.	Fluorescence labeled Gb ₃	129
A.7.	Statistical analyses	130
A.7.1.	Statistical analysis of fatty acid labeled Gb ₃	130
A.7.2.	Statistical analysis of head group labeled Gb ₃	131
A.7.3.	Statistical analysis of Membrane tension	133
A.8.	Chemicals and consumables	135
A.9.	Software	137
A.10.	Equipment	137

1. Introduction

1.1. Enterohemorrhagic *Escherichia coli*

Enterohemorrhagic *Escherichia coli* (EHEC) is a bacterial strain, which triggers many outbreaks around the world, including industrialized nations.^[3-6] This bacterial strain was found in 1977 and the toxin was called vero toxin, a toxin that destroyed the vero cells.^[7] EHEC became prominent in the 1980s, namely with large scale outbreaks in the United States (US) from the EHEC-strain O157:H7 in 1982.^[8] In 1996, EHEC was prominent in Japan with 9451 infected people.^[3] In 2006, there was again a large outbreak in the US which involved 26 states.^[9] Not only in the US and Japan were EHEC outbreaks, but also in Europe, e.g. Sweden 2002^[10] and Norway 2006^[11] such outbreaks appeared.

In Germany, there were two outbreaks. The first appeared in 1995 in Bavaria,^[12] the second 2011 in northern Germany.^[13-18] To recognize such outbreaks, a reporting requirement for EHEC disease was introduced 1998 in Germany.^[19] In the first years (2001 to 2003) of the reporting system, around 1000 peoples in Germany yearly got infected by EHEC.^[19] In the last six years, more than 2000 people got infected by EHEC per year (figure 1.1).^[20]

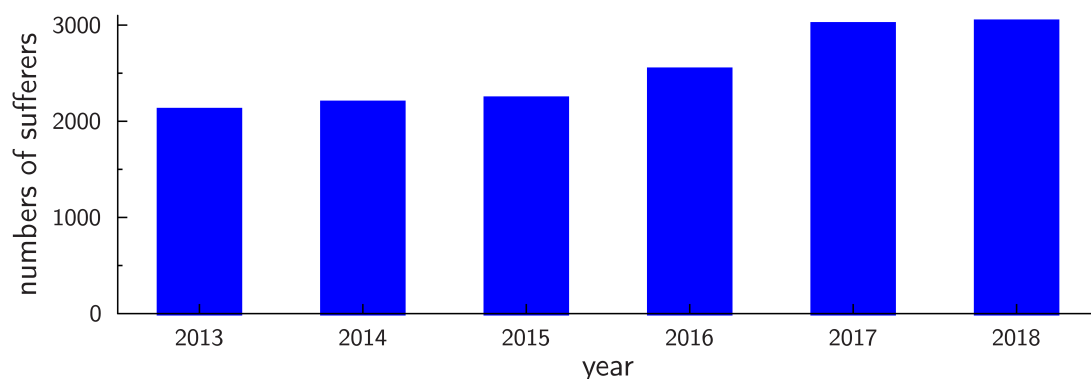


Figure 1.1.: The reported cases of enterohemorrhagic *Escherichia coli* (EHEC) disease in Germany from 2013 to 2018. The data was taken from the Robert Koch-Institut with SurvStat@RKI 2.0 at 30.07.2019.^[20]

The effects of the disease caused by EHEC ranges from diarrhea,^[21,22] bloody diarrhea,^[23–25] hemorrhagic colitis,^[26–28] haemolytic uraemic syndrome (HUS)^[17,29–33] to the damages of the central nervous system.^[30,34] Some patients even died from EHEC infection due to multiple organ failure.^[19]

The different symptoms could be explained by different bacterial strains.^[35,36] The different bacterial strains produce the same toxin, but different sub types due to a different binding affinity to the cells. The toxin of EHEC is the protein shiga toxin (STx) which is also the toxin from *Shigella dysenteriae*.^[37]

The uptake of the EHEC happens *via* food, e.g. raw meat^[4,38] or unwashed vegetables.^[39] Within the intestine, the bacteria produces STx.^[40] The toxin activates the innate immunity. This results in a change of the cell morphology and in a change of the intercellular tight junctions in the intestinal epithelial. The STx can then cross the intestinal epithelial barrier into the blood stream.^[40] Through the blood stream, the STx is distributed into the whole body. The cell membrane of different tissues in the human body has different amounts of globotriaosyl ceramide (Gb₃) which is the receptor lipid of STx in the outer membrane leaflet.^[41–43] The microvascular endothelial cells of the glomerular and brain have a high amount of the receptor lipid Gb₃ in the outer membrane leaflet.^[44–47] This correlates with the disease caused by EHEC, HUS damage of the kidney (glomerular cells) and damage of the central nervous system. A topographical analysis of the distribution from Gb₃ in a whole human body has not been done yet, but in a study with a whole weaned piglet. The topographical analysis showed the highest amount of Gb₃ in the intestine and the lung.^[48] The amounts of Gb₃ in the tissues were ranked, the kidney cells are only at rank 8 and the cells of the brain are at rank 21 of altogether 25 ranks.^[48]

1.2. Shiga toxin

The toxin from EHEC is the STx which kills cells. To understand the mechanism of the toxicity from EHEC, a deeper look at the structure and uptake of STx is necessary. The STx is a AB₅ toxin with one toxic A-subunit of STx (STxA) and five binding subunits the B-subunits of STx (STxB) (figure 1.2 A).^[49–52] The five STxB form a pentameric ring (figure 1.2 B). The STxA binds with a α -helix into the middle of the ring (figure 1.2 A).^[51] The receptor lipid Gb₃ has 15 binding sides in the pentameric structure of STxB (figure 1.2 C).^[50]

Cells which were incubated with STx and had Gb₃ at the outer leaflet died, because the STxA binds to the ribosomes and blocks the protein biosynthesis.^[53] The STx cannot diffuse through the membrane. The mechanism of the up take of STx into the

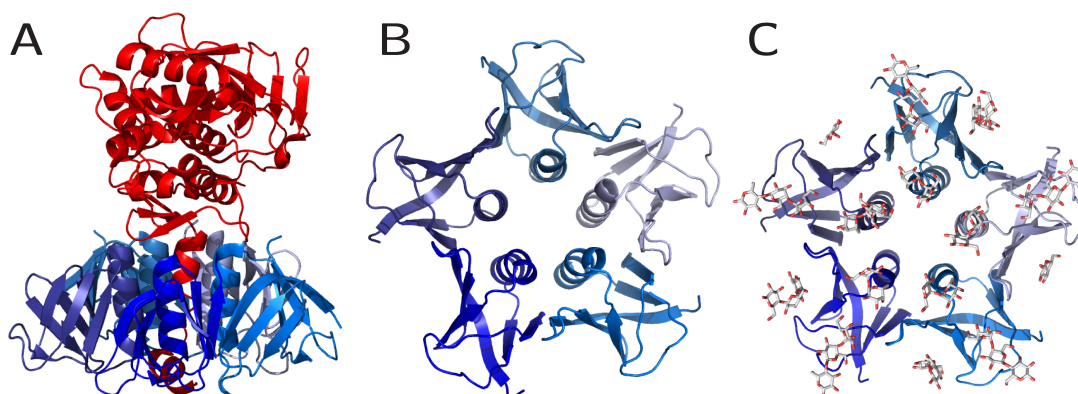


Figure 1.2.: The full protein shiga toxin (STx) is shown in A. The dark blue subunit is an A-subunit of shiga toxin (STxA) and the pentamer structure underneath are five B-subunit of shiga toxin (STxB) (PDB ID: 4M1U).^[51] The pentamer structure of STxB is separately shown from the membrane site in B (PDB ID: 1C48). The 15 globotriaosyl ceramide (Gb₃) bindings sites of the pentamer of STxB are visualized in C (PDB ID: 1BOS).^[50]

cell is shown in (figure 1.3). The initiate step of the uptake of STx into the cell is the binding of STxB to its receptor lipid Gb₃ at the outer leaflet of the plasma membrane which is a heterogeneous two-dimensional fluid of proteins and lipids and is explained in the next chapter 1.3. The STx clusters on the membrane,^[54] builds up membrane invaginations^[55] and endocytotic pits.^[56,57] These endocytotic pits are absorbed by the cells through clathrin-dependent^[58,59] or clathrin-independent endocytosis.^[60,61] In the early endosomes, the STx are directed towards the late endosomal traffic route. The STx path to the endoplasmic reticulum goes from the late endosomes through the *trans*-Golgi network into the endoplasmic reticulum. In the endoplasmic reticulum, the membrane-associated endoprotease furin cuts the STx between the amino acids Arg251-Met252 from the STxA and activates its toxicity.^[62] In this step, the translocation of STxA from the inside of the endoplasmic reticulum into the cytosol takes place as well.^[63] In the cytosol, the activated STxA inhibits the protein biosynthesis at the rRNA-N-glykosidase which kills the cells.^[53,64]

An interesting fact is that cancer cells also have a high amount of Gb₃ at the outer membrane leaflet^[65-67] and the usage of STx for the cancer therapy is under research.^[68-70] The nice STx uptake mechanism of a cell is perfect for transporting therapeutic proteins into the endoplasmic reticulum or directly into the cytosol.^[69,71] There are different approaches to design anti-cancer drugs with STxB. A linker residue combined with a drug is chemically synthesized to the STxB pentamer.^[72-74] The design of fusion proteins was also evaluated. For that purpose, the toxic part of STxA was substituted by a therapeutic protein.^[75] Also, multi-lamellar vesicles (MLVs) coated with STxB at the outer leaflet were used, with anti cancer drugs on the

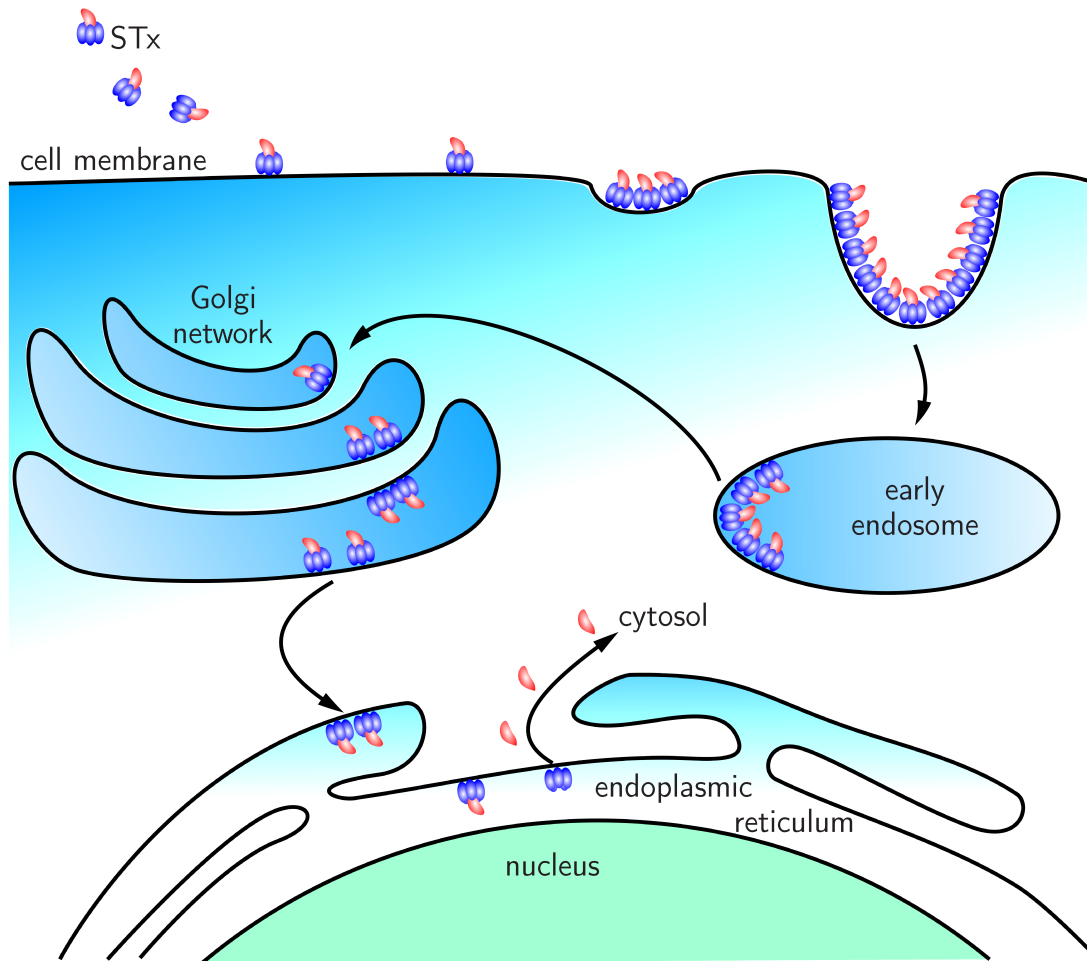


Figure 1.3.: Shiga toxin (STx) is taken up from the cell *via* binding to the cell membrane and clusters. The clusters build endocytotic pits and are taken up into the early endosomes. The STx is directed by the early endosomes to the retrograde traffic route over the Golgi network into the endoplasmic reticulum. There, the STxA is cut from the STx and is translocated into the cytosol, where it inhibits the ribosomes.^[62,64]

inside.^[76] In all those cases, the drugs for the cancer cells are taken up from all cells with Gb₃ on the outer leaflet. In the cancer therapy, the STxB can be mutated to have a better selection on the cell type and Gb₃ concentrations.

The better understanding of the binding from STx to the cell membrane would help to design better drugs against EHEC and to design a selective drug against cancer. One important aspect is to know where the Gb₃s are concentrated before STx binds at the cell membrane.

1.3. Cell membranes and their properties

The cell membrane is not only a homogeneous two dimensional fluid, which Singer and Nicolson suggested.^[77] The plasma membrane of an eucaryotic cell has many different components which can be divided into two major groups, lipids and membrane proteins. The lipid builds up the membrane matrix in which the membrane proteins are incorporated. The membrane has many different lipids which are divided into the subgroups glycerolipids, sterols and sphingolipids.^[78,79] The glycerolipids as well as the sphingolipids have different head groups. Very often, a phosphate is present in the lipid head group called phospholipids, which can be either a glycerolipid or a sphingolipid. The main lipid content are the phosphoglycerolipids, which are divided into the different head groups, phosphatidylcholine (PC), phosphatidylethanolamine (PE), phosphatidylinositolphosphate (PIP) and phosphatidylserine (PS). The glycerolipids as well as the sphingolipids have different fatty acids.

The membrane has a huge amount of different lipids aggregated into a two dimensional fluid. The different lipids and different proteins cluster in different ways and amounts which results in a heterogeneous membrane.^[80-83] These clusters or domains are called lipid rafts (figure 1.4).^[80] Lipid rafts are defined as "small (10–200 nm), heterogeneous, highly dynamic, sterol- and sphingolipid-enriched domains that compartmentalize cellular processes. Small rafts can sometimes be stabilized to form larger platforms through protein-protein and protein-lipid interactions."^[84] Three different lipid rafts are illustrated in figure 1.4. First, different proteins are activated in the lipid raft which are inactive in the non-raft membrane (figure 1.4).^[85,86] It was reported that the actin network binds to a lipid raft.^[87] The cell used the glycosphingolipids for signaling processes and communications which are enriched in such lipid rafts.^[88] The last illustrated lipid raft contains the receptor lipid for STx it is Gb₃ and the STx binds to it.^[64] It is not clear if the lipid rafts exist first, before the toxin bind, or if the lipid raft is created by the binding of the toxin. A problem is that such lipid rafts are not visualized with the newest technical equipment in eukaryotes.^[89] Only indirect information from detergent resistant membrane (DRM),^[90] fluorescence resonance energy transfer (FRET)^[91,92] and fluorescence correlation spectroscopy (FCS)^[93,94] measurements hints that such rafts exist. In bacterial small domains of ~40 nm in diameter were found.^[95]

The heterogeneity of the lipid raft model was analyzed in model membrane systems with the three major membrane lipids of eucaryotic cells, a low melting phospholipid (POPC or DOPC), a high melting lipid (DPPC or sphingomyelin (SM)) and sterol (cholesterol (Chol)).^[97,98] These model membranes undergo phase separation in a wide

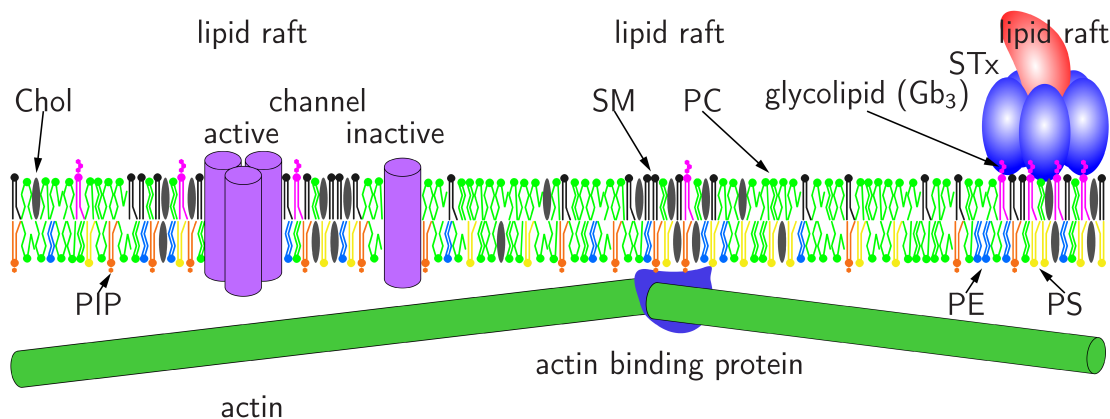


Figure 1.4.: A schematic drawing of the cell membrane with three different lipid rafts. From left to right, the first lipid raft activates a channel protein,^[85] with the second one the actin is bound^[87] and in the third one glycolipids are enriched and shiga toxin (STx) binds to it.^[88] The cell membrane has different lipid species such as cholesterol (Chol), sphingomyelin (SM), phosphatidylcholine (PC), glycolipid as globotriaosyl ceramide (Gb₃), phosphatidylinositolphosphate (PIP), phosphatidylethanolamine (PE) and phosphatidylserine (PS).^[96]

region of the lipid compositions.^[99] The lipid raft hypothesis is mimicked by such phase-separated membranes. The two phases of the raft mimic model membranes are the liquid ordered (l_o) phase which is enriched in high melting lipids and sterols and mimics the raft domains and the liquid disordered (l_d) phase which is enriched in low melting lipids and mimics the membrane matrix. The non-physiological lipid DOPC is preferential used instead of POPC, because the domains are larger and better visible with the fluorescent microscope.^[97] The raft mimic model membranes which represent the cell membranes and the phase distribution of the STx receptor lipid will be analyzed. These data are an indication of the position from Gb₃ in the plasma membrane relative to the lipid raft theory.

The measurement of the raft like lipid composition can be accomplished on different membrane systems which can be the giant unilamellar vesicles (GUVs),^[100] adhered GUVs,^[101] pore-spanning membranes (PSMs)^[102] and solid supported membranes (SSMs)^[103] (figure 1.5). GUVs and SSMs mimic the cell membrane with the same conditions for each membrane region (figure 1.5 A, D). The two different leaflets can have different surroundings. In GUVs the buffer inside can be different from the buffer outside of a GUV.^[104,105] The different leaflets of the SSMs are distinguishable: One is in contact with the surface of the support and the other leaflet is in contact with the solution. SSMs are very easy to handle and the membrane is, in contrast to the GUVs, two dimensional which is useful for microscopy studies (figure 1.5 D). With the supported membrane, the SSMs mimic the membrane cell adhesion to a

surfaces. The increase of water between support and the membrane of SSM makes sure that the surface interaction has no influence of the properties from integral membrane proteins.^[106] Therefore polymer-supported membranes were developed which increase the water film between the membrane and the substrates from few nm to many nm.^[107] This increase of the water layer also increases the activity of proteins in the SSMs and brings it nearer to the membrane system of GUVs which mimic the membrane part of a cell which has no contact. To combine the adhesion membrane model (SSM) and the membrane model without any adhesion (GUV), the whole cellular membrane is described, because the cellular membrane has parts with adhesion and parts without. The cell membrane interacts not only with the surface outside of the cell but it has also adhesion properties to the inside of the cell.^[108] The actin network stabilizes the plasma membrane and interacts strongly over actin binding proteins with the membrane.^[109] This can be mimicked with membrane systems which have different adhesion properties such as the adhered GUVs and the PSMs (figure 1.5 B and C). Both membrane systems have an adhered area as in SSMs and in both membrane systems there are lipid areas where the membrane is as free-standing as in GUVs.^[102,110] These membrane systems mimic the cell membranes with different adhesion properties to a surface or to the actin network.^[102]

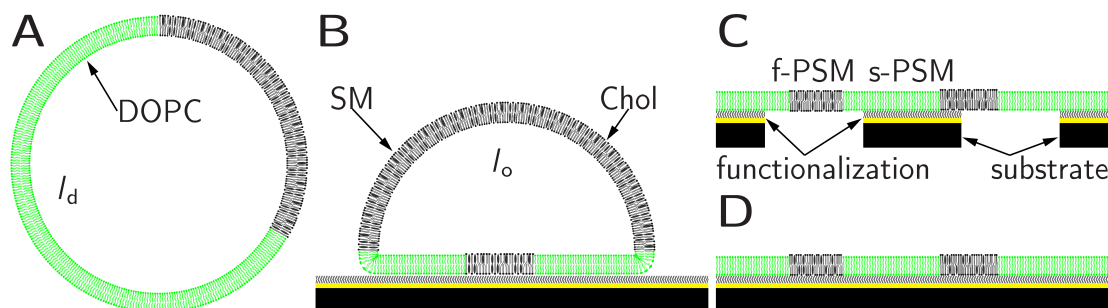


Figure 1.5.: Different model membrane systems are giant unilamellar vesicles (GUVs) (A), adhered GUVs (B), pore-spanning membranes (PSMs) (C) and solid supported membranes (SSMs). The shown systems are schematically drawn with phase-separated membranes, which contain DOPC/sphingomyelin (SM)/cholesterol (Chol). The liquid disordered (l_d) phase is enriched in DOPC and the liquid ordered (l_o) phase is enriched in SM and Chol. The substrates for the adhered GUVs, PSMs and SSMs are functionalized with two different layers. The functionalization can differ for each system.

The actin network has an influence on the phase separation in membranes. Liu *et al.* showed that the l_o phase is co-localized with the actin network.^[87] This can be a rearrangement of lipids or that the phase diagram of such a lipid mixture changes with different adhesion regions which are adhesion to the action network or not. A phase diagram of PSMs was investigated which mimics such two different adhesion

1. Introduction

regions for one membrane. This model system should clarify if cell adhesion also has an influence on the raft building or if only the different lipid and protein components do that. These influences have then also an effect on the distribution of Gb₃ in the plasma membrane. The distribution of the Gb₃ was investigated with a raft mimic membrane system in which fluorescently labeled Gb₃s were incorporated. This analysis was done in GUVs. The knowledge of the distribution of the Gb₃ in plasma membrane or plasma mimic membrane can help to understand the binding properties of STxB to Gb₃ so that different drugs against EHEC can be designed which changes the Gb₃ distribution in the plasma membrane and prevent the uptake of STx into the cell.

2. Scope of the thesis

The bacterium enterohemorrhagic *Escherichia coli* (EHEC) is one of the main causes of food-borne illness around the world. The disease caused by EHEC ranges from different diarrheas over hemorrhagic colitis and haemolytic uraemic syndrome up to damage of the central nervous system, in some cases with lethal outcome. All these different diseases are only triggered by the toxic protein shiga toxin (STx) which inhibits the protein biosynthesis of eukaryotic cells. In a first step, while approaching the cells, the B-subunit of STx (STxB) binds to the receptor lipid globotriaosyl ceramide (Gb₃) which is present in the outer membrane of human cells. The cellular membrane is highly heterogeneous and has regions of various ordering. This might lead to enrichment or depletion of Gb₃ in certain areas.

One important finding is that the Gb₃, the receptor for STx, is enriched in membranes of cancer cell. A better understanding of the binding from STx to the cell membrane would help to improve drug development against EHEC and open pathways for drugs to selectively target cancer cells. One important point is the knowledge where Gb₃s are concentrated before STx binds to the cell membrane. Quantification of local Gb₃ concentration in areas of different lipid order of biomimetic membranes is one scope within this thesis. For the quantification giant unilamellar vesicles (GUVs) and pore-spanning membranes (PSMs) are used which allow preparation of membranes with high definition to identify the impact of membrane ordering to Gb₃ enrichment.

The regions of various ordering in the cellular membrane can be affected by heterogeneous connections to either the cytoskeleton in the inside of the cell or to different surfaces at the outside of the cell. A second scope of this thesis is to identify the effects related to membrane-surface interactions (adhesion) to the organization of membranes with regions of higher and lower ordering. This might also influence the preferential distribution of Gb₃ in lipid membranes.

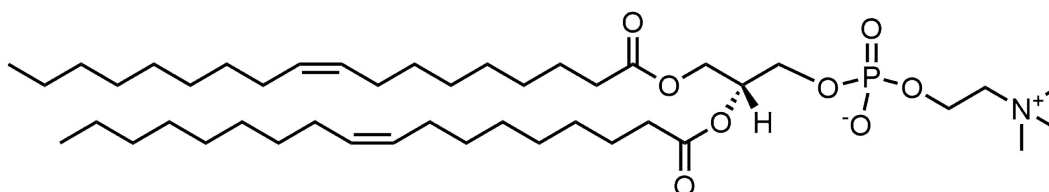
3. Materials and methods

3.1. Used materials

3.1.1. Matrix lipids

In this work, different lipids with different functions were used. The lipid composition of the analyzed membranes with an amount of at least of 94 % are summarized as matrix lipids and represent the three main compositions of mammalian lipids, glycerolipids, sphingolipids and sterols.^[78]

1,2-dioleoyl-*sn*-glycero-3-phosphatidylcholine (DOPC)

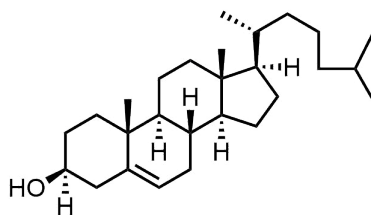


Scheme 3.1.: The structure of 1,2-dioleoyl-*sn*-glycero-3-phosphatidylcholine (DOPC).

1,2-dioleoyl-*sn*-glycero-3-phosphatidylcholine (DOPC) is a non-natural glycerophospholipid with two oleic acids in the hydrophobic part (Scheme 3.1). This phospholipid is used in many model systems and has a low transition temperature (T_M). The reported T_M s are $-14\text{ }^\circ\text{C}$,^[111] $-16.5\text{ }^\circ\text{C}$,^[112] $-17.3\text{ }^\circ\text{C}$,^[113] $-18.3 \pm 3.6\text{ }^\circ\text{C}$,^[114] $-18\text{ }^\circ\text{C}$,^[115] $-19.1\text{ }^\circ\text{C}$,^[116] $-21\text{ }^\circ\text{C}$ ^[117] and $-22\text{ }^\circ\text{C}$.^[118] The molecular weight of DOPC is $786.129\text{ g mol}^{-1}$ and the chemical formula is $\text{C}_{44}\text{H}_{84}\text{NO}_8\text{P}$.

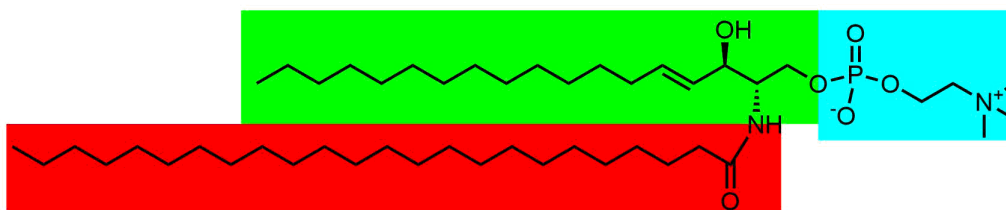
Cholesterol (Chol)

Cholesterol (Chol) is a sterol (scheme 3.2). Chol has a molecular weight of 386.35 g mol^{-1} and its chemical formula is $\text{C}_{27}\text{H}_{46}\text{O}$. It is present in mammalian membranes and reduces the fluidity in the liquid-crystalline phase.^[119] Chol increases the fluidity for gel phase membranes. Sphingomyelin (SM) and Chol are the main lipid parts in the lipid rafts.^[84]



Scheme 3.2.: The structure of cholesterol (Chol).

Sphingomyelin (SM)



Scheme 3.3.: The structure of lignoceroyl sphingomyelin ($SM_{C_{24:0}}$) is shown as an example of sphingomyelin (SM) structure. The sphingosine structure is labeled in green. The hydrophilic cholin-phosphate-ester group (blue) is connected with a phosphate-esters to the sphingosine. The lignoceric acid (red) is connected *via* an amide bond to the 2 amine group of the sphingosine.

Sphingomyelin (SM) has a sphingosine basic structure (figure 3.3 green). A cholin group (figure 3.3 blue) is connected at the 1 hydroxyl-group of the spingosine by a phosphate-ester. The fatty acid (figure 3.3, red) which is connected through a amide bond to the 2 amine group of the sphingosine differs in each SM species. The shown $SM_{C_{24:0}}$ has a lignoceric acid as a fatty acid. Porcine brain SM (SM_{porc}) is a natural SMs extraction and was used in this work. SM_{porc} is a SM mixture with six known different SM species (table 3.1).

Table 3.1.: The natural sphingomyelin (SM) extraction, porcine brain sphingomyelin (SM_{porc}), has different amounts of different SMs, which are listed here. The different extracted SMs are palmitoyl sphingomyelin ($SM_{C_{16:0}}$), stearoyl sphingomyelin ($SM_{C_{18:0}}$), arachidoyl sphingomyelin ($SM_{C_{20:0}}$), behenoyl sphingomyelin ($SM_{C_{22:0}}$), lignoceroyl sphingomyelin ($SM_{C_{24:0}}$) and nervonoyl sphingomyelin ($SM_{C_{24:1}}$) and an unknown fraction.^[120,121]

SMs	$SM_{C_{16:0}}$	$SM_{C_{18:0}}$	$SM_{C_{20:0}}$	$SM_{C_{22:0}}$	$SM_{C_{24:0}}$	$SM_{C_{24:1}}$	Unknown
%	2	49	5	8	6	20	10

The synthetic SMs which were used in this work are palmitoyl SM ($SM_{C_{16:0}}$), stearoyl SM ($SM_{C_{18:0}}$), arachidoyl SM ($SM_{C_{20:0}}$), behenoyl SM ($SM_{C_{22:0}}$) and lignoceroyl SM ($SM_{C_{24:0}}$). At room temperature, all SMs are in the gel-phase. The

T_{MS} from the gel-phase to the liquid-crystalline phase for different SMs are listed in table 3.2. For some SMs, there are reported gel to gel-phase T_{MS} which are also listed. SMs occur in mammalian cells and are contributed to the lipid raft theory. The lipid rafts are enriched in SMs and Chol. In model membranes, SMs are enriched in the liquid ordered (l_o) phase when the membrane undergoes phase separation into the liquid disordered (l_d) and l_o phase.

Table 3.2.: The different sphingomyelins (SMs) have different transition temperatures (T_{MS}). Some literature reported pre- T_{MS} which are also listed and separated with a comma. The various T_{MS} from varying literature are separated with a semicolon. The different SMs are porcine brain sphingomyelin (SM_{porc}), palmitoyl sphingomyelin (SM C_{16:0}), stearoyl sphingomyelin (SM C_{18:0}), arachidoyl sphingomyelin (SM C_{20:0}), behenoyl sphingomyelin (SM C_{22:0}), lignoceroyl sphingomyelin (SM C_{24:0}) and nervonoyl sphingomyelin (SM C_{24:1}).

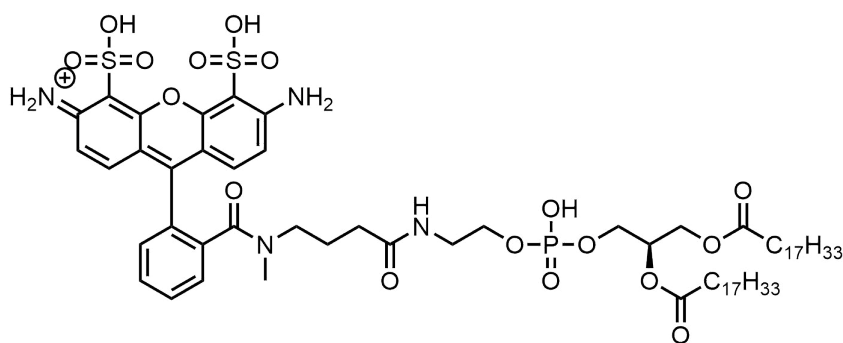
SMs	List of reported transition temperatures[°C]
SM _{porc}	35–40; ^[120] 35.7 ± 5.8 ^[122]
SM C _{16:0}	40.2 ± 2.6; ^[122] 39.6; ^[123] 27.5, 40.4; ^[124–126] 41; ^[127] 30, 41; ^[128] 40.5; ^[129] 41.3; ^[130] 40.5; ^[131] 37.5; ^[132] 30.9, 41.7; ^[133] 41.5 ^[134,135]
SM C _{18:0}	44.9 ± 0.4; ^[122] 43.7; ^[123] 45; ^[127] 52.8; ^[130] 44.7; ^[131] 44.5; ^[132] 33.9, 44.7; ^[133] 44; ^[134] 33.4, 44.1 ^[125,126]
SM C _{20:0}	46.5; ^[122,127] 32.4, 44.6 ^[125,126]
SM C _{22:0}	31.7, 45.8; ^[124–126] 18.4, 46.9; ^[127] 44.5 ^[122,132]
SM C _{24:0}	40.0, 46.7; ^[124–126] 40, 47.5; ^[122,127] 42, 47; ^[128] 42.6, 48.6; ^[130] 37.6, 45.7; ^[136] 34.9, 44.2; ^[137] 47.1; ^[131] 39.5, 46.2; ^[138] 35.5; ^[132] 46.1; ^[133]
SM C _{24:1}	18.0, 22.3, 27.4; ^[123] 14, 16, 23; ^[128] 26.2; ^[131] 27.5; ^[122,132] 24.1 ^[133]

3.1.2. Membrane fluorescent probes

To visualize the lipid bilayer under a microscope, different fluorescent probes were used. The used l_d phase marker are all coupled to DOPE or 1,2-dipalmitoyl-*sn*-glycero-3-phosphatidylethanolamine (DPPE). Different light amplifications by stimulated emission of radiation (lasers) were used to excite the fluorophores.

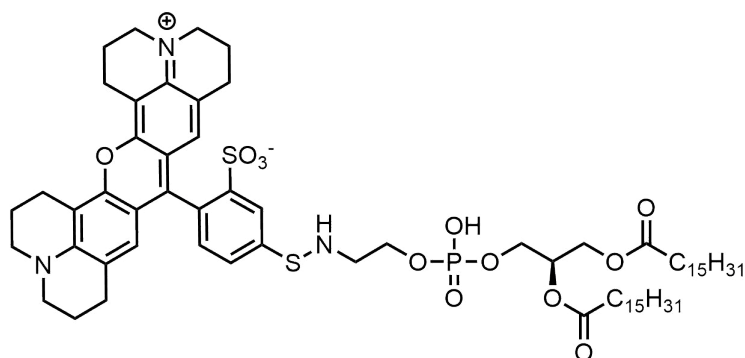
ATTO488-DOPE

ATTO488-1,2-dioleoyl-*sn*-glycero-3-phosphoethanolamin (ATTO488-DOPE) is a lipid coupled membrane fluorophore (scheme 3.4). The marked lipid is DOPE and the fluorophore is ATTO488. The excitation maximum is at the wavelength 500 nm and the emission maximum at the wavelength 520 nm. The excitation with the laser line 488 nm is possible. This fluorophore is an l_d phase marker. In this work, the fluorophore was used to visualized membranes and phase-separated membranes.



Scheme 3.4.: The structure of ATTO488-1,2-dioleoyl-*sn*-glycero-3-phosphoethanolamin (ATTO488-DOPE). The ATTO488 fluorophore is connected to a DOPE lipid.

TexasRed-DHPE

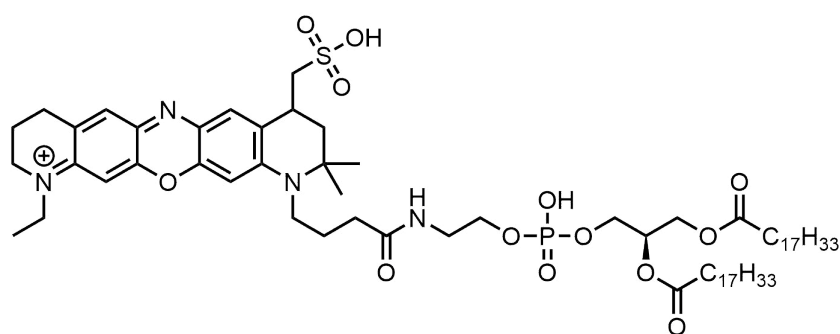


Scheme 3.5.: The structure of sulforhodamine-1,2-dihexanoyl-*sn*-glycero-3-phosphoethanolamine (TexasRed-DHPE). The sulforhodamine fluorophore is connected to a DPPE lipid.

A l_d phase marker fluorophore is the sulforhodamine-1,2-dihexanoyl-*sn*-glycero-3-phosphoethanolamine (TexasRed-DHPE).^[139,140] The sulforhodamine is connected to a DPPE lipid (scheme 3.5). This fluorophore was used to label membranes and phase-separated membranes. The diffusion constant of this fluorophore was determined with fluorescence correlation spectroscopy (FCS) in freestanding pore-spanning membranes (f-PSMs) composed of the DOPC membrane. The excitation maximum and emission maximum are 595 nm and 615 nm. The fluorophore was excited with the laser wavelength 561 nm.

ATTO655-DOPE

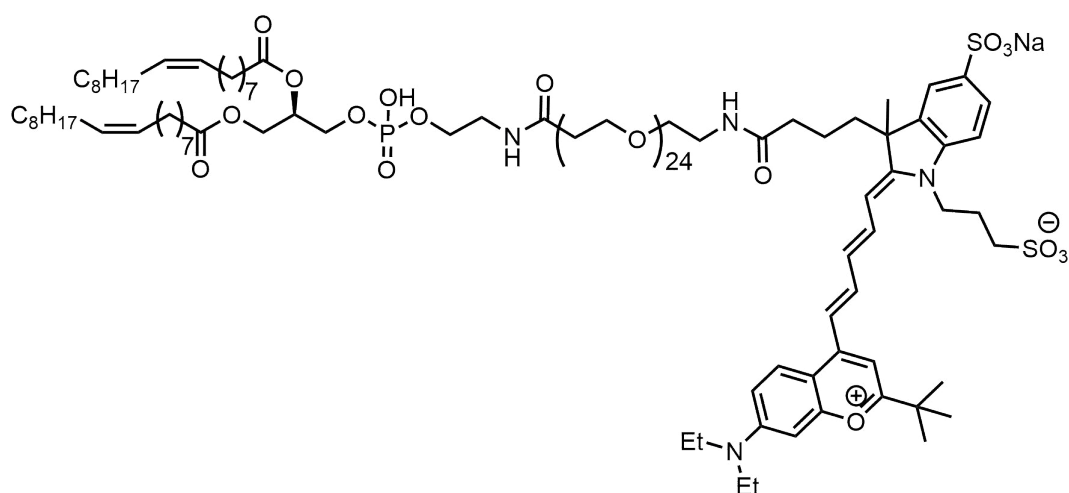
ATTO655-1,2-dioleoyl-*sn*-glycero-3-phosphoethanolamin (ATTO655-DOPE) is a lipid-coupled membrane fluorophore (scheme 3.6). The lipid is DOPE and the fluorophore is ATTO4655. The excitation maximum is at the wavelength 663 nm and



Scheme 3.6.: The structure of ATTO655-1,2-dioleoyl-*sn*-glycero-3-phosphoethanolamin (ATTO655-DOPE). The ATTO655 fluorophore is connected to a DOPE lipid.

the emission maximum is at the wavelength 680 nm. The excitation with the laser line 633 nm is suitable and this fluorophore is an l_d phase marker. In this work the fluorophore was used to visualize membranes and to measure the diffusion constant with FCS in DOPC f-PSMs.

Dy731-DOPE



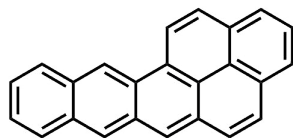
Scheme 3.7.: The structure of Dy731-PEG₂₅-1,2-dioleoyl-*sn*-glycero-3-phosphoethanolamin (Dy731-DOPE). The Dy731 fluorophore is connected *via* 25 polyethylene glycol (PEG) units to a DOPE lipid.

Dy731-PEG₂₅-1,2-dioleoyl-*sn*-glycero-3-phosphoethanolamin (Dy731-DOPE) is a lipid coupled fluorophore (scheme 3.7). The fluorophore (Dy731) was connected to a DOPE with 25 polyethylene glycol (PEG) units in between. This was done in the group of Prof. Dr. Daniel B. Werz. The excitation wavelength is 732 nm and the fluorophore emits by 763 nm. The phase preference of this fluorophore is the l_d phase.^[141] This fluorophore was used in the phase distribution measurements of

3. Materials and methods

globotriaosyl ceramide (Gb₃). It is possible to excite Dy731-DOPE with the laser wavelength 633 nm.

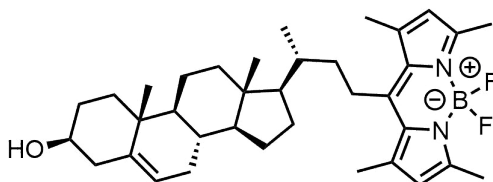
Naphthopyrene



Scheme 3.8.: The structure of naphtho[2,3-a]pyrene (naphthopyrene).

The fluorophore naphtho[2,3-a]pyrene (naphthopyrene) has an excitation maximum at 459 nm and an emission maximum at 495 nm. The structure of naphthopyrene is planar and has 24 π electrons (scheme 3.8). The phase preference of naphthopyrene is the l_o phase.^[139,140] In this work naphthopyrene was used to measure the diffusion constant with FCS in the l_o phase in the f-PSM. The excitation laser wavelength amounted to 458 nm.

BODIPY-Chol

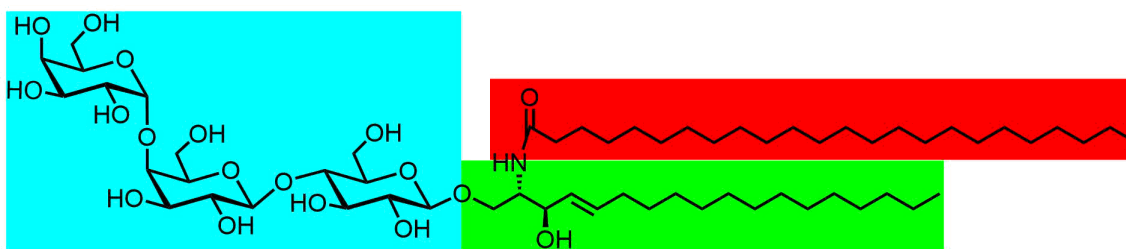


Scheme 3.9.: The structure of 23-(dipyrrrometheneboron difluoride)-24-norcholesterol (BODIPY-Chol).

23-(dipyrrrometheneboron difluoride)-24-norcholesterol (BODIPY-Chol) is a Chol derivative (scheme 3.9). The fluorophore BODIPY is connected to the 23'-C-atom of Chol. The BODIPY-Chol has the phase preference of Chol and is an l_o phase marker.^[140,142] The emission maximum is at the wavelength 506 nm and the maximum of the excitation wavelength is at 499 nm. BODIPY-Chol was stimulated with the laser line 488 nm. The BODIPY-Chol was used to visualize the l_o phase in PSMs and the diffusion constant was measured in the l_o phase with FCS in f-PSMs.

3.1.3. Globotriaosyl ceramide

Globotriaosyl ceramide (Gb₃) is the receptor lipid of shiga toxin (STx). The receptor structure motive is the trisaccharide α -D-galactose-(1 \rightarrow 4)- β -D-galactose-(1 \rightarrow 4)-

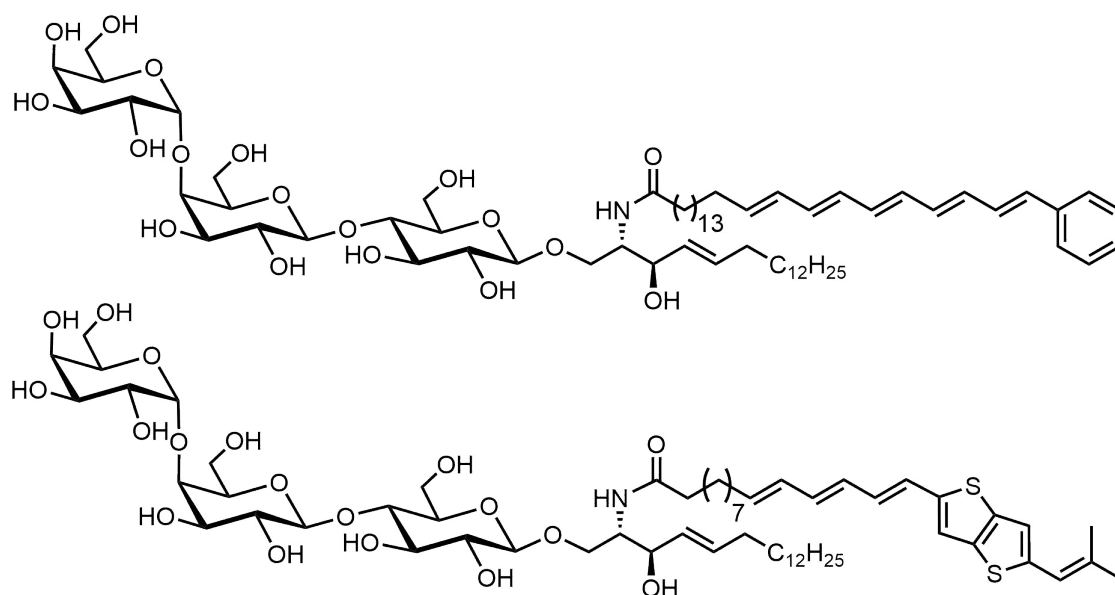


Scheme 3.10.: The structure of globotriaosyl ceramide (Gb_3) has a sphingosine motive (green). The head group of Gb_3 consists of a trisaccharide which is α -D-galactose-(1 \rightarrow 4)- β -D-galactose-(1 \rightarrow 4)- β -D-glucose (blue). The hydroxyl/aldehyde group from glucose 1 binds to the sphingosine 1 hydroxyl group *via* an acetal bond. The Gb_3 can vary in the fatty acid (red) which is connected *via* an amide bond to the 2 amine group of the sphingosine. The shown Gb_3 has a lignoceroyl fatty acid.

β -D-glucose (figure 3.10 blue). This is connected to a sphingosine skeleton with an acetal bond (figure 3.10 green). The fatty acid which is connected *via* an amide bond to the 2 amine of the sphingosine can vary in the Gb_3 like the SMs (figure 3.10 red). A porcine erythrocytes Gb_3 ($Gb_{3\text{porc}}$) was used. The fatty acid mixture in the $Gb_{3\text{porc}}$ is composed of 21 % palmitic, 4 % stearic, 2 % oleic, 14 % behenic, 1 % tricosylic, 19 % lignoceric, 11 % nervonic, 4 % α -hydroxylated behenic, 5 % α -hydroxylated lignoceric and 17 % α -hydroxylated nervonic acids.

Fatty acid labeled Gb_3 s

Two different Gb_3 s species with a labeled fatty acid were used in this work. The Gb_3 phenyl-modified fatty acid ($Gb_3\text{PH}$) and Gb_3 thienothienyl-modified fatty acid ($Gb_3\text{TT}$) were synthesized by the group of Prof. Dr. Daniel B. Werz.^[141] Both structures have an aromatic ring system, phenyl and thienothienyl respectively. The π electron systems are expanded with conjugated double bonds. Five conjugated double-bonds in a trans configuration were synthesized at the phenyl ring to increase the wavelength of the absorption and emission. The carbon-chain between the phenyl group and the acid group has 25 carbon atoms. The thienothienyl π electron system was expanded with three conjugated double-bonds in direction to the carbon acid and to the other direction with one double bond. All double bonds have the trans-configuration. There are 14 carbon atoms between the carbon acid and the thienothienyl ring system. The excitation wavelengths for the $Gb_3\text{PH}$ and $Gb_3\text{TT}$ are from 330 to 366 nm and 369 to 391 nm respectively. The emission maxima are at 434 nm and 440 nm respectively.



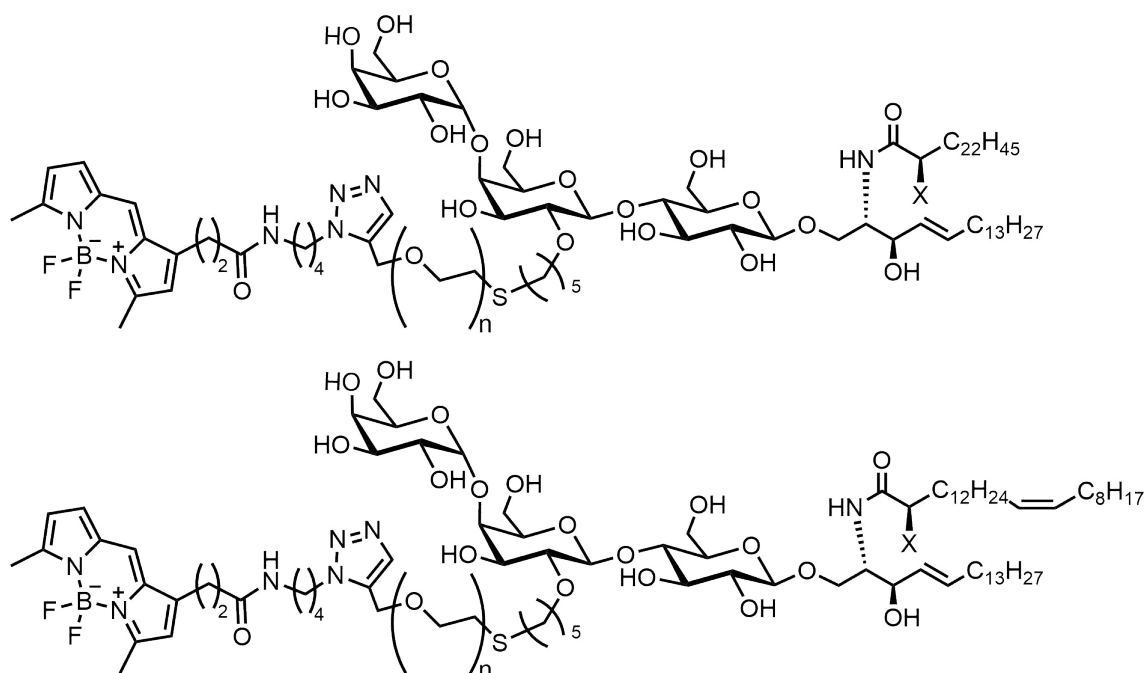
Scheme 3.11.: Structures of the two different fatty acid labeled globotriaosyl ceramides (Gb_3s). The structure of globotriaosyl ceramid phenyl-modified fatty acid (Gb_3PH) is shown at the top, the structure of globotriaosyl ceramid thienothieryl-modified fatty acid (Gb_3TT) below. Both fatty acids have a conjugated π electron system in the ring structure and conjugated double bonds with them.

head group labeled Gb_3s

The head group labeled Gb_3s were synthesized by the group of Prof. Dr. Daniel B. Werz (figure 3.12).^[143] The group synthesized eight different head group labeled Gb_3s . The fluorophore which is connected over a PEG linker to the 2'-hydroxylgroup of the β galactose was in all cases BODIPY. The linker length (n) differs from 3 to 13 units. The carbon chain of the fatty acid (m) in each case has 24 carbon atoms, but it differs in the saturation (Δ) meaning the saturated fatty acid ($\Delta=0$, scheme 3.12 top structure) and mono-unsaturated fatty acid ($\Delta=1$, scheme 3.12 bottom structure). The α position (X) from the fatty acid is hydroxylated (OH) or not (H). In total, all head group labeled Gb_3s are abbreviated to $Gb_3PEG_nC_{m:\Delta}X$.

3.1.4. B-subunit of shiga toxin

The shiga toxin (STx) has six subunits, the A-subunit of STx (STxA) and a pentameric structure of five B-subunits of STx (STxB). Only the STxB binds to the Gb_3 and therefore only the STxB was used in this study. The STxB samples A and C were purified by the working group of Prof. Dr. Winfried Römer (BIOSS an Institute of Biology II, Albert-Ludwigs University Freiburg) in 2013 and 2005.^[144,145] The STxB sample B was purified by the working group of Prof. Dr. Daniel Huster (Insti-



Scheme 3.12.: The structures of the head group labeled globotriaosyl ceramides (Gb_3S). The fluorophore BODIPY is connected *via* a PEG linker with n units (3,13) to the 2' hydroxyl group of the β galactose. The fatty acid ($C_{m:\Delta}$) varies in the saturated ($C_{24:0}$) top structure and mono-unsaturated ($C_{24:1}$) bottom structure. The α position of the fatty acid (X) is hydroxylated (OH) or not hydroxylated (H). In total, there are eight different combination which are shorten to $Gb_3PEG_nC_{m:\Delta}X$.

tute for Medical Physics and Biophysics, Leipzig University) in 2017.^[146] The STxB was stored at -80°C and was used in a phosphate-buffered saline (PBS) buffer. The molecular weight of STxB is 7.7 kDa and it has 69 amino acids. The protein sequence is:

TPDCVTGKVE YTKYNDDDTF TVKVGDKELF TNRWNLQSL LSAQITGMTV
TIKTNACHNG GGFSEVIFR.^[50]

3.2. Preparative methods

The used buffers are PBS or Tris. PBS consisted of KCl (2.7 mM), NaCl (136 mM), KH_2PO_4 (1.5 mM) and Na_2HPO_4 (8.1 mM) and had a pH of 7.4. Tris consisted of Tris (20 mM), NaCl (100 mM) and CaCl_2 (1 mM) and had a pH of 7.4

3.2.1. Preparation of vesicles

For this work, vesicles of different lipid compositions at different temperatures were prepared. Vesicles with DOPC and a fluorescent lipid were incubated at 30°C for

preparation of multi-lamellar vesicle (MLV) and incubated at room temperature for the preparation of large unilamellar vesicles (LUVs) and giant unilamellar vesicles (GUVs). The preparation temperature of phase-separated and l_o phase vesicles was 55 °C for all vesicle preparations. The phase-separated vesicles composed of DOPC/SM/Chol/Gb₃/ fluorescent lipid and the l_o phase vesicles composed of SM/Chol/ fluorescent lipid.

Multi-lamellar vesicles

Multi-lamellar vesicles (MLVs) were prepared from a lipid film. 0.2–0.4 mg of the lipid-mixture were dissolved in 200 μ L chloroform methanol solution (2:1) in a glass tube. The solvent was removed under a nitrogen stream with the preparation temperature of the lipid-mixture. The rest of the solvent was removed under reduced pressure at this temperature. The dry lipid film was stored at 4 °C for later use.

The lipid film was hydrated with 500 μ L of buffer and incubated for 20 min at the preparation temperature. After this time the film was vortexed for 30 s and incubated for 5 min at the preparation temperature. This procedure was repeated 3 times and the MLVs were used for the preparation of small unilamellar vesicles (SUVs) and LUVs.

Small unilamellar vesicles

Small unilamellar vesicles (SUVs) were prepared from MLVs with ultrasonic treatment. The MLVs solution was filled in an Eppendorf Tube and was placed in the ultra sonifier at 60% power for 30 min. The SUVs were used within one day after preparation.

Large unilamellar vesicles

Large unilamellar vesicles (LUVs) were prepared from MLVs by extrusion. The extruders were cleaned before use with 2 times ethanol, 2 times water and 2 times buffer. The diameter of the LUVs was given by the pore diameter of the membrane which was placed in the middle of the extrusion system. The MLV solution with the lipid mixture DOPC and fluorescent lipid was loaded into a hamilton syringe and pressed 31 times through the porous membrane. The LUV preparation, for the phase-separated and l_o phase lipid-mixtures, was carried out in a heating chamber at 55 °C. The extruder was heated up for 10 min, before the MLV solution was filled in. The solution was warmed up to 55 °C in the heating chamber for 10 min and pressed 11 times through the membrane. The warm up and extrusion process was repeated

3 times. After the extrusion, the LUV solution was filled in an Eppendorf Tube and used within one day after preparation.

Giant unilamellar vesicles

Giant unilamellar vesicles (GUVs) were prepared *via* electroformation. In this method, the lipid-mixture (0.1 mg in chlorophorm and methanol) was spread onto Indium Tin Oxide coated slides (ITO-slides) at the preparation temperature. The solvent was removed under reduced pressure at this temperature for 3 to 18 h. The ITO-slides were put together with a silicon ring in the middle so that a chamber of 1.5 mL was build and later filled up with a succrose solution (298 mOsmol). The GUVs were prepared by using a sinewave voltage (12 Hz, 1.6 V_{pp}), either 2.5 h or overnight, at the preparation temperature. The GUV solution was stored in dark Eppendorf Tubes up to three days at room temperature before being used.

3.2.2. Functionalization of porous substrates

For all experiments, porous substrates were obtained and used from Aquamarijn Micro Filtration BV (Zutphen, Netherlands) with pore diameters of 1.2, 2.0, 3.0 and 5.0 μm . The top layer of the substrates was made out of Si_3N_4 and had a thickness of 500 nm. The support structure was composed of Si with a thickness of 900 μm .

Mercaptoalcohol on gold

The porous substrates from Aquamarijn were cleaned with an argon-plasma. A thin titanium layer was sputter-coated on top of the substrates (40 mA, 60 s, 0.1 mbar). The titan is needed so that the gold stuck on the surface *via* an orthogonal evaporation process (30 to 40 nm, 3×10^{-6} to 6×10^{-6} mbar, 0.2 to 0.4 nm s^{-1}). The gold evaporated substrates were stored from 2 h up to several days in a 1 mM mercaptoalcohol *n*-propanol solution. The used mercaptoalcohols were 2-mercapto-1-ethanol (2ME), 6-mercapto-1-hexanol (6MH), 8-mercapto-1-octanol (8MO), 11-mercapto-1-undecanol (11MUD) and 16-mercapto-1-hexadecanol (16MHD).

Plasma cleaned silicon nitride

The porous substrates were cleaned by using argon-plasma and then hydrophilised by means of oxygen plasma. On the substrates, a gold layer was orthogonally evaporated (30 to 40 nm, 3×10^{-6} to 6×10^{-6} mbar, 0.2 to 0.4 nm s^{-1}). The orthogonal evaporated gold substrates were incubated in a 0.5 % 3-aminopropyltrimethoxysilane

methanol solution for 2 min to silanize the inner pore walls. After this the substrate was rinsed with ethanol and incubated with a solution of methoxy PEG succinimidyl carbonate (20 mg) in 1.5 mL ethanol for 5 min, the substrate were rinsed again with ethanol, dried under a nitrogen stream and stored in a petri dish. Before using the substrates for the preparation of PSMs, the gold layer was removed with an adhesive tape.^[147]

Silicon oxide

The porous substrates were cleaned with ethanol and dried under a nitrogen stream. The cleaned substrates were orthogonally evaporated with silicon monoxide (30 to 40 nm, 3×10^{-6} to 6×10^{-6} mbar, 0.2 to 0.4 nm s^{-1}). After evaporation, the substrates were incubate for 1 h in water at 55 °C before usage.^[148]

3.2.3. Preparation of pore-spanning membranes

The functionalized substrates were rinsed with ethanol, water and PBS. The wet substrates were placed into the measuring chamber. For temperature-controlled measurements, the chamber was made of copper and the substrate laid in a suitable gap. The chamber for the FCS measurement was made of steel and the substrate was fixed with a metal plate that was itself fixed on the side with a screw. The substrate in the interferometric scattering microscopy (iSCAT) measurements was prepared in a petri dish. The rest of the measurements were made in a petri dish and the substrate was fixed with adhesive tape. The chamber was filled up with PBS. It was heated up to 55 °C for the temperature-controlled measurements, in the other case the preparation took place at room temperature. 60–100 μL prepared GUV solution was sedimented through a 5 mL pipette tip filled with buffer over the substrate for 2 min. After waiting of 3–15 min, the PSMs were ready and the chamber was rinsed with buffer to remove the non-spreaded GUVs. For the iSCAT measurements, the prepared PSMs were incubated with gold nano particle (GNP), diameter of 20 or 40 nm for 30 min. The prepared substrates for the iSCAT measurements were transferred into the PBS filled iSCAT measurement chamber which had two gold stripes with a thickness of 200 nm. The substrates were also flipped for these measurements and set on top of the gold stripes. A 200 nm water layer was then between the membrane and the bottom of the iSCAT measurement chamber.^[147]

3.3. Biophysical methods

3.3.1. Fluorescence microscopy

A fluorescence microscope is a normal microscope only that the excitation light is not detected. A fluorophore absorb the excitation light and emitted light with higher wavelength which is explained by the Stokes shift. The emitted light is collected and filtered to be sure that no reflective light will be measured by the fluorescence microscope.

The wavelength of the excitation light can be adjusted by an optical filter and a white light source (mercury vapour lamp) or a light source which has a smaller wavelength spectrum, such as light-emitting diodes (LEDs) or lasers. The filtered excitation light was focused with an objective into the sample. The fluorophore absorb the light and emitted light with higher wavelength which was collected by the same objective and detected by a camera, photodiode or photomultiplier.

Confocal laser scanning microscope

A confocal laser scanning microscope (CLSM) works with lasers as excitation light source. The laser is scanned over the probe with two movable mirrors, pointwise excitation. The emitted light passes a pinhole to set the confocality of the system and is detected with a photomultiplier tube. In this work three different CLSMs were used. The CLSM from OLYMPUS was used for the fatty acid Gb₃ phase distribution study and the phase separation on PSMs study. Two different CLSMs from ZEISS (LSM 710, LSM 880) were used for the head group labeled Gb₃ phase distribution study. The LSM 880 was also used for the FCS measurements.

Fluorescence correlation spectroscopy

To measure fluorescence correlation spectroscopy (FCS), a CLSM can be used. Only one point spread function (PSF) is measured over the time. The PSF intensity ($I(x, y, z)$) is an ellipsoid with the short half axis ω_1 in x - and y -directions and ω_2 in the z -direction as long half axis

$$I(x, y, z) = I_0 \exp\left(-\frac{2(x^2 + y^2)}{\omega_1^2} - \frac{2z^2}{\omega_2^2}\right). \quad (3.1)$$

Theory

The intensity ($I(t)$) at time (t) of the PSF is compared to the intensity ($I(t + \tau)$) with the lag time (τ). The auto-correlation ($G(\tau)$) is calculated on the two different intensities by changing the lag time.^[149]

$$G(\tau) = \frac{\langle I(t + \tau) \cdot I(t) \rangle}{\langle I(t + \tau) \rangle \cdot \langle I(t) \rangle} \quad (3.2)$$

The mean intensities ($\langle I(t) \rangle$) of the two different intensity time traces are the same:

$$\langle I(t + \tau) \rangle = \langle I(t) \rangle. \quad (3.3)$$

With this, the auto-correlation function is reduced to:

$$G(\tau) = \frac{\langle I(t + \tau) \cdot I(t) \rangle}{\langle I(t) \rangle^2}. \quad (3.4)$$

The FCS curves are calculated by the intensity fluctuations ($\delta I(t)$) and not by the absolute intensity. The fluctuation is calculated by the difference of the mean intensity from the intensity time trace.

$$\delta I(t) = I(t) - \langle I(t) \rangle \quad (3.5)$$

The intensity fluctuation in the auto-correlation results in

$$G(\tau) = \frac{\langle (\langle I(t) \rangle + \delta I(t + \tau)) \cdot (\langle I(t) \rangle + \delta I(t)) \rangle}{\langle I(t) \rangle^2}, \quad (3.6)$$

and the factorizing of this resulted function gives

$$G(\tau) = \frac{\langle \langle I(t) \rangle \langle I(t) \rangle + \langle I(t) \rangle \cdot \langle \delta I(t + \tau) \rangle + \langle I(t) \rangle \cdot \langle \delta I(t) \rangle + \delta I(t + \tau) \cdot \delta I(t) \rangle}{\langle I(t) \rangle^2}. \quad (3.7)$$

The equation 3.7 is reduced by the fact that the mean values of the fluctuation are zero.

$$G(\tau) = 1 + \frac{\langle \delta I(t + \tau) \cdot \delta I(t) \rangle}{\langle I(t) \rangle^2} \quad (3.8)$$

The 3D-diffusion auto-correlation function is generated from the intensity profile of the PSF (equation 3.1) and by the assumption that the intensity fluctuation is only affected by the diffusion of particles. The 3D-diffusion auto-correlation function

is

$$G(\tau) = 1 + \frac{\gamma}{N} \left(\frac{1}{1 + \tau/\tau_d} \right) \left(\frac{1}{1 + (\omega_1/\omega_2)^2 (\tau/\tau_d)} \right)^{0.5}, \quad (3.9)$$

with γ as a correction factor for the intensity profile in the focus^[150] and the fit to a measured auto-correlation function resulted in the diffusion time (τ_d).^[149,151,152]

The diffusion from lipids in membranes takes only place in 2D and not 3D, so the 3D auto-correlation is reduced by reducing the PSF from an ellipsoid to a plane orthogonal to the optical axis.^[150]

$$G(\tau) = 1 + \frac{\gamma}{N} \left(\frac{1}{1 + \tau/\tau_d} \right). \quad (3.10)$$

The diffusion constant (D) of the lipids is calculated from the 2D-diffusion time (τ_d) with

$$\tau_d = \frac{\omega_1^2}{4D}. \quad (3.11)$$

This equation is only correct if the PSF is known and if the membrane is in the mid-plane of the PSF. Then the short half axis of the PSF (ω_1) is equal to the radius of the cylinder. To overcome this specification, Z-scan FCS can be performed. Z-scan FCS uses the fact that the diffusion time depends quadratically on the Z-position of the PSF.^[150]

$$\tau_d(\Delta z) = \frac{\omega_1^2}{4D} \left(1 + \frac{\lambda_0^2 \Delta z^2}{\pi^2 n^2 \omega_1^4} \right) \quad (3.12)$$

The diffusion constant (D) and the short half axis of the PSF (ω_1) can now be calculated from a quadratic fit of the different calculated diffusion times (τ_d) at different Z-positions ($\Delta z = z - z_0$). z_0 is equal to the minimum of the fitting curve. The laser wavelength (λ_0) and the reflective index of the solution (n) is set up.^[150] The short half axis of the PSF (ω_1) can also be controlled by the numbers of diffusion particles in dependency of the Z-position with the averaged concentration of diffusion fluorescent molecules (c).

$$N(\Delta z) = \pi c \omega_1^2 \left(1 + \frac{\lambda_0^2 \Delta z^2}{\pi^2 n^2 \omega_1^4} \right) \quad (3.13)$$

The measurement and calculation of the diffusion coefficient with FCS

The auto-correlation function at different Z-positions are measured and the equation 3.12 can be fit with different diffusion times and different Z-positions.

The use of an upright fluorescence microscope has the disadvantage that the mechanical focus drift cannot be corrected by a stabilized focus which measures the

reflection beam of a second laser at the cover slide. The mechanical focus drift must be inhibited. This was done by using a metal measurement chamber.

To increase the reliability of the measurement, the auto-correlation was measured five times for 2 min at each Z-position. The fit of the 2D auto-correlation function (equation 3.10) is weighted with the errors of the lag time ($\sigma(\tau)$)

$$\sigma(\tau) = \sqrt{\frac{1}{L(L-1)} \sum_{l=1}^L \left(\frac{G_l(\tau) - G_l(\infty)}{G_l(0) - G_l(\infty)} - \frac{1}{L} \sum_{l=1}^L \frac{G_l(\tau) - G_l(\infty)}{G_l(0) - G_l(\infty)} \right)^2}. \quad (3.14)$$

L describes the number of measurements at the same position with the index (l). $G_l(\infty)$ and $G_l(0)$ are estimated by averaging of long and short delay times respectively.^[150] This calculated error is used to get a precisely fitted 2D-diffusion auto-correlation with the χ^2 method^[153]

$$\chi_{\text{Autocorrelation}}^2 = \sum_i \left(\frac{G(\tau_i) - \overline{G(\tau_i)}}{\sigma(\tau_i)} \right)^2. \quad (3.15)$$

The χ^2 evaluation is also used for the Z-scan FCS fit (equation 3.12) with the error of the auto-correlations fit ($\chi_{\text{Autocorrelation}}^2$) at the different Z-positions (Δz).

$$\chi_{\text{Z-scan FCS}}^2 = \sum_i \left(\frac{\tau_d(\Delta z_i) - \overline{\tau_d(\Delta z_i)}}{\chi_{\text{Autocorrelation}}^2(\Delta z_i)} \right)^2 \quad (3.16)$$

The diffusion constant (D) is calculated from the Z-scan FCS fit (equation 3.12).

3.3.2. Interferometric scattering microscopy

Interferometric scattering microscopy (iSCAT) was used to determine the diffusion constants from the f-PSM and solid supported PSM (s-PSM) on the 6MH on gold (6MH-Au) and plasma cleaned silicon nitride (p-Si₃N₄) functionalized substrates. The measurements were performed by Dr. Susann Spindler in the group of Prof. Dr. Vahid Sandoghdar (Max Planck Institute for the Science of Light, Erlangen). The analyzed lipids (1,2-dioleoyl-sn-glycero-3-phosphoethanolamine-N-cap-biotinyl (cb-DOPE)) were labeled with GNPs. The lipid GNP connection was over a biotin streptavidin binding. Light was reflected not only by the GNP but also from the cover slide and the porous substrate. The reflected light from the GNP interferes with the reflected light from the substrate or cover slip. The light intensity was measured with a camera. The position of the GNP was shown by a 2D-Gaussian curve in the light intensity images. This was fitted and the position of the GNPs were

connected to a trajectory. The diffusion constant was calculated with the covariance-based estimation (CVE), this had the advantage that the fitting errors of the GNP position were considered.^[154]

Preparation of the iSCAT measurement

The PSMs were prepared as previous described (section 3.2.3), with PBS in a petri dish. The prepared PSMs were incubated with the 20 or 40 nm GNPs for 30 min. Then the substrate was transferred to the measured chamber, filled with PBS. This chamber had two gold spacers with a thickness of ~ 200 nm. The flipped substrate were placed, so that between the membrane and the cover slide a buffer film of 200 nm were. Thus substrates were measured at a home build inverse microscope in Erlangen.^[147] The membrane patch were found with the microscope and the ATTO532-1,2-dioleoyl-*sn*-glycero-3-phosphoethanolamin (ATTO532-DOPE) fluorophore. The length of one video was 5 s by a frame rate of 1 kHz.

3.3.3. Atomic force microscopy

An atomic force microscopy (AFM) uses a cantilever to detect height differences in the nm regime or forces in the pN regime. A cantilever can be described with Hooke's law

$$F = k\Delta x. \quad (3.17)$$

The measured force (F) is proportional to the cantilever stiffness (k) and the deflection of the cantilever (x).^[149] The deflection of the cantilever is in the sub nm regime. The accuracy of the small deflections from the cantilever is achieved by reflecting a laser beam from the backside of the cantilever onto a 4-quadrant diode.

AFM can be used for surface topography images or force measurements. The quantitative imaging (QI) mode was used in this work to measure a surface topography from the PSMs. The principle of this mode is to measure a force distance curve up to the maximum force setting and than retract the cantilever to a set distance length at each pixel. The advantage of this mode is that shear forces which can be set to scanning the probe are minimized, because the cantilever indents the probe only from the top and not from the side.

Measurement of membrane tension

The membrane tension of PSMs was measured by AFM. PSMs were prepared, as previously described (section 3.2.3), with PBS in a petri dish and fixed with an

adhesive tape. The center of the microscope images and the center of the topographic images were aligned by using a home-build calibration cross. A membrane patch was found with the fluorescence microscope and a QI topography image was taken with the AFM of the patch. f-PSMs were identified in the QI images. At the center of the f-PSMs, new force indentation curves were taken, to calculate the membrane tension.

The membrane tension of the f-PSM was extracted from the force indentation curves by fitting

$$F = 2\pi R\sigma_z \frac{u'(R)}{\sqrt{1 + u'(R)^2}}. \quad (3.18)$$

The measured force F depends on the radius of the f-PSM (R). The membrane surface geometry ($u(R)$) is calculated from the indentation depth (z). The membrane tension (σ) is extracted from

$$\sigma_z = \sigma + K_A \frac{\Delta A}{A_0}. \quad (3.19)$$

The increased membrane area ($\Delta A/A_0$) multiplied with the area compressibility modulus (K_A) affected the σ upon the indentation. This fitting neglects the bending of the membrane, because the pore radius is greater than the membrane thickness by a factor of >100 .^[155]

3.3.4. Surface plasmon resonance

Surface plasmon resonance (SPR) is used in many applications in order to analyze molecular interactions. In this work, the dissociation constant (K_d) of STxB Gb₃ was measured with SPR. To measure the binding, the receptor molecule (Gb₃) is fixed to a sensor surface. The binding partner (STxB) is rinsed over the surface. The change of refractive index near the surface is time-dependently detected and reflects the binding of STxB to Gb₃.

The refractive index near the surface is detected via the surface plasmon resonance frequencies. The surface plasmon are stimulated by a total reflected laser beam in a certain angle to the optical axis. By changing the angle of the laser beam the intensity of the surface plasmon changes and the reflective light of the laser varied. At the specific angle which represents the surface plasmon resonance frequencies the reflective light is at a minimum. The change of the reflective index near the surface changes the surface plasmon resonance frequencies, which changes the angle of the minimum from the reflected laser light. This change in the angle was measured time dependent.^[149]

The SPR experiment

40 nm gold coated SPR chips were incubated in a 1 mM octanethiol solution over night to generate a hydrophobic self-assembled monolayer (SAM). A SPR chip was set up into the system and the measurement chambers were rinsed with buffer. The system had two different channels, the analytic and control channel. To avoid systematical errors like temperature fluctuation, the reflective units from both channels were measured and subtracted ΔRU , fist correction.

SUVs with the lipid composition DOPC/ Gb_{3porc} (95:5) were rinsed only over the analytic channel for 30 min. The reflective index changed by spreading the SUVs on the functionalized SPR chips which is seen by the increase of the ΔRU in figure 3.1 A starting at the injection 1. The control SUVs composed of DOPC were rinsed over both channels, the analytic channel and the control channel, for 30 min. The possible spreading of the SUVs is seen by a decrease of the ΔRU , because the reflective index of the control channel changes due to the fact that the vesicles spread to the surface (figure 3.1 A, 2). To remove multi lamellar membrane stacks, a 50 mM NaOH solution was rinsed over both channels five times for 2 min (figure 3.1 A, 3-7). After removing the multi lamellar membrane stacks, the surface of the SPR chip is full of a membrane monolayer. In the analytic channel, the receptor lipid was incorporated into the membrane on the surface. In the control channel, a DOPC membrane was spread on the surface.

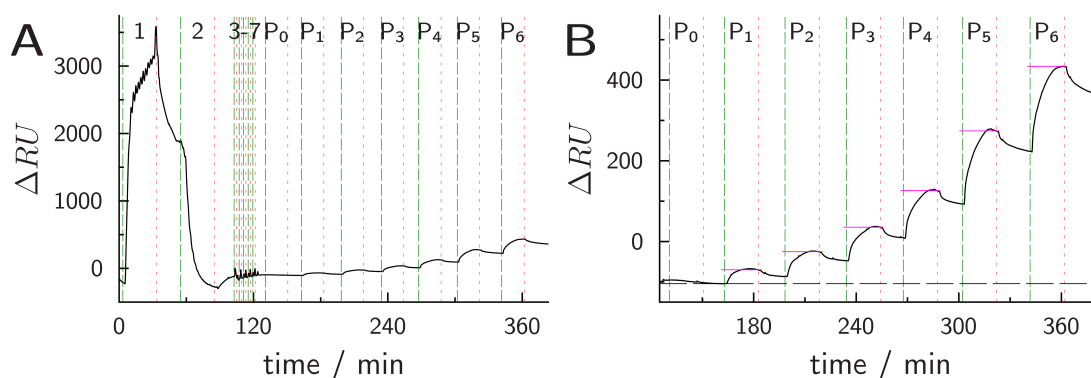


Figure 3.1.: A complete surface plasmon resonance (SPR) measurement with the different injection (1-7 and P₀₋₆). The reflective index of the analytic channel was corrected by the control channel (ΔRU) and plotted against the time. The complete measurement is shown in A) with the insertion of the analytic vesicles (1), the control vesicles (2) and five steps of rinsing with NaOH (3-7). The addition of different protein concentration (P₀₋₆) starting with a control, adding only buffer (P₀). In B, a zoom into the protein addition is shown and the cumulative analysis is illustrated by the horizontal black line and the magenta lines in the different protein additions, the differences are the measured values.

The measurement starts with a control, only buffer was rinsed over the prepared membrane with the same settings as protein injection, to see the influence of the injection (figure 3.1, P₀). Different protein concentrations were rinsed afterwards over the membrane, starting with the lowest one (figure 3.1, P₁-P₆).

The analysis of the dissociation constant can be done with the second correction method. The buffer injection will be subtracted from each protein injection and plotted together. For this analysis, it must be clear that the protein will fully take off from the surface, but this is not the case for STxB Gb₃ binding. To overcome the not 100% take off of the protein, the SPR time trace was cumulatively analyzed. The values before the first protein injection were the reference ΔRU (figure 3.1 B, black broken line). The difference from the reference ΔRU to the ΔRU at the end of each protein measurement (figure 3.1 B, cyan line in P₁-P₆) is the reflectivity change and can be fitted with the protein concentrations to a Langmuir adsorption isotherm

$$R_{rel} = \frac{R_{rel,max}c(\text{STxB})}{K_d + c(\text{STxB})} \quad (3.20)$$

in order to calculate the dissociation constant (K_d). To compare different measurements, the relative reflectivity change was calculated by normalizing to a protein concentration of 300 nM, $R_{rel} = 1$.

3.4. Data evaluation

3.4.1. Phase distribution in GUVs

In this work, the phase preference of fluorescently labeled Gb₃s was measured and analyzed (results in chapter 4.2.2 and 4.2.3). Phase-separated GUVs were prepared as described in chapter 3.2.1. 60–100 μL of prepared GUV solution was sedimented through a 5 mL pipette tip filled with PBS into a bovine serum albumin (BSA) passivated petri dish for 2 min. Afterwards, GUVs were measured with the CLSM. A Z-stack was measured from the GUVs and two fluorophores are recorded in separated channels. One channel represents the fluorescence intensity of the labeled Gb₃s and the second channel shows the fluorescence intensity of the l_d phase marker (Dy731-DOPE).^[141]

The analysis of the labeled Gb₃ distribution in phase-separated GUVs was done with a custom written Matlab script. The measured Z-stacks were measured at different CLSMs with different data structures. These data structures were aligned so that there was no need to rewrite the Matlab script for the different CLSMs.

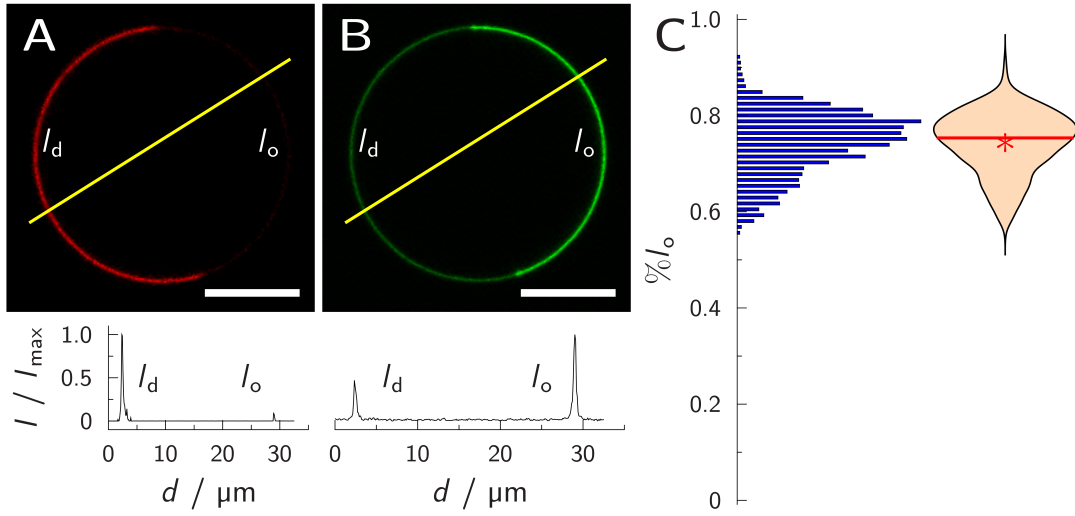


Figure 3.2.: Confocal images of a phase-separated GUV composed of DOPC/ SM_{porc} /Chol/ $Gb_3PEG_{13}C_{24:0}H$ /Dy731-DOPE (39:39:20:1:1). A) Dy731-DOPE fluorescence (red); B) $Gb_3PEG_{13}C_{24:0}H$ fluorescence (green). The yellow lines indicate where the fluorescence intensity profiles (bottom images) have been obtained. From the intensity profiles, liquid ordered phase distribution ($\%l_o$) = 0.682 was calculated for $Gb_3PEG_{13}C_{24:0}H$. C) Histogram and corresponding violin plot obtained from 60 GUVs with 2525 individual analyzed profile lines with the composition as in A. The red solid line indicates the median value, the red star the mean value. Scale bar 10 μm .

To achieve an unbiased data evaluation, the profile lines of each GUV slide from the GUV stacks was set manually only in the phase marker channel (Dy731-DOPE, figure 3.2 A) Every profile line crosses the GUV twice. One time in the l_o phase and the second time in the l_d phase, and it crosses the center of the GUV to overcome polarization effects (figure 3.2, yellow line). These profile lines were analyzed in both channels of the same GUV slide (figure 3.2 A and B). The intensity ($I(d)$) of the profile line was fitted against the position (d) of the profile line with a two-peak Gaussian fit, each peak for one membrane crossing.

$$I(d) = a_1 \exp\left(\left(\frac{d-b_1}{c}\right)^2\right) + a_2 \exp\left(\left(\frac{d-b_2}{c}\right)^2\right) + e \quad (3.21)$$

The fit parameter a_1, a_2 describes the amplitude or maximum intensity of the peaks, b_1, b_2 the position of the peaks, c the peak width which is equal for both peaks, because the membrane thickness around the GUV is the same. e describes the background intensity. The peak with the maximum intensity from the Dy731-DOPE profile represents the l_d phase peak. This was used to select the phases in the analyzed labeled Gb_3 intensity profile in order to calculate the l_o phase distribution ($\%l_o$). The ratio between $I(l_o)$ and the total intensity of both phases allows the determination of the

proportion of labeled Gb₃.

$$\%l_o = \frac{I(l_o)}{I(l_o) + I(l_d)} \quad (3.22)$$

This analysis was done for several GUVs. The preparation was also done on different preparation days. To see the distribution of the %*l*_o, the data was plotted in a histogram and for a better comparison it was also plotted as a violin plot (figure 3.2 C).

For the statistical analysis of the labeled Gb₃s (chapter A.7), a linear mixed-effects model (LMM) was fitted to the whole %*l*_o data

$$\%l_o = X\beta + Zu + \epsilon, \quad (3.23)$$

in order to evaluate the effects of the different chemical properties of the labeled Gb₃s. The effects of the measured %*l*_o of a phase-separated GUV are listed in the vectors of fixed effects β and the random effects u . The fixed effects describe the effect of the different chemical properties from the labeled Gb₃ such as the different fatty acids, to the %*l*_o. The random effects describe systematic distributions such as the influence of the GUVs population from each day to the %*l*_o or the distribution of the %*l*_o in one GUV. The description to which group the measured data belongs is listed in the coefficient matrix of the fixed effect X and random effect Z . At least, a vector of random error (ϵ) was added.

Equation 3.23 was solved with the maximum likelihood estimation which optimizes the equation in the way that the different random effects as well as the random error are normally distributed with a mean value of zero. The results and the different LMM equations are summarized in chapter A.7.

3.4.2. Phase separation on PSMs

In this thesis, phase separation of PSMs was measured and analyzed in dependence of temperature and lipid mixture. The results of this study can be seen in chapter 5.2. The lipid mixture varied in the Chol content from 0 to 50 mol% in a DOPC/SM 1:1 matrix. The measurement was performed with a CLSM within a temperature-control chamber.^[156] The prepared PSMs (chapter 3.2.3) on top of a silicon oxide (SiO_x) functionalized substrate were heated and cooled between 25 and 55 °C. One measurement series was done on one membrane patch, either heated or cooled. The series consists of several images taken at certain temperatures. Different series were measured on one substrate with the same Chol concentration in the GUV solution.

The taken images are composed of two different channels. The channels display the intensity of the phase markers BODIPY-Chol and TexasRed-DHPE. There are two possibilities of phase separations located in the PSM within the measured phase diagram (figure 3.3). Firstly, the PSM phase-separated into the gel like (l_β)/ l_d phase at low temperature and, at high temperature, it is homogeneous in the l_d phase. Secondly, at low temperature, the phase separation is between the l_o / l_d phase. The phase separation was analyzed by eye for each series, comparing the images with the illustration in figure 3.3.

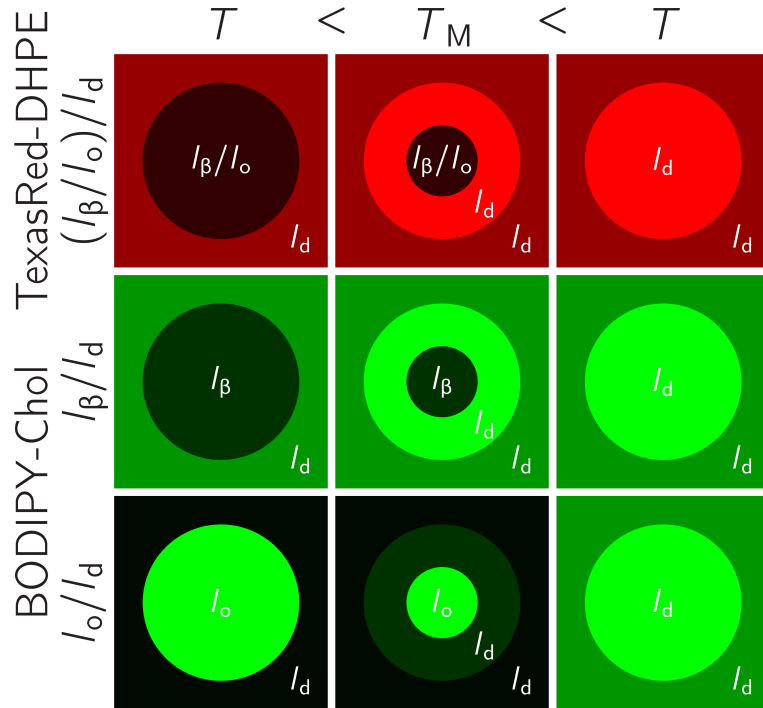


Figure 3.3.: The two different phase separations are illustrated with the different intensities of the two different fluorophores sulforhodamine-1,2-dihexanoyl-*sn*-glycero-3-phosphoethanolamine (TexasRed-DHPE) (red, upper line) and 23-(dipyrrrometheneboron difluoride)-24-norcholesterol (BODIPY-Chol) (green, bottom lines) in the pore-spanning membranes (PSMs). The membrane is phase separated at temperature lower than the transition temperature (T_M) in the gel like (l_β)/liquid disordered (l_d) or liquid ordered (l_o)/ l_d phase separation. At higher temperature than the T_M the PSM is homogeneous in the l_d phase.

In the measurements and the illustration, the channel of TexasRed-DHPE is not influenced by the type of phase separation. It represents the l_d phase, which is at lower temperature as the transition temperature (T_M) always in the s-PSM and at higher temperature homogeneously distributed in the PSM. Therefore, this channel was used to identify the T_M of each series.

3. Materials and methods

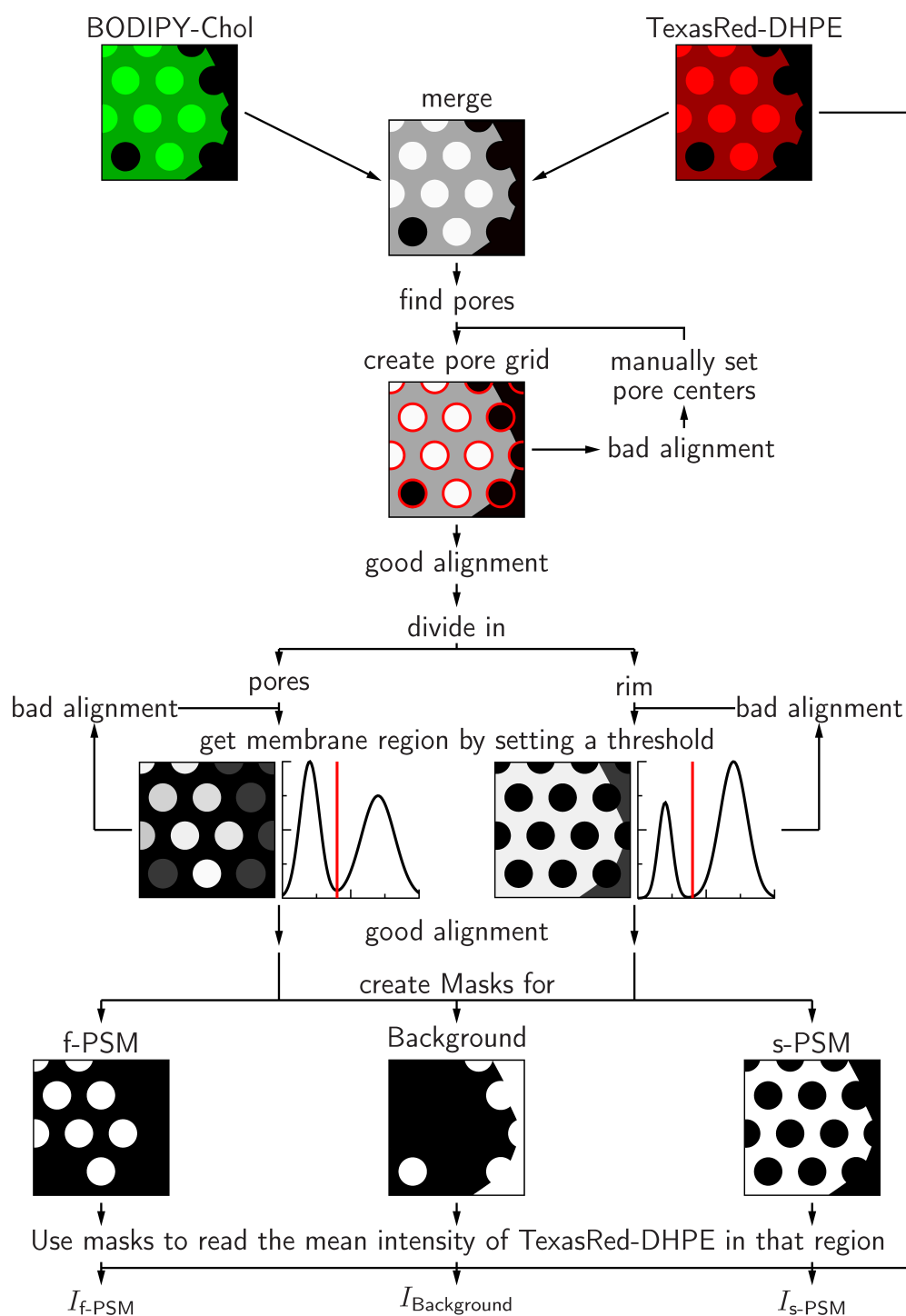
In the first step, each fluorescence micrograph from all the temperature series and lipid compositions was separately analyzed to extract the intensity ratio of the f-PSM to the s-PSM. This was done with a custom designed Matlab-script. The analysis of the image sequence was performed in random order to avoid systematical errors from the user. The fluorescently micrograph analysis is schematically shown in scheme 3.13.

The two channels of the fluorescence micrograph show the fluorescence intensity of BODIPY-Chol and TexasRed-DHPE (scheme 3.13). To divide the fluorescence micrograph into the pore and rim regions, the channels were merged and smoothed with a median filter. The pore localization in the merged fluorescence micrograph was automated. Pores were not always identified as a circular object. Unidentified pores were extrapolated with the conditions of hexagonal pore orientation and equidistant spacing between the pores (scheme 3.13). As a control of the algorithm, the result was checked by visual judgment. If the calculated pore mask did not fit into the merged image (bad alignment), some pore centers had to be set manually, while the rest were extrapolated (scheme 3.13). The well aligned pore mask was used to separate the regions of the pores and the rim. The membrane areas (f-PSM and s-PSM) in both regions were found by threshold analysis. For that, an intensity histogram of the pore region or the rim region was created in order to have a decision guide for the threshold setting. Each pixel with an intensity above the threshold belongs to the membrane area, whereas each pixel with an intensity below the threshold belongs to the non membrane region, the so-called background. The generation of the f-PSM mask was shape constrained, because pores can only be completely spanned by membrane or not. This condition was realized with a filling parameter. If the amount of pixels which were higher than the threshold was greater than the filling parameter, the whole pore was included in the f-PSM mask, and if not the whole pore was included in the background mask. The mean intensity (I) of the TexasRed-DHPE channel was read out for the different areas by using these masks (f-PSM, Background, s-PSM). Afterwards, the intensity ratio

$$\frac{I_{\text{f-PSM}}}{I_{\text{s-PSM}}} = \frac{I_{\text{f-PSM}} - I_{\text{Background}}}{I_{\text{s-PSM}} - I_{\text{Background}}}. \quad (3.24)$$

was calculated from the mean intensities of the TexasRed-DHPE channel.

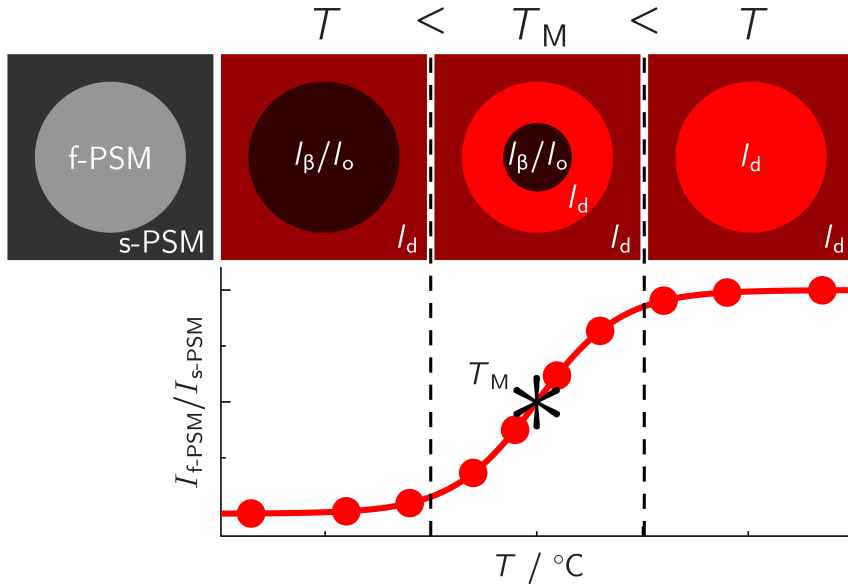
The calculated intensity ratio of one series were plotted against the temperature (T) from the measured temperature ramp (figure 3.14). The T_M is the tuning point of a sigmoidal curve,^[104] which was fit with



Scheme 3.13.: The process chart for the image intensity calculation. The two channels of the fluorescence image were merged to calculate the pore mask. The pore and rim regions were extracted and separately analyzed to get the masks of the membrane areas (freestanding pore-spanning membrane (f-PSM), solid supported pore-spanning membrane (s-PSM)). The non membrane areas were collected and assigned to the background. These masks were utilized to gain the mean fluorescent intensities of the specific regions from the TexasRed-DHPE fluorescence image (I_{f-PSM} , $I_{Background}$ and I_{s-PSM}).

$$\frac{I_{f\text{-PSM}}}{I_{s\text{-PSM}}}(T) = I_{\text{end}} + \frac{I_{\text{start}} - I_{\text{end}}}{1 + \exp\left(\frac{T - T_M}{dT}\right)}. \quad (3.25)$$

The width of the transition (dT) describes the transition temperature range. The intensity ratio at low temperature is described through I_{start} and the intensity ratio at high temperature is I_{end} .



Scheme 3.14.: A schematically illustration of how to get the transition temperature (T_M) of a temperature series from pore-spanning membranes (PSMs). The intensity ratio $I_{f\text{-PSM}}/I_{s\text{-PSM}}$ is plotted against the temperature. The turning point is the T_M . The intensity ratio of the PSMs at three temperatures is illustrated above as fluorescence micrograph.

The measured T_M values of all samples with equal Chol concentration were averaged and plotted against the Chol concentration, as phase diagram.

4. Labeled globotriaosyl ceramides (Gb₃s) and their phase behavior in phase-separated membranes

In this thesis, the phase preference of the receptor lipid globotriaosyl ceramide (Gb₃) was analyzed before shiga toxin (STx) binding. This aspect was investigated using phase-separated giant unilamellar vesicles (GUVs) and fluorescently labeled Gb₃s. The B-subunit of STx (STxB) binds the natural Gb₃ in the liquid ordered (*l_o*) phase of phase-separated membranes.^[54] Furthermore, the STxB binding preference was tested for the fluorescently labeled Gb₃s. Gb₃s in cell membranes differ in fatty acid length, saturation and α -hydroxylation. Different fatty acids were analyzed to observe the influence of the fatty acids on the phase preference of the Gb₃s and the binding preferences of STxB.

At first, different STxBs samples were analyzed with respect to the binding properties to Gb₃. Afterwards, the phase preference of the different fluorescently labeled Gb₃s was investigated. Fluorescent properties of each fluorophore were measured with the fluorimeter. Then the phase behavior of the different labeled Gb₃s was analyzed, starting with the fatty acid labeled Gb₃s and ending with the study of the head group labeled Gb₃s.

4.1. Binding studies of STxB to its receptor lipid Gb₃

Three different STxB samples¹ were available to analyze the phase preference of Gb₃ after STxB binding. The STxB binding to Gb₃ and their purity was analyzed. The data from the STxB sample B were published in: Bosse M., **Sibold J.**, Scheidt H. A., Patalag L. J., Kettelhoit K., Ries A., Werz D. B., Steinem C. & Huster D. Shiga Toxin Binding Alters Lipid Packing and Domain Structure of Gb₃-Containing

¹The STxB samples A and C were purified by the group of Prof. Dr. Winfried Römer and B by the group of Prof. Dr. Daniel Huster (chapter 3.1.4)

4. Phase behavior of globotriaosyl ceramide (Gb₃)

Membranes: A Solid-State NMR Study. *Phys. Chem. Chem. Phys.* **21**, 15630–15638 (2019).

The purity of three different STxB samples was analyzed with a 16% Schagger gel using two protein marker rows (Marker 1 *ultra low range marker* and Marker 2 *PageRuler™*) and three different STxB preparations (figure 4.1). Both markers showed an exponential correlation from the molecular weight to the migration distance (seen as line, because the molecular weight is logarithmic plotted).

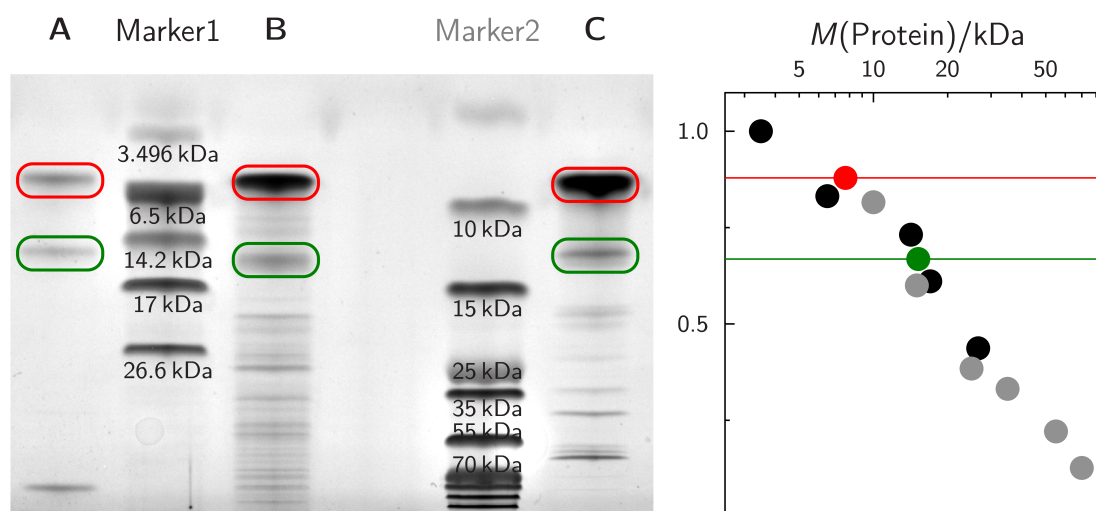


Figure 4.1.: A 16% Schagger gel with the three different B-subunits of shiga toxin (STxB) samples (A, B and C). To clarify the mass of the STxB two different protein markers were used: Marker 1 *ultra low range marker* and Marker 2 *PageRuler™*. In red the protein bands of STxB are highlighted and in green the cluster of STxB. Beside the gel, the relative migration distances of the protein markers (Marker 1 black and Marker 2 grey) were plotted against the protein weights, showed in a logarithm scale. The two protein bands are also incorporated into the plot and the molecular weight of STxB (red dot) and the doubled weight (green dot) are marked.

The 16% Schagger gel shows that the protein bands with the highest intensities in all three samples (A, B and C) is marked in red (figure 4.1). The migration distance was plotted as red line and the calculated molecular weight of STxB (7.7 kDa)^[50] as red dot in the relative distance weight plot (figure 4.1). The molecular weight of STxB and the migration distance were in good agreement to the protein markers. These bands were assigned to STxB. In all three STxB samples, a second protein band was visible marked in green (figure 4.1). The migration distance was plotted as a green line in the distance weight plot. The molecular weight of the STxB dimer (15.4 kDa) was plotted as a green dot, which seemed to be in good agreement with the protein markers. However, the green marked bands were referred as STxB dimer.

The different protein samples showed distinct amounts of impurities. The isolation A revealed one additional band with a molecular weight higher than 70 kDa. The STxB purification B showed several weak protein bands greater than 10 kDa being presumably impurities. STxB isolation (C) has seven weak bands between 18 and 70 kDa.

The STxB binding to Gb₃ was studied with adsorption isotherm measurements, performed by surface plasmon resonance (SPR) spectroscopy. A lipid monolayer composed of DOPC/porcine erythrocytes Gb₃ (Gb_{3porc}) (95:5) was spread on a hydrophobic (octan-1-thiol on gold (OT-Au)) functionalized SPR chip and the binding of different STxB concentrations were measured (R , detailed experiment set up in chapter 3.3.4). The data was normalized according to 300 nM STxB (R_{real}) to allow a comparison of different experiments. The dissociation constant (K_d) is extracted by fitting the Langmuir adsorption isotherm

$$R_{\text{real}} = \frac{R_{\text{real max}} \cdot c(\text{STxB})}{c(\text{STxB}) + K_d} \quad (4.1)$$

to the data (figure 4.2). The concentration of STxB ($c(\text{STxB})$) is the monomer concentration. The K_d values for the different STxB samples are listed in (table 4.1).

The K_d values range from 13 to 35 nM (figure 4.2, table 4.1) which reflects a high binding affinity for all three STxB samples. In figure 4.2 D, the fits of all three STxB samples are compared. The STxB sample B has the highest affinity to the receptor lipid which is represented in the lowest K_d value of 12.9 ± 3.2 nM. The STxB sample A and C have K_d values of 17.4 ± 2.5 and 34.7 ± 5.6 nM respectively. The binding affinity of the STxB samples A and B are comparable. The sample C showed a two times lower binding affinity to Gb₃.

Table 4.1.: Dissociation constants (K_d) for the different STxB samples. The errors are the standard deviation calculated from the fit. The number of repeated adsorption isotherms are also listed.

STxB sample	K_d [nM]	number of scans
A	17.4 ± 2.5	4
B	12.9 ± 3.2	2
C	34.7 ± 5.6	3

K_d values for the STxB binding to cells are typically in the nM regime.^[52,157–159] Schütte *et al.* measured STxB Gb₃s binding affinities with a similar system using defined Gb₃-species with different fatty acids in contrast to Gb₃ mixture (Gb_{3porc}) used in the experiments presented here. Their K_d values were in the range of 40 to

4. Phase behavior of globotriaosyl ceramide (Gb_3)

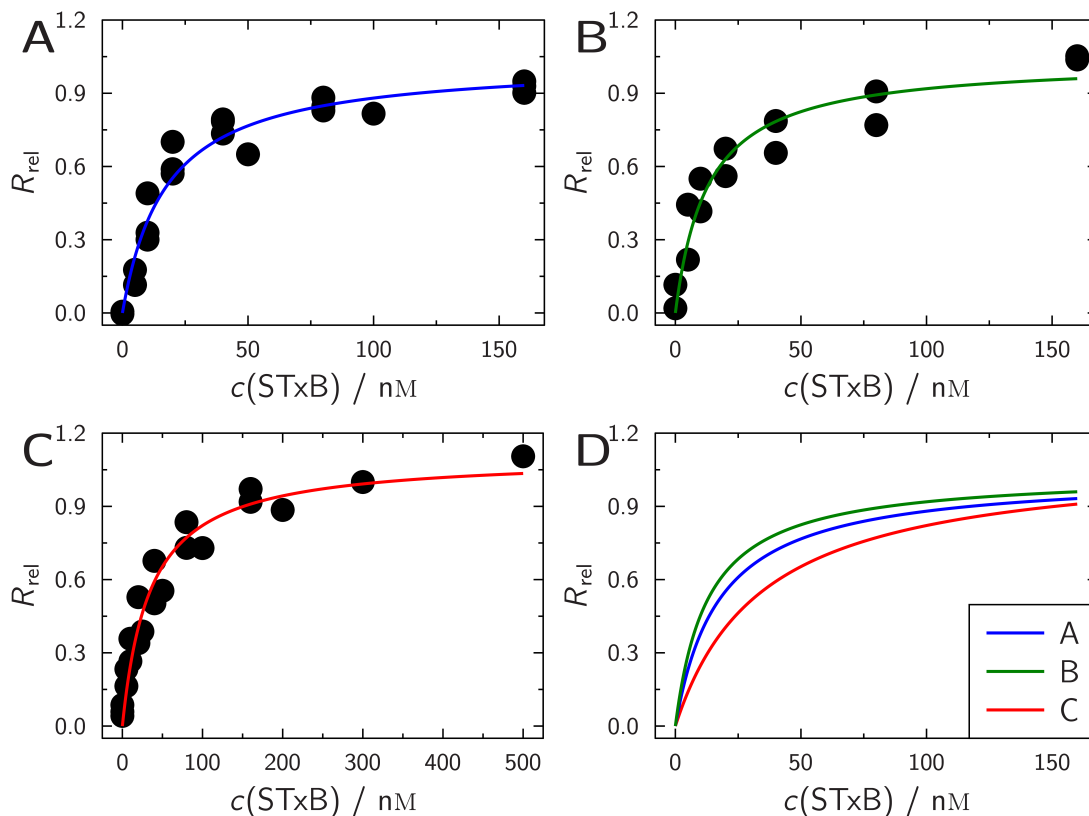


Figure 4.2.: Adsorption isotherm of three different B-subunit of shiga toxin (STxB) samples (A, B and C) bound to membranes composed of DOPC/ $\text{Gb}_{3\text{porc}}$ (95:5). Langmuir adsorption isotherm (solid line) were fitted to the data and the dissociation constant is summarized in table 4.1. The fitted Langmuir adsorption isotherms are compared in D.

70 nM.^[160] In an other binding study, performed by Head *et al.*, the binding of STxB to Gb_3 in microtiter wells was measured.

All three STxB samples show high binding affinities to Gb_3 , comparable to values found in literature. To enhance comparability, the STxB sample C was used in further experiments because this purification had the largest yield.

4.2. Analysis of the phase preference of labeled Gb_3

STxB binding was studied at cellular membranes as well as biomimetic model systems.^[157,162] The cellular membrane is very heterogeneous in terms of lipid composition and membrane structure. In the last two decades, nanoscaled domains differing in lipid composition with a higher order packing density have been discussed as functional units called lipid rafts. To mimic such domain structures, biomimetic models utilize lipid mixtures which phase separate in a l_o , raft-like domains, and a liquid disordered (l_d) phase. In studies using GUVs, the Gb_3 s showed preferential

binding of STxB to the l_o phase in lipid mixture consisting of DOPC/sphingomyelin (SM)/cholesterol (Chol)/Gb_{3porc} (40:35:20:5).^[54] From this observation, it can be concluded that Gb₃ is enriched in the l_o phase after binding.^[160,162] However, it is not clear, where Gb₃ is located in phase-separated membranes before STxB binding. To get information about the phase distribution of Gb₃ before STxB binding, fluorescently labeled Gb₃s were synthesized in the group of Prof. Dr. Daniel B. Werz (TU Braunschweig, Institut für Organische Chemie, Braunschweig (Germany), scheme A.1). Their phase preference was investigated in phase-separated GUVs. One solution was the design of fluorescently labeled fatty acids with pentaene or hexaene moieties which are connected to the Gb₃ (figure 3.11). These results are published in: Patalag L. J., **Sibold J.**, Schütte O. M., Steinem C. & Werz D. B. Gb₃ Glycosphingolipids with Fluorescent Oligoene Fatty Acids: Synthesis and Phase Behavior in Model Membranes. *ChemBioChem* **18**, 2171–2178 (2017). The second solution was to connect the fluorophore to the second sugar of the Gb₃ with a polyethylene glycol (PEG) linker in between (figure 3.12). These results are submitted as: **Sibold J.**, Kettelhoit K., Vuong L., Liu F., Werz D. B. & Steinem C. Synthesis of Head Group Labeled Gb₃ Glycosphingolipids and Their Distribution in Phase-Separated Giant Unilamellar Vesicles. *Angew. Chem. Int. Ed.* **58**, 17805–17813 (2019). In this study, the fluorescent properties of the Gb₃s derivatives were determined as well as their preferential phase distribution in biomimetic membranes.

4.2.1. Fluorescent properties of labeled Gb₃s

The fluorescently labeled Gb₃s used in this work are divided in two categories, fatty acid labeled Gb₃s and head group labeled Gb₃s (scheme A.1). Two different fatty acid labeled Gb₃s, the Gb₃ phenyl-modified fatty acid (Gb₃PH) and Gb₃ thienothieryl-modified fatty acid (Gb₃TT) (scheme 3.11), were analyzed. Additionally, eight different head group labeled Gb₃s were used (scheme 3.12). All the eight different head group labeled Gb₃s had a BODIPY as fluorophore and Gb₃PEG₁₃C_{24:0}H was exemplary analyzed. Absorption and emission spectra were measured by fluorimetry to determine the fluorescent properties of the Gb₃s. Therefore, GUVs composed of DOPC/Gb₃ (99:1) were prepared for all Gb₃ derivatives. The amount of lipids in the analyzing solution was 16 μM, determined by the phosphor concentration of the GUV solution.

The excitation spectra of the fatty acid labeled Gb₃s were measured at an emission wavelength of 465 nm (figure 4.3 A and B, red line). Gb₃PH showed two maxima at 347 and 366 nm and a shoulder at 330 nm (figure 4.3 A, red line). Gb₃TT showed

4. Phase behavior of globotriaosyl ceramide (Gb_3)

two peaks at 369 and 391 nm (figure 4.3 B red line). The excitation spectra of the head group labeled Gb_3 were measured at the emission wavelength of 580 nm. The excitation range of BODIPY is from 460 to 520 nm with a maximum at 506 nm (figure 4.3 C red line).

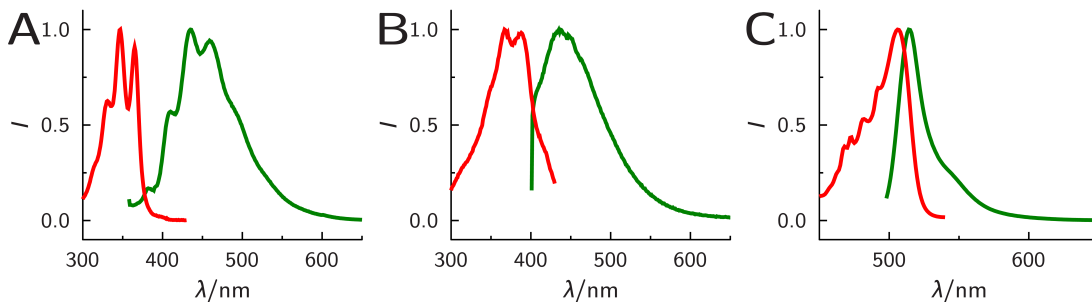


Figure 4.3.: Excitation (red) and emission (green) spectra of labeled globotriaosyl ceramides (Gb_3 s) in GUVs composed of DOPC/ Gb_3 (99:1). The lipid concentration in the cuvette was set to 16 μM . The fluorescence excitation spectra were measured from $\lambda = 300$ to 430 nm, with $\lambda_{\text{em}} = 465$ nm for Gb_3PH (A) and Gb_3TT (B) and from $\lambda = 450$ to 540 nm, with $\lambda_{\text{em}} = 580$ nm for $\text{Gb}_3\text{PEG}_{13}\text{C}_{24:0}\text{H}$ (C). Fluorescence emission was excited at A) $\lambda_{\text{ex}} = 348$ nm, recorded from $\lambda = 360$ to 650 nm, B) $\lambda_{\text{ex}} = 391$ nm, recorded from $\lambda = 400$ to 650 nm and C) $\lambda_{\text{ex}} = 488$ nm, recorded from $\lambda = 500$ to 650 nm.

The emission spectrum of Gb_3PH was measured with excitation at 348 nm, resulting in a broad range from 400 to 600 nm with two peaks at 434 and 458 nm and a shoulder at 410 nm (figure 4.3 A green line). The intensity maximum is at 434 nm. The excitation wavelength for the emission spectrum Gb_3TT was 391 nm. The emission of Gb_3TT showed a broad range from 400 to 600 nm, with a maximum around 450 nm (figure 4.3 B green line). The exemplarily measured head group labeled Gb_3 was excited at 488 nm and showed a peak from 500 to 570 nm with a maximum at 514 nm (figure 4.3 C green line).

The excitation spectra of the fatty acid labeled Gb_3 s show typical bands for the vibrational resolution of polyene chromophores.^[163] The excitation spectra as well as the emission spectra of the fatty acid labeled Gb_3 s are red shifted compared to the excitation and emission spectra of sphingosine-like chain containing a pentaene^[164] which is a result of the addition from the ring structures. The red shift of the Gb_3TT compared to Gb_3PH is a result of the thiophene group instead of the phenyl ring.

The excitation and emission spectra of the BODIPY in the head group labeled Gb_3 s is similar to other BODIPY labeled lipids found elsewhere.^[165–172]

To measure the phase distribution of the labeled Gb_3 s, the different phases in the phase-separated GUVs were marked. There are many different phase markers and the best phase markers exist for the l_d phase.^[139,140]

The aim of this work is to quantitatively measure the distribution of Gb₃ in the lipid phases and STxB binding by fluorescence microscopy. Quantitative analysis for the phase preference of the Gb₃s can only be obtained from fluorescence images if no significant fluorescence resonance energy transfer (FRET) between the labeled Gb₃s and the *l_d* marker exists. This ensures that the measured fluorescence intensities fully reassemble the Gb₃ distribution. A FRET effect is detectable in the emission spectrum as an emission of the acceptor fluorophore (*l_d* marker) by excitation of the donor fluorophore (Gb₃s). This is possible if the emission spectrum of the donor fluorophore overlaps with the excitation spectrum of the acceptor fluorophore. To control this, the donor fluorophore was excited and the emission spectrum of the GUVs which contains the two fluorophores was measured.

The two different *l_d* phase marker, TexasRed-DHPE and Dy731-DOPE, were analyzed regarding possible FRET effects with the fatty acid labeled Gb₃s and the BODIPY used for the head group labeled derivatives. The analysis was performed in GUVs composed of DOPC/Gb₃/*l_d* marker (98:1:1). The lipid concentration in the cuvette was 16 μM, determined by the phosphor concentration of the GUV solution. The emission spectra of the six different GUV solutions were measured by means of fluorimeter.

The excitation wavelengths for the emission spectra are 348, 391 and 488 nm for Gb₃PH, Gb₃TT and Gb₃PEG₁₃C_{24:0}H, respectively (figure 4.4). The emission spectra of the three labeled Gb₃s without a *l_d* phase marker were plotted as reference in the diagrams (figure 4.4 green). In blue, the emission spectra of the Gb₃s and TexasRed-DHPE are shown. All three Gb₃s showed a FRET with TexasRed-DHPE at 610 nm. The efficiency of the FRET is higher than 50 % for all labeled Gb₃-species. The FRET effect of the labeled Gb₃s and the second *l_d* marker, Dy731-DOPE, is shown in red in figure 4.4. These emission spectra overlapped nicely with the emission spectra without a *l_d* marker. As the emission of Dy731-DOPE at 760 nm is very low, this part of the emission spectrum is zoomed in (upper right corner figure 4.4). The FRET efficiency was determined as <3 % (figure 4.4 A, B) for the fatty acid labeled Gb₃s and <0.5 % for the head group labeled Gb₃ (figure 4.4 C). These effects are very low and have a minor influence for the determination of quantitative information from fluorescence signal of the Gb₃s.

Other effects which might influence the quantitative evaluation of the fluorescence from Gb₃ are possible quenching effects from salts or even self-quenching of the fluorophores. Quenching reduces the measured intensity of the fluorophores and therefore, it would lead to errors when determining quantitative information from fluorescence images. The self-quenching effect depends on the distance between two fluo-

4. Phase behavior of globotriaosyl ceramide (Gb₃)

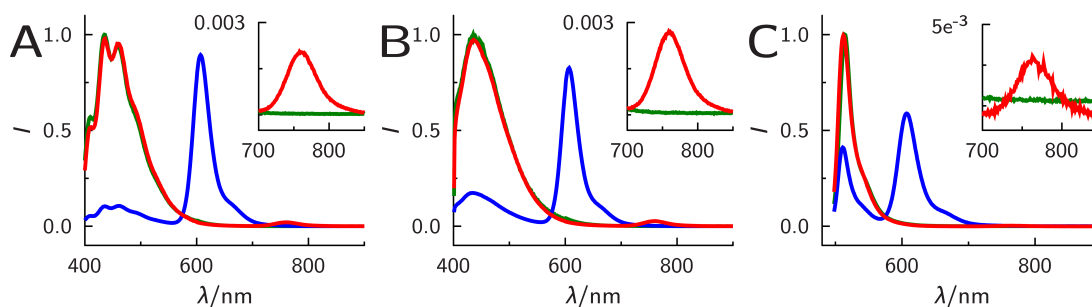


Figure 4.4.: Fluorescence spectra of A) Gb₃PH ($\lambda_{\text{ex}} = 348$ nm), B) Gb₃TT ($\lambda_{\text{ex}} = 391$ nm) and C) Gb₃PEG₁₃C_{24:0}H ($\lambda_{\text{ex}} = 488$ nm). Green lines: fluorescence spectra obtained from GUVs composed of DOPC/Gb₃ (99:1); blue lines: fluorescence spectra obtained from GUVs composed of DOPC/Gb₃/TexasRed-DHPE (98:1:1); red lines: fluorescence spectra obtained from GUVs composed of DOPC/Gb₃/Dy731-DOPE (98:1:1). The lipid concentration in the cuvette was set to 16 μM .

rophore molecules and therefore, it is directly connected to the fluorophore concentration in the lipid mixture. GUVs with varying fluorophore concentration (DOPC/Gb₃ (1-x:x)) were prepared and studied using fluorimetry. The measured excitation intensity of the GUV solution (F) was compared with the emission intensity of the same solution after lysis of the GUVs using Triton X-100 (1 mM, lipid solution, F₀). Lysis leads to a homogeneous distribution of the lipid material in the solution and fluorophore-fluorophore distance is drastically increased.^[173] To make sure that the distance in the lipid solution is large enough, a low lipid concentration of 16 μM in the cuvette was used for the self-quenching experiments (figure 4.5).

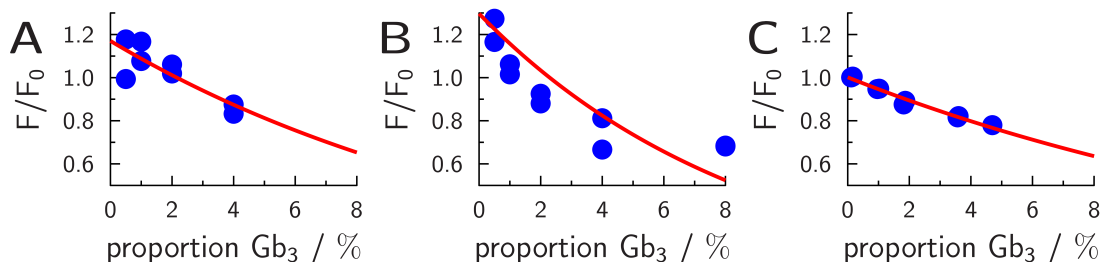


Figure 4.5.: Self-quenching effect of labeled globotriaosyl ceramide (Gb₃). The fluorescence intensity of GUVs (DOPC/Gb₃ (1-x:x)) was recorded before (F) and after Triton X-100 addition (F₀). The excitation wavelengths of the different Gb₃s were 348, 391 and 488 nm for Gb₃PH (A), Gb₃TT (B) and Gb₃PEG₁₃C_{24:0}H (C), respectively. The Gb₃ concentration in the GUVs of Gb₃PEG₁₃C_{24:0}H was measured with adsorptions spectra.

In figure 4.5, the self-quenching effects of Gb₃s labeled with three different fluorophores are shown. The normalized fluorescence intensity (F/F₀) decreases with increasing labeled Gb₃ proportion in the GUVs showing, a self-quenching effect. The

self-quenching effect theoretically shows an exponential course that was adjusted (red line).^[173]

To allow comparison of different experiments, the absolute concentration of Gb₃ in the cuvette is important to be known and is typically measured by absorption measurements (UV/Vis). Because the absorbance of the fatty acid labeled Gb₃s is very weak, the overall signal intensity was too low to allow the determination of Gb₃ concentration in the GUVs by absorption measurements. Instead, the concentrations in the GUVs were approximated by the amount of the fatty acid labeled Gb₃s used for the preparation of the GUVs.

For low Gb₃ concentrations, the relative fluorescence intensity of the fatty acid labeled Gb₃ is above one (figure 4.5 A and B), indicating either a dequenching effect of the fluorophores or a quenching effect of Triton X-100 to the fatty acid labeled Gb₃s. The used concentrations are in a regime where self-quenching does not play a role,^[173] making an interaction between Triton X-100 and fatty acid labeled Gb₃ more probable.

The determination of the concentration of head group labeled Gb₃ in GUVs was performed by UV/Vis. The self-quenching measurement of Gb₃PEG₁₃C_{24:0}H, as an example of the head group labeled Gb₃s, is shown in figure 4.5 C. The relative fluorescence intensity of the BODIPY head group labeled Gb₃ were not above one, proving that no quenching effects of Triton X-100 to the fluorophore exist.

To avoid self-quenching effects of the fluorophore within the measurements head group labeled Gb₃ was used in low amounts of 1 mol % of Gb₃ to ensure no artifacts were present in the calculation of the phase distribution of the Gb₃ species.

Measurements at 1 mol % fatty acid labeled Gb₃ in GUVs were not executable, due to the very low signal-to-noise ratio resulting from the low absorption properties. Therefore, concentration of these Gb₃ species was increased to 5 mol %, allowing to detect phase distributions of the fatty acid labeled Gb₃s. As shown in figure 4.5 A and B, this is a compromise as it represents the lowest possible concentration considering the signal detection, but measurements are influenced by self-quenching effects.

For the quantitative measurements, the measurement parameter for the following phase distribution of Gb₃ studies was chosen: The fatty acid labeled Gb₃s was incorporated in phase-separated GUVs with 5 mol % and the head group labeled Gb₃, with the better signal to noise ratio, with 1 mol %.

4.2.2. Preference of fatty acid labeled Gb₃s in phase-separated GUVs

The phase preference of the two fatty acid labeled Gb₃s (Gb₃PH and Gb₃TT, scheme 3.11) was analyzed in model membrane systems. The Gb₃s were included in GUVs composed of DOPC/SM_{porc}/Chol/Gb₃/Dy731-DOPE (39:35:20:5:1). Images of GUVs were recorded along the Z-axis for both fluorophores, the fatty acid labeled Gb₃ and the *l_d* marker, Dy731-DOPE. From each slide of these Z-stacks, two profile lines were analyzed to calculate the *l_o* phase distribution (%*l_o*) as described in section 3.4.1 (figure 3.2). The results from the different line scans were shown as violin plots for each of the Gb₃-species (figure 4.6).

As shown in figure 4.6, Gb₃PH is nearly homogeneously distributed in the *l_o*/*l_d* phase-separated membrane with a %*l_o* of 0.45. On the other hand, nearly one quarter of the Gb₃TT is present in the *l_o* phase (%*l_o*=0.24, figure 4.6, table 4.2). The distribution width of the two fatty acid labeled Gb₃s differs by a factor of 2. The standard deviation of Gb₃PH is with 0.22 double as high as for Gb₃TT, this can be an artefact of the self-quenching from the fluorophores.

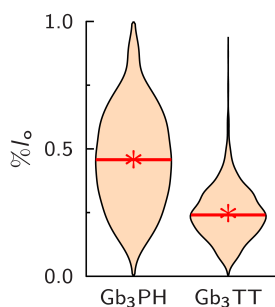


Figure 4.6.: Liquid ordered phase distribution (%*l_o*) of the different fatty acid labeled globotriaosyl ceramides (Gb₃s) in GUVs composed of DOPC/SM_{porc}/Chol/Gb₃/Dy731-DOPE (39:35:20:5:1) visualized as violin plots. The mean values are given as stars and the medians are represented with a stroke. The number of profile lines as well as the mean and the standard deviation are listed in table 4.2.

The fatty acid labeled Gb₃s are preferentially located in the *l_d* phase, in contrast to native Gb₃s which are found in the detergent resistant membranes (DRMs) from primary human blood microvascular endothelial cells (pHBMEC).^[47] A DRM extraction was done by Legros *et al.* to distinguish between the raft domains (DRM fraction, mimic as *l_o* phase) and fluid membrane (non-DRM fraction, mimic as *l_d* phase).^[174–176] It has been shown, that the modification of sphingolipids with bulky fatty acids (as BODIPY or NBD) changes the phase preference of the lipid from *l_o* phase to the *l_d* phase.^[139,142,177,178] The bulky element in the fatty acid is excluded from the *l_o* phase, because it disturbs the membrane order of the *l_o* phase.^[140] Both fatty acid labeled Gb₃s have a bulky structures in the modified chains (scheme 3.11). This might be the reason for the *l_d* phase preference. This explanation is supported by the findings, that the Gb₃TT is more soluble in the *l_d* phase as Gb₃PH (%*l_o*=0.24 ± 0.10

to 0.45 ± 0.22). The fatty acid of Gb₃PH has a phenyl group and a long fatty acid. The fatty acid of Gb₃TT has a thienothienyl ring system which are two rings and a branched chain end which also increases the sterics of the fatty acid.

Table 4.2.: Mean values of the liquid ordered phase distribution ($\%l_o$) for the different fatty acid labeled Gb₃s without (-) and with (+) B-subunit of shiga toxin (STxB) (300 nM). The data are shown as $m \pm sd$ (N); m : mean value, sd : standard deviation, N : numbers of analyzed profile lines.

$\%l_o$ (N)	Gb ₃ PH	Gb ₃ TT
-STxB	0.45 ± 0.22 (2175)	0.24 ± 0.10 (2003)
+STxB	0.41 ± 0.21 (2103)	0.24 ± 0.11 (2329)

Upon binding of STxB, a reorganization within the lipid membrane might be happening and the preferred phase of the Gb₃s might change to the l_o phase because the STxB binds the natural Gb₃ in the l_o phase.^[54,160,162] To study this, GUVs were analyzed in the same way as described before, in presence of 300 nM STxB in the GUV solution. These Gb₃ distributions were compared with GUVs which were not incubated with STxB (figure 4.7, table 4.2). The violin plots of the $\%l_o$ of the Gb₃ without STxB (-STxB) looks similar to the violin plots with STxB for both fatty acid labeled Gb₃s. The distribution of both fatty acid labeled Gb₃s did not change significantly (figure 4.7, table 4.2 and A.4).

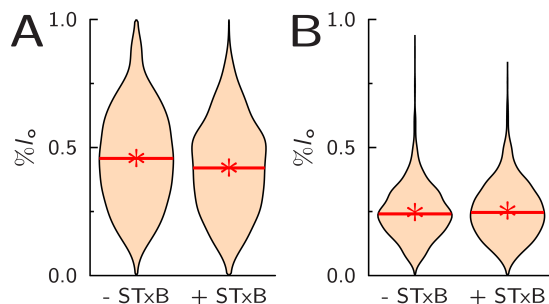


Figure 4.7.: Violin plots of liquid ordered phase distribution ($\%l_o$) from different fatty acid labeled Gb₃s before (-STxB) and after binding of STxB (+STxB, 300 nM). The measurement was done with GUVs composed of DOPC/SM_{porc}/Chol/Gb₃/Dy731-DOPE (39:35:20:5:1). In A, the $\%l_o$ of Gb₃PH and in B, the $\%l_o$ of Gb₃TT are compared to the binding of STxB. The mean values are given as stars and the medians are represented with a stroke. The number of analyzed profile lines as well as the mean and the standard deviation is listed in table 4.2.

The binding of STxB to phase-separated GUVs with fatty acid labeled Gb₃s did not change the phase distribution of the Gb₃s. There are two possible interpretations for this result: First, the STxB did not bind to the Gb₃s and second, the STxB

4. Phase behavior of globotriaosyl ceramide (Gb₃)

binds to the l_d phase and the binding did not shift the phase distribution of the fatty acid labeled Gb₃s. To check the binding of STxB to the l_d phase, the phase-separated GUVs with the fatty acid labeled Gb₃s were incubated with 300 nM Cy3 labeled STxB (figure 4.8). The intensity images and the radial profile of STxB is co-localized with the intensity of Dy731-DOPE (figure 4.8). This observation suggests that the binding of STxB to fatty acid labeled Gb₃ is located in the l_d phase.

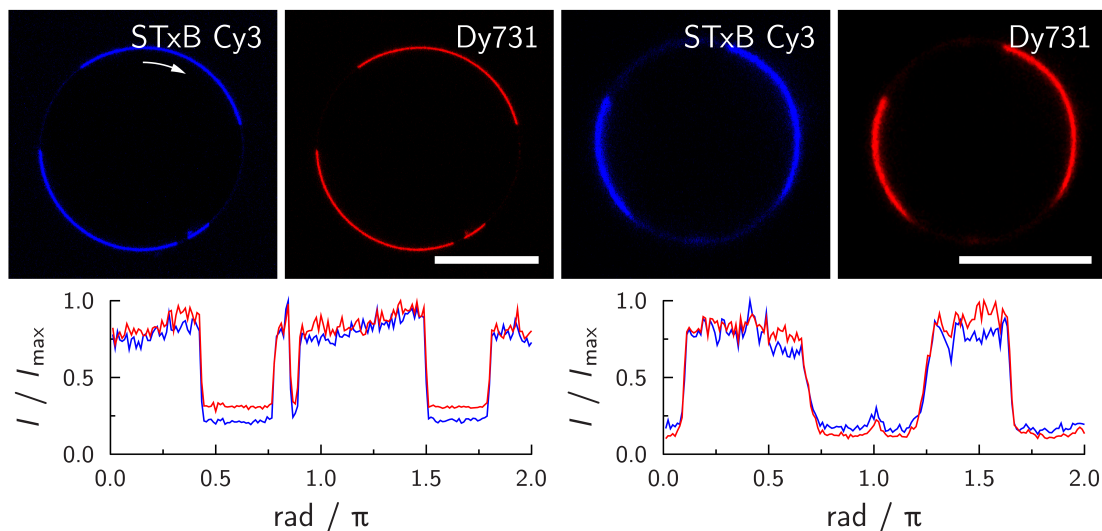


Figure 4.8.: Confocal fluorescence image of phase-separated GUVs composed of DOPC/ SM_{porc} /Chol/Gb₃/Dy731-DOPE (39:35:20:5:1) with 300 nM Cy3 labeled STxB in solution. The fluorescence image from the STxB is shown in blue and from the phase marker Dy731-DOPE is shown in red. Underneath the circular profile of the GUV intensity of both fluorophores is plotted, starting at twelve o'clock and going clockwise. A) represents a GUV with Gb₃PH and B) Gb₃TT. Scale bar 10 μ m.

Using natural^[54,55] and synthetic unlabeled Gb₃s,^[160,162] STxB binds to the l_o phase which is not in agreement with the fatty acid labeled Gb₃s. A similar phenomena was reported in studies with B-subunit of cholera toxin (CTxB) which binds to its fatty acid labeled receptor pentasaccharide ganglioside (GM₁).^[142,177,179,180] While CTxB is known to bind to GM₁ in the l_o phase, the fatty acid labeled GM₁ binding to CTxB was observed in the l_d phase.^[142,181,182] The change in the fatty acid from an alkyl to a bulky ring system changed the packing density of Gb₃. The phase preference of the receptor is the l_d phase and therefore protein binding also takes place in the l_d phase. From this observation, it can be concluded that the phase preference and distribution of the fatty acid labeled Gb₃s does not represent the phase preference and distribution of the natural Gb₃s.

4.2.3. Preference of head group labeled Gb₃ in phase-separated GUVs

The fatty acid labeled Gb₃ derivatives are preferentially distributed in the l_d phase and bind STxB in the l_d phase in contrast to natural Gb₃s which are typically bound by STxB in the l_o phase.^[54,55] To mimic the natural situation head group labeled derivatives were synthesized. The head group of Gb₃ consists of a trisaccharide which is only partially involved in the binding of STxB to Gb₃.^[50,183,184] The 2'-hydroxyl-group of the β -galactose of the Gb₃ head group does not contribute to the process of STxB binding as shown by crystal structure analysis^[50] and binding studies of trisaccharides.^[183,184] To ensure the head group labeled derivatives mimic the situation found in cellular systems in terms of phase preference and STxB binding, the uninvolved hydroxyl group was used to connect the fluorophore BODIPY *via* a PEG linker to the Gb₃ (scheme 3.12). Unlike natural Gb₃ which are a mixture of 16 to 24 carbon atoms in the alkyl chains, the fatty acid of the head group labeled Gb₃s is based on the C₂₄ fatty acid. C₂₄ was chosen, because they are a major part of the Gb₃s in erythrocytes,^[185] HeLa cells^[186] and HEP-2 cells.^[187] In addition, natural Gb₃s show α -hydroxylation. The group of Prof. Dr. Daniel B. Werz synthesized head group labeled Gb₃s with different fatty acids to enable the investigation of the influence of the fatty acid saturation and hydroxylation on the phase distribution. In total, eight different head group labeled Gb₃s, with three chemical modifications were synthesized. To encode the information of the chemical structure of the Gb₃ the following abbreviation is used: Gb₃PEG_nC_{24: Δ} X (scheme 3.12). The linker length of the PEG linker (n) was chosen to be 3 and 13 units. At position 15 of the fatty acid (C_{24: Δ}), a double bond was introduced to check the effect of unsaturated fatty acids (C_{24:1}) compared to saturate fatty acids (C_{24:0}). The α -hydroxylation (x) was set to non-hydroxylized (H) or hydroxylized (OH) fatty acids. Phase preference of the head group labeled Gb₃s was measured according to the methodology and techniques already described for the fatty acid labeled Gb₃s (chapter 3.4.1). GUVs composed of DOPC/SM/Chol/Gb₃/Dy731-DOPE (39:39:20:1:1) were used. An overview of the results from these eight different head group labeled Gb₃s is shown in table 4.3. In the following section, different aspects of the chemical modifications and their influence on the phase preference are discussed in detail.

Linker length

Surprisingly, the size of the linker attached to the head group of a lipid alters the phase behavior of the fluorescently labeled lipid dramatically.^[188,189]

4. Phase behavior of globotriaosyl ceramide (Gb₃)

Table 4.3.: Mean values of the liquid ordered phase distribution (% l_o) for the different head group labeled Gb₃s in GUVs composed of DOPC/SM_{porc}/Chol/Gb₃/Dy731-DOPE (39:39:20:1:1). The errors are the standard deviation of the mean. N in brackets is the number of analyzed profile lines. The number (No.) references the Gb₃-species in table 4.4.

	% l_o (N)	No.
Gb ₃ PEG ₃ C _{24:0} H	0.41 ± 0.07 (2516)	1
Gb ₃ PEG ₃ C _{24:0} OH	0.42 ± 0.08 (2273)	2
Gb ₃ PEG ₃ C _{24:1} H	0.32 ± 0.07 (2351)	3
Gb ₃ PEG ₃ C _{24:1} OH	0.27 ± 0.06 (2701)	4
Gb ₃ PEG ₁₃ C _{24:0} H	0.74 ± 0.07 (2525)	5
Gb ₃ PEG ₁₃ C _{24:0} OH	0.71 ± 0.05 (3064)	6
Gb ₃ PEG ₁₃ C _{24:1} H	0.47 ± 0.15 (1654)	7
Gb ₃ PEG ₁₃ C _{24:1} OH	0.50 ± 0.08 (2377)	8

Gb₃s with saturated non-hydroxylated chains showed a clear l_d phase preference when a PEG₃ linker was present (% l_o =0.41 ± 0.07, table 4.3) and a strong l_o phase preference when PEG₁₃ was used linker (% l_o =0.74 ± 0.07, (figure 4.9 A, table 4.3). The difference of 0.33 ± 0.14 showed a significant change in the phase preference between these derivatives (table 4.4 ΔPEG first row). In the same manner, saturated and hydroxylated fatty acid derivatives (figure 4.9 B) show an increase of 0.29 ± 0.13 in the % l_o if the linker length was changed from 3 to 13 PEG units (table 4.4 ΔPEG second row). The effect of PEG linker to the phase preference is also present if unsaturated fatty acids were used without or with hydroxylation (figure 4.9 C and D, table 4.4 ΔPEG last two rows). In conclusion, there is an average increase in the % l_o of 0.25 from the short to the long PEG linker, independent of further chemical modifications. The influence of the linker length to the phase preference of the head group labeled Gb₃s was also analyzed with a linear mixed-effects model (LMM) to check on statistical significance (chapter A.7.2). The LMM analyzed all eight data-sets of the eight different head group labeled Gb₃s at once. The LMM results in a significant influence of the PEG linker on the phase distribution from the head group labeled Gb₃s. The PEG₁₃ derivatives are preferentially located by the value of 0.27 ± 0.03 in the l_o phase, as their correspondent Gb₃-species with a PEG₃ linker (table A.5).

The head group labeled Gb₃s with the longer linker length are preferentially located in the l_o phase. A similar observation was done by Honigmann *et al.*^[188] They reported on a fluorophore that was connected either directly to the lipid DSPE or connected *via* a PEG-linker with 45 ethylene glycol units to the lipid. The fluorophore was reconstituted into supported lipid membranes composed of DPhPC/DPPC/Chol.

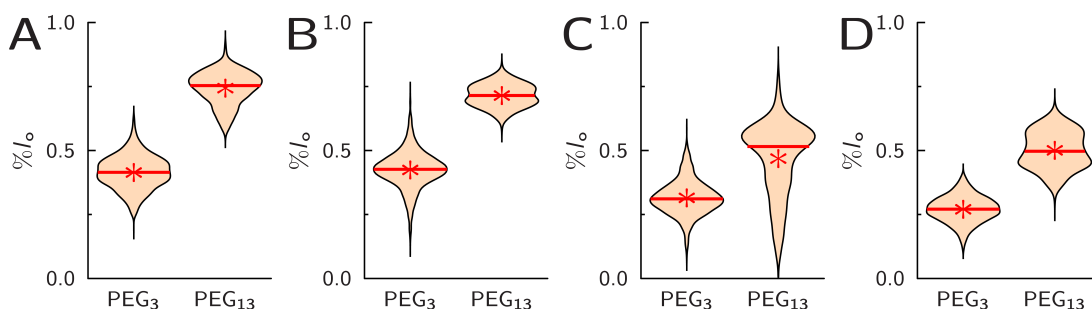


Figure 4.9.: Violin plots of the liquid ordered phase distribution ($\%l_o$) of different head group labeled globotriaosyl ceramide (Gb₃), which compare the different PEG linker length short (PEG₃) to long (PEG₁₃). The residue of the Gb₃ structure is in A Gb₃C_{24:0}H, in B Gb₃C_{24:0}OH, in C Gb₃C_{24:1}H and in D Gb₃C_{24:1}OH. The GUV is composed of DOPC/SM_{porc}/Chol/Gb₃/Dy731-DOPE (39:39:20:1:1). The star represents the mean value. The median is given by the stroke. The mean values with their standard deviation are listed with the number of measurements in table 4.3.

Table 4.4.: Differences in the mean values dependent on the functional group. The numbers are explained in table 4.3 and shorten the Gb₃ species. $\Delta\text{PEG} = \%l_o(\text{PEG}_{13}) - \%l_o(\text{PEG}_3)$; $\Delta\text{C}_{24} = \%l_o(\text{C}_{24:0}) - \%l_o(\text{C}_{24:1})$; $\Delta\text{OH} = \%l_o(\text{H}) - \%l_o(\text{OH})$.

	ΔPEG	ΔC_{24}	ΔOH
5-1	0.33 ± 0.14	5-7 0.27 ± 0.22	5-6 0.03 ± 0.13
6-2	0.29 ± 0.13	6-8 0.21 ± 0.13	7-8 -0.03 ± 0.23
7-3	0.15 ± 0.22	1-3 0.09 ± 0.14	1-2 -0.01 ± 0.15
8-4	0.23 ± 0.14	2-4 0.15 ± 0.14	3-4 0.05 ± 0.13

A fluorescence analysis of the partition clearly showed that the fluorescent lipid lacking the PEG-linker was preferentially localized in the l_d phase, while that with the PEG-linker partitioned into the l_o phase.^[188] The phase preference of fluorescently marked lipids was systematically analyzed by changing the PEG linker length, from 3 to 15 units, between the fluorophore and lipid.^[189,190] The used lipids for labeling are expected to be localized into the l_o phase, of coexisting l_o/l_d phase-separated membranes.^[189,190] It was found that marked lipids are located in the l_d phase, if only 3 PEG units as linker were used, while, in contrast, the use of 15 PEG units as linker changes the phase preference of the labeled lipid to the l_o phase. With PEG linker lengths of 5 and 10, they showed systematically the correlation between the increase of the PEG linker length and an increase of the l_o phase preference from the labeled lipid.^[189,190]

This observation is explained by a model from Klymchenko *et al.*^[140] The fluorophore connected to the lipid is partially hydrophobic and might be also bulky. The fluorophore changes the packing parameter of the lipid, because it increases the head

group size of the labeled lipid. If the distance from the fluorophore to the lipid was increased by a PEG linker, the influence of the fluorophore to the packing density of the lipid can be weaker, up to being not relevant at all.^[140]

In our study, a 13-unit long linker decoupled the fluorophore from the membrane interface with the result that Gb₃PEG₁₃C_{24:0}H which is expected to at least preferentially partition into the l_o phase indeed has a l_o distribution of almost 0.75. From these results, it can be concluded that the Gb₃ species with PEG₁₃ are better suited to report on the natural partition of Gb₃ than those with PEG₃. Thus, the experiments in which the influence of unsaturation and hydroxylation of the fatty acid of Gb₃ is compared are all performed with the PEG₁₃ species. The corresponding results with the PEG₃ linker are plotted for the completeness in figures 4.10, 4.11 and 4.12 and are listed in tables 4.4 and 4.5.

Fatty acid saturation

The influence of fatty acid saturation on the partition behavior of Gb₃ was investigated (figure 4.10). The results show that introducing a fatty acid with a *cis*-double bond redistributes the Gb₃ sphingolipid in the l_d phase which can be rationalized by the increased space requirement of the Gb₃ species with the C_{24:1} fatty acid. The differences between the l_o distribution of Gb₃PEG₁₃C_{24:0}H/Gb₃PEG₁₃C_{24:1}H and Gb₃PEG₁₃C_{24:0}OH/Gb₃PEG₁₃C_{24:1}OH harboring the PEG₁₃ linker are significant and range between 0.21 ± 0.13 to 0.27 ± 0.22 , respectively (table 4.4, ΔC_{24}). The influence of saturation of the fatty acid on the phase preference was also statistically analyzed using the LMM. The analysis was done only for long linker length, these are obviously the better biological mimic model. Gb₃s with saturated fatty acids are highly present in the l_o phase than the Gb₃s with the unsaturated fatty acid (0.24 ± 0.04 , table A.6).

The influence of the fatty acid on the lipid packing of glycosphingolipids with different saturated fatty acid was checked by Stefaniu *et al.* using a Langmuir–Blodgett technique.^[191] The glycosphingolipids with the unsaturated fatty acid have 2% higher molecular area than the glycosphingolipids with the saturated fatty acid. The surprisingly small differences in area per lipid is explained by the strong head group interaction, which suppresses the effect of the unsaturated fatty acid,^[191] as these measurements were performed at a surface pressure of 30 mN m^{-1} which reflects the packing density of lipid bilayers.^[192]

A bilayer study which contains glycosphingolipids with the fatty acids C_{18:0} and C_{18:1} was analyzed with deuterium nuclear magnetic resonance (²H-NMR).^[193] The

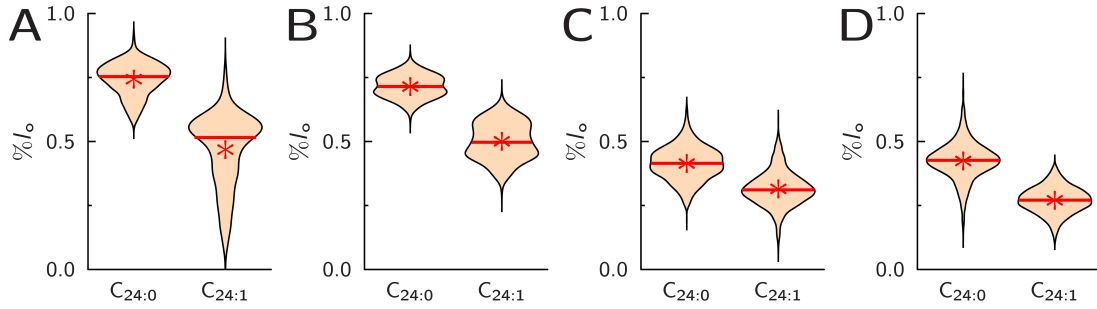


Figure 4.10.: The liquid ordered phase distribution ($\%l_o$) of head group labeled globotriaosyl ceramide (Gb₃). The saturated fatty acid (C_{24:0}) were compared to the unsaturated fatty acid (C_{24:1}) of the Gb₃-species. The Gb₃ residue in A is Gb₃PEG₁₃H, in B Gb₃PEG₁₃OH, in C Gb₃PEG₃H and in D Gb₃PEG₃OH. The GUV composition was DOPC/SM_{porc}/Chol/Gb₃/Dy731-DOPE (39:39:20:1:1). The violin plots include the mean value as star and the median as stroke. The mean values with their standard deviation are listed with the number of measurements in table 4.3.

advantage of the ²H-NMR study is that the ordering parameter is directly measurable and it shows that an unsaturated fatty acid connected to a glycosphingolipid has a less order parameter compared to the saturated fatty acid species. This indicates that unsaturated fatty acids are less incorporated into l_o phases in l_o/l_d membranes, because the l_o phase consists of the ordered lipids.^[194]

Björkqvist *et al.*^[128] analyzed the transition temperature (T_M) of glycosphingolipids in bilayers by differential scanning calorimetry (DSC) measurements and by anisotropy measurements. The structures contain either saturated fatty acid (C_{24:0}) or unsaturated fatty acid (C_{24:1}). In all cases, the saturated system has a ~ 20 K higher T_M compared to the unsaturated one.^[128] The differences in the T_M for the SM C_{24:0} and SM C_{24:1} are also ~ 20 K (table 3.2).^[128,131–133] The reduced T_M indicates lower packing density which results in less incorporation into the l_o phase. The incorporation of SM C_{24:1} into the l_o phase was measured by the property to create a l_o phase in DOPC/SM/Chol membranes.^[195] While SM C_{24:0} showed phase-separated membrane systems using this lipid mixture, the SM C_{24:1} resulted in a homogeneous membrane. This proves directly that the saturated fatty acid prefers the l_o phase in comparison to the unsaturated fatty acid.

The effect of fatty acid saturation was also found by doing lipid extraction studies of pHBMEC.^[46] DRM extraction was done to distinguish between the raft domains (DRM fraction) and fluid membrane (non-DRM fraction).^[174–176] The Gb₃s were extracted from pHBMEC, the Gb₃s with the saturated fatty acids C_{24:0} were enriched in the DRM fraction and the Gb₃s with the unsaturated fatty acids C_{24:1} were enriched in the non-DRM fraction^[46] which is in agreement with the study in this thesis.

α -Hydroxylation

In nature, there is a great amount of α -hydroxylated fatty acids among the Gb₃s.^[185] The influence of the hydroxylation in the fatty acids from the Gb₃s is shown in figure 4.11. No significant differences were found when non-hydroxylated Gb₃s are compared to hydroxylated Gb₃s (table 4.4 Δ OH). The analysis of the LMM to the hydroxylation results in no significant differences between the head-group labeled Gb₃s (0.01 ± 0.03 p-Value=0.67, table A.5).

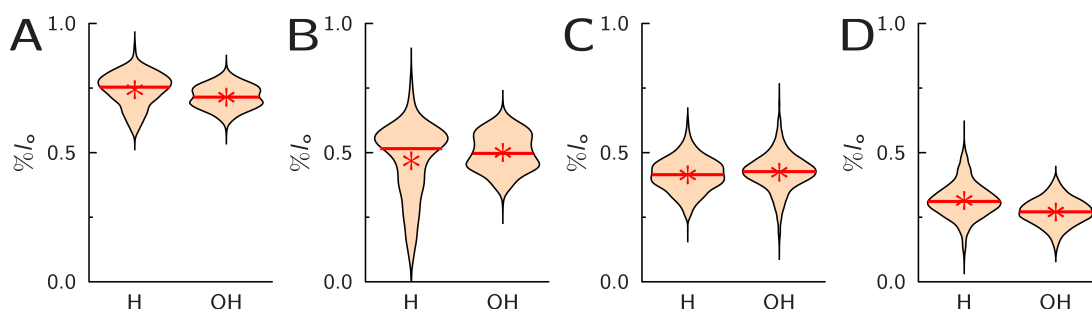


Figure 4.11.: The liquid ordered phase distribution ($\%l_o$) of the different head group labeled Gb₃-species are compared to their hydroxylation in α position at the fatty acid in violin plots. The lipid composition of the GUVs was DOPC/SM_{porc}/Chol/Gb₃/Dy731-DOPE (39:39:20:1:1). The Gb₃ structures Gb₃PEG₁₃C_{24:0} (A), Gb₃PEG₁₃C_{24:1} (B), Gb₃PEG₃C_{24:0} (C) and Gb₃PEG₃C_{24:1} (D) are plotted respectively. The mean values are given by a star and the median values are given as a stroke. The mean values with their standard deviation are listed with the number of measurements in table 4.3.

The influence of α -hydroxylation to the area per lipid was analyzed using galactosylceramide (GalCer)_{C_{24:0}} at an air water interface.^[191] Stefaniu *et al.* found that the α -hydroxylated GalCer-species decrease the area per lipid with higher surface pressure. The influence of the surface pressure on the area per lipid from the hydroxylated species is a result of changing their fatty acid tilt angle depending on the surface pressure. In contrast, the non-hydroxylated GalCer has a constant area per lipid and a constant tilt angle during the change of the surface pressure. At a surface pressure of 30 mN m^{-1} which reflects the packing density of a bilayer,^[192] both lipids have the same area per lipid.^[191] Therefore, no differences in lipid packing behavior are present which explains the finding that hydroxylation has no influence on the phase distribution of the l_o/l_d phase.

Morrow *et al.* measured the difference of the hydroxylation in α position at the fatty acid C_{18:0} from glycosphingolipids in POPC/Chol membranes with the ²H-NMR. They reported that the ordering parameter showed no differences for the α -hydroxylated and non-hydroxylated C₁₈ at the glycosphingolipid.^[193] The orientation of the sugar head group was also the same for both glycosphingolipids.^[196] This is

in line with the observation that the hydroxyl-group did not significantly alter the partition of the Gb₃-species in phase-separated GUVs.

However, even if the partitioning of Gb₃ in the l_o phase is similar for the non-hydroxylated and hydroxylated species, Schütte *et al.* found that the 2-OH group influences the fraction of l_o phase in phase-separated supported lipid bilayers.^[162] In case of the hydroxylated C_{24:0} fatty acid, the l_o fraction is lower compared to the non hydroxylated species.^[162] Ekholm *et al.* showed that the 2-OH group increases the hydration in the membrane interface and decreases the affinity of a sphingolipid for sterols.^[197] The same was found by Lingwood *et al.*^[198] and Yahi *et al.*^[199] and implies that the recruitment of Chol into the l_o phase by hydroxylated Gb₃ is reduced compared to the non-hydroxylated species leading to a smaller l_o fraction.

Influence of the sphingomyelin fatty acid

The studies of the influence from chemical differences on the head group labeled Gb₃s were done with a nature extraction of SM, the SM_{porc}. This SM is a mixture of different SMs, which are listed in table 3.1. The phase behavior of ternary mixtures are influenced by the lipids. The exchange of the sphingomyelin in a ternary lipid mixture from a SM mixture to a defined SM is known to alter the phase separation behavior.^[200] Five different SM species with a saturated fatty acid varying in length were chosen, namely palmitoyl SM (SM C_{16:0}), stearoyl SM (SM C_{18:0}), arachidoyl SM (SM C_{20:0}), behenoyl SM (SM C_{22:0}) and lignoceroyl SM (SM C_{24:0}).

For each of the eight different head group labeled Gb₃-species, a % l_o distribution was measured with each of the five different SMs (figure 4.12, table 4.5). Comparing the four Gb₃-species with the PEG₁₃ linker (figure 4.12 A, B, C, D, table 4.5 first four rows) the % l_o increases with the length of the SMs. From SM C_{16:0} to SM C_{18:0} there is a slide increase in the % l_o with the saturated fatty acid (figure 4.12 A and B) and with the unsaturated fatty acid there is nearly no increase (figure 4.12 C and D). The strongest increase in % l_o is found comparing SM C_{18:0} to SM C_{20:0}. From SM C_{20:0} over SM C_{22:0} to SM C_{24:0} there is only a minor or no increase in % l_o for the Gb₃s with the PEG₁₃ linker. The % l_o data from the head group labeled Gb₃s with PEG₁₃ linker was statistically analyzed with LMM. The influence of the fatty acid length from the SMs to the % l_o of the Gb₃ shows three groups, which significantly differ. The data of the SM C_{20:0}, SM C_{22:0} and SM C_{24:0} showed no differences to each other. They differs significantly to the SM C_{16:0} and SM C_{18:0}. The measured % l_o with the SM C_{16:0} differs from the SM C_{18:0} (table A.8).

4. Phase behavior of globotriaosyl ceramide (Gb_3)

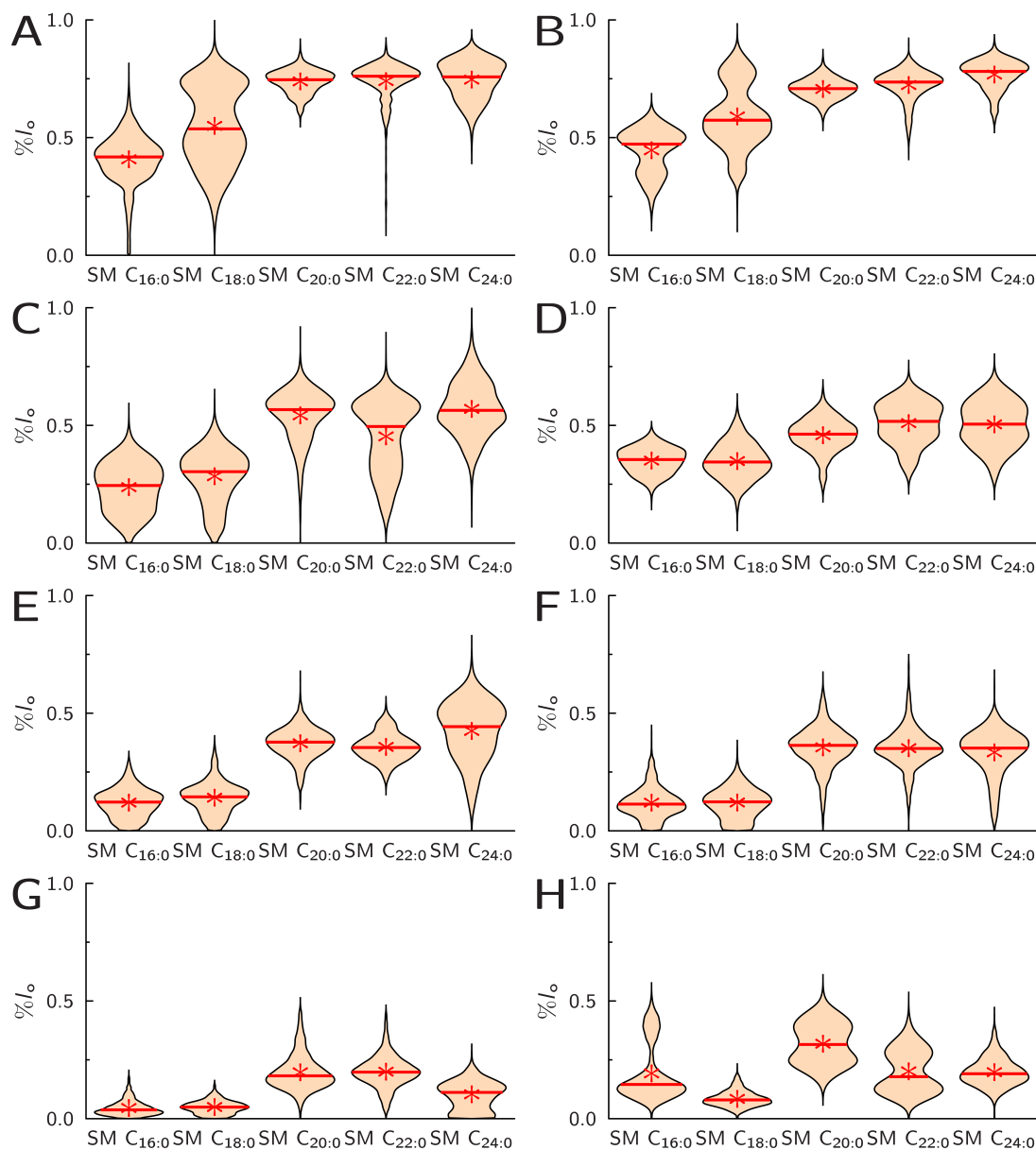


Figure 4.12.: The liquid ordered phase distribution ($\%l_o$) was measured for all eight different head group labeled Gb_3 s $Gb_3PEG_{13}C_{24:0}H$ (A), $Gb_3PEG_{13}C_{24:0}OH$ (B), $Gb_3PEG_{13}C_{24:1}H$ (C), $Gb_3PEG_{13}C_{24:1}OH$ (D), $Gb_3PEG_3C_{24:0}H$ (E), $Gb_3PEG_3C_{24:0}OH$ (F), $Gb_3PEG_3C_{24:1}H$ (G) and $Gb_3PEG_3C_{24:1}OH$ (H) with different sphingomyelins (SMs). The different SMs are palmitoyl sphingomyelin ($SM C_{16:0}$), stearoyl sphingomyelin ($SM C_{18:0}$), arachidoyl sphingomyelin ($SM C_{20:0}$), behenoyl sphingomyelin ($SM C_{22:0}$) and lignoceroyl sphingomyelin ($SM C_{24:0}$) in the GUV lipid composition DOPC/SM/Chol/ Gb_3 /Dy731-DOPE (39:39:20:1:1). The mean values of each distribution are represented in the violin plots by a star and and median by a stroke. The mean values with their standard deviation are listed with the number of measurements in table 4.5.

4.2. Analysis of the phase preference of labeled Gb₃s

Table 4.5.: Mean values of the liquid ordered phase distribution ($\%l_o$) for the different head group labeled Gb₃s with different sphingomyelins (SMs) in GUVs composed of DOPC/SM/Chol/Gb₃/Dy731-DOPE (39:39:20:1:1). The SMs are palmitoyl sphingomyelin (SM C_{16:0}), stearoyl sphingomyelin (SM C_{18:0}), arachidoyl sphingomyelin (SM C_{20:0}), behenoyl sphingomyelin (SM C_{22:0}) and lignoceroyl sphingomyelin (SM C_{24:0}). The errors are presented as standard deviation and the numbers of analyzed profile lines are in brackets.

$\%l_o$ (N)	SM C _{16:0}	SM C _{18:0}	SM C _{20:0}	SM C _{22:0}	SM C _{24:0}
Gb ₃ PEG ₁₃ C _{24:0} H	0.41 ± 0.11 (2392)	0.55 ± 0.17 (2986)	0.74 ± 0.05 (2397)	0.74 ± 0.09 (2077)	0.79 ± 0.09 (1707)
Gb ₃ PEG ₁₃ C _{24:0} OH	0.45 ± 0.10 (3232)	0.59 ± 0.14 (3396)	0.71 ± 0.05 (2414)	0.72 ± 0.07 (2893)	0.77 ± 0.07 (2509)
Gb ₃ PEG ₁₃ C _{24:1} H	0.24 ± 0.10 (2035)	0.28 ± 0.12 (1845)	0.54 ± 0.11 (2482)	0.45 ± 0.15 (2759)	0.57 ± 0.12 (1730)
Gb ₃ PEG ₁₃ C _{24:1} OH	0.35 ± 0.06 (1814)	0.34 ± 0.08 (2465)	0.46 ± 0.08 (2648)	0.51 ± 0.09 (2266)	0.50 ± 0.10 (2491)
Gb ₃ PEG ₃ C _{24:0} H	0.12 ± 0.06 (1890)	0.14 ± 0.07 (1539)	0.37 ± 0.07 (2188)	0.36 ± 0.06 (2363)	0.42 ± 0.13 (1695)
Gb ₃ PEG ₃ C _{24:0} OH	0.12 ± 0.07 (2769)	0.12 ± 0.07 (2549)	0.36 ± 0.09 (2907)	0.36 ± 0.09 (2155)	0.33 ± 0.10 (2431)
Gb ₃ PEG ₃ C _{24:1} H	0.05 ± 0.04 (2384)	0.05 ± 0.03 (2413)	0.20 ± 0.08 (2227)	0.20 ± 0.07 (2259)	0.10 ± 0.06 (2505)
Gb ₃ PEG ₃ C _{24:1} OH	0.19 ± 0.12 (3086)	0.09 ± 0.04 (1768)	0.32 ± 0.09 (1988)	0.20 ± 0.09 (2685)	0.20 ± 0.06 (1828)

The general trend, that the head group labeled Gb₃s are more incorporated in the l_o phase, if the fatty acid length of the SMs increases can be explained by the higher order of the SMs with increasing fatty acid length. The gel-liquid phase T_M increases with the fatty acid length from the SMs (table 3.2).^[201] The higher order of the SMs with increasing the fatty acid length was also measured at the air-water interface.^[131,202]

The strong increase of the $\%l_o$ from SM C_{18:0} to SM C_{20:0} is not described by the higher order of the SMs by increasing the fatty acid length. The increase of the fatty acid length in the SM increases the asymmetric chain lengths.^[125] Bilayers of lipids with such asymmetric chain lengths tend to interdigitate into the other leaflet.^[126] This effect increases with higher asymmetry between the chains.^[124,203] The influence of the fatty acid length from SMs to the interdigitation was measured with X-Ray scattering in the gel-phase.^[137,204] The interdigitation was also observed for pure SMs with the fatty acids C_{20:0}, C_{22:0} and C_{24:0} in liquid crystalline phases.^[205,206] The SMs with the long fatty acids interdigitate also in membranes with different lipid compositions which was shown by computer simulations.^[207] The fatty acid mismatch of the head group labeled Gb₃ species is comparable to the fatty acid mismatch found in SM C_{24:0}.

4. Phase behavior of globotriaosyl ceramide (Gb₃)

This explains why Gb₃s prefers interdigitated membrane areas which are present in membranes with SMs with fatty acids longer than or equal to C_{20:0}.

The incorporation of Gb₃s into the *l*_o phase can also be an effect of the Chol content in the *l*_o phase. It is known that Chol is better soluble in the SMs as in phosphatidylcholine (PC) membranes.^[134,202,208] Chol is best soluble in SM C_{16:0}.^[134,208] If the Chol content in the *l*_o phase would have a greater influence as the SM-species, the %*l*_o from the SM C_{16:0} is expected to be dramatically different from the residual chain lengths. Following the data in table 4.5, this is not the case, so the interaction of Gb₃ to Chol appears to be less important than the interaction of Gb₃ to SM for phase distribution of head group labeled Gb₃s.

Binding of STxB

To check whether head group labeled Gb₃s are representing the natural Gb₃s in terms of phase behavior after STxB binding, Cy3 fluorescently marked STxB was used to perform binding studies. The Gb₃-species with the α -hydroxylated fatty acids were not analyzed, because the phase preference is identical to the phase preference of the Gb₃-species with the non-hydroxylated fatty acids.

GUVs consisting of DOPC/SM_{porc}/Chol/Gb₃/Dy731-DOPE (39:35:20:5:1) were incubated with 500 nM STxB Cy3 and afterwards imaged *via* confocal laser scanning microscope (CLSM). The quantitative analysis of the phase reference of head group labeled Gb₃s was not possible, since for STxB binding, concentrations of Gb₃ in self-quenching amounts was necessary. The images are shown in figure 4.13. Using the fluorescence intensity of STxB Cy3 (blue) and the *l*_d fluorescent marker Dy731-DOPE (red), the localization of the STxB Gb₃ binding was investigated. Underneath each fluorescent image, the circular intensity profile of the GUV is plotted for a better comparison of the intensity information. Figure 4.13 A shows the Gb₃PEG₁₃C_{24:0}H which has the highest preference for the *l*_o phase, before STxB binds. The circular profile shows a decrease in the Dy731-DOPE intensity and at the same position an increase in the STxB Cy3 intensity. This means that both fluorophores are anti correlated and are located in different phases. While Dy731-DOPE marks the *l*_d phase, it is clear visible that the STxB binds into the *l*_o phase.

The change of the fatty acid from the saturated to the unsaturated one of the head group labeled Gb₃ changes the phase preference of the STxB binding. Since, the unsaturated Gb₃ does incorporate into the *l*_o phase (0.47), it is of interest how the distribution changes upon STxB binding. The circular profile line in figure 4.13 B shows a correlation between fluorescence intensities of STxB Cy3 and Dy731-DOPE. This cor-

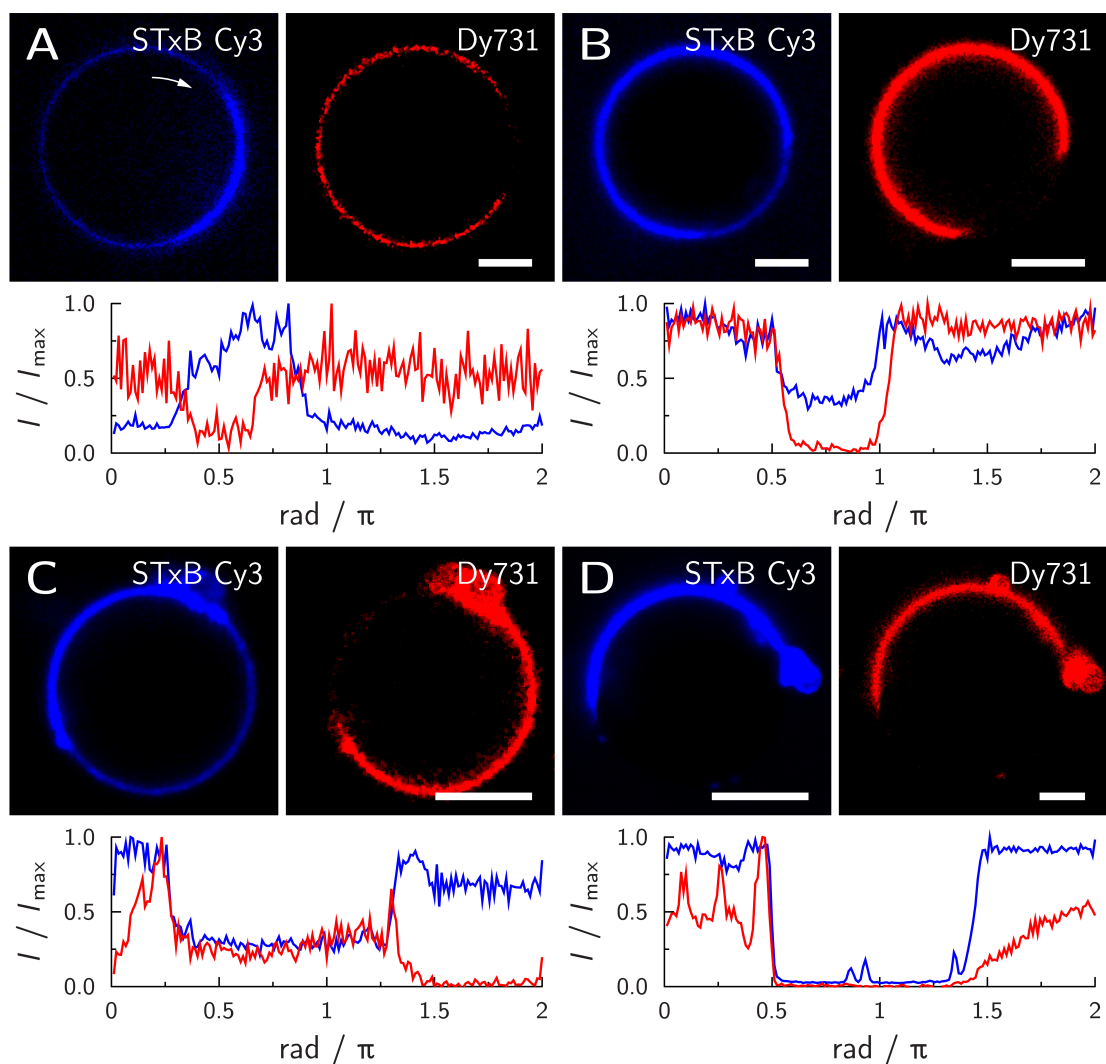


Figure 4.13.: Confocal images of phase-separated GUV composed of DOPC/SM_{porc}/Chol/Gb₃/Dy731-DOPE (39:35:20:5:1) in a 500 nM STxB Cy3 solution. The different head group labeled Gb₃s were Gb₃PEG₁₃C_{24:0}H (A), Gb₃PEG₁₃C_{24:1}H (B), Gb₃PEG₃C_{24:0}H (C) and Gb₃PEG₃C_{24:1}H (D). The labeled STxB is blue-colored and the Dy731-DOPE is shown in red. Under the fluorescent images, the normalized circular profile of the GUV from these two fluorophores are shown starting at twelve o'clock and going clockwise round the GUV, symbolized as a white arrow in A. The scale bars represent 5 μm.

4. Phase behavior of globotriaosyl ceramide (Gb₃)

relation of the two fluorophores indicates that the STxB binding to Gb₃PEG₁₃C_{24:1}H takes place in the l_d phase.

Using unsaturated fatty acid derivatives of Gb₃, the STxB Gb₃ binding occurs a higher amount in the l_d phase (figure 4.13 B and D). While before STxB binding the Gb₃PEG₁₃C_{24:1}H is distributed nearly 1:1 between l_o and l_d phase ($\%l_o = 0.47 \pm 0.15$). The STxB binds the Gb₃ to ~ 0.33 in the l_o phase. This indicated decrease is still in the measured errors. Schütte *et al.* found out that STxB binds Gb₃ with the unsaturated fatty acid C_{24:1} only in the l_o phase,^[162] which is in contrast to our study with the Gb₃PEG₁₃C_{24:1}H.

STxB Gb₃ binding can be altered depending on the saturation state of the alkyl chains of the Gb₃, when a long PEG linker is used. A preference of STxB to the l_o phase was found when saturated fatty acid were used and to the l_d phase when unsaturated fatty acid was used.

The Gb₃PEG₁₃C_{24:0}H is located before the STxB binding in the l_o phase with 0.74 ± 0.07 and the STxB Gb₃ binding is to ~ 0.75 in the l_o phase, indicated by the STxB intensity. This indicates no recruitment of the Gb₃ through STxB which is in line with Schütte *et al.*^[162] They found that the l_o area did not increase on solid supported membranes (SSMs) composed of DOPC/SM_{porc}/Chol/Gb₃ (40:35:20:5), if the STxB binds to the Gb₃ with a C_{24:0} fatty acid.^[162]

To check the possibility that STxB recruits Gb₃ into the l_o phase, STxB Cy3 binding experiments were done with GUVs, containing Gb₃-species with short PEG₃ linker which means that the Gb₃ prefers the l_d phase before STxB binding (figure 4.9). STxB binds the Gb₃PEG₃C_{24:0}H in the l_o phase, as indicated by the anti correlation in the circular profile of figure 4.13 C. The change of the fatty acid from the saturated to the unsaturated of the Gb₃-species with the short PEG linker changes the phase preference of the STxB binding from the l_o to the l_d phase which is shown in the correlation of the two fluorophores in the circular profile in figure 4.13 D. The phase preference of STxB binding to the Gb₃PEG₃C_{24:0}H was found to be ~ 0.7 . This indicates a high recruitment of the Gb₃s into the l_o phase, because the Gb₃PEG₃C_{24:0}H location is only up to 0.41 ± 0.07 in the l_o phase before STxB binding. This recruitment of Gb₃ into the l_o phase was precisely analyzed on pore-spanning membranes (PSMs)^[209] and in HeLa cells.^[145] In HeLa cells, Falguières *et al.* analyzed the amount of Gb₃ in the DRM before and after the STxB binding, which increases.^[145]

4.3. Conclusion of phase behavior of Gb₃

The bacterium enterohemorrhagic *Escherichia coli* (EHEC) is one of the main causes of food borne illness also present in industrial countries. The toxin of this bacteria is shiga toxin (STx) which inhibits the protein biosynthesis of eucaryotic cells. In a first step of approaching the cells, the B-subunit of STx (STxB) binds to the receptor lipid globotriaosyl ceramide (Gb₃). This receptor lipid is in different amounts present in the outer membrane of human cells. The cellular membrane is very heterogeneous and has regions of higher and lower ordering. It is known that binding of STx to the membrane takes place in a more ordered membrane structure. To get a better knowledge about the distribution of the Gb₃ in the membrane before and after STxB binding, phase behavior of fluorescently labeled Gb₃s was analyzed in biomimetic model membranes.

The phase distribution behavior of fluorescently labeled Gb₃ was studied in phase-separated giant unilamellar vesicles (GUVs) composed of DOPC/SM_{porc}/cholesterol (Chol). Two different labeling strategies were used: fatty acid labeled Gb₃ and head group labeled Gb₃. Two different fatty acid labeled Gb₃s were analyzed: Gb₃ phenyl-modified fatty acid (Gb₃PH) and Gb₃ thienothienyl-modified fatty acid (Gb₃TT). Gb₃PH was found to be nearly homogeneous distributed in the liquid ordered (l_o)/liquid disordered (l_d) phase-separated membrane before and after STxB binding. Gb₃TT is only present at a partition of 0.24 in the l_o phase before and after STxB binding. STxB showed preferred binding to the l_d phase. This is in contradiction to the phase distribution of natural Gb₃ STxB binding.^[54] Thus tail labeled Gb₃-species are not suitable representations for the natural Gb₃s.

A second strategy to label Gb₃ is at the head group. The fluorophore BODIPY was connected with a polyethylene glycol (PEG) linker directly to the trisaccharide. This also allowed to vary the fatty acid of the labeled Gb₃s. The major part of the Gb₃s in erythrocytes,^[185] HeLa cells^[186] and HEP-2 cells^[187] have a fatty acid length of 24 carbon atoms which was used in this thesis. The head group label allowed to study the effects of saturation and α -hydroxylation of the chains on the phase distribution behavior before STxB binding.

First, it was found that changing the linker length from 3 to 13 PEG units changes the phase preference from l_d to l_o phase. Since the interaction between the membrane and the fluorophore decreases with increasing linker length, a longer linker is more suitable to represent the natural Gb₃ behavior. Gb₃-species with the unsaturated fatty acid preferred the l_d phase compared to the Gb₃-species with the saturated fatty acid. Hydroxylation had no influence on the phase preference of the Gb₃s.

4. Phase behavior of globotriaosyl ceramide (Gb₃)

Furthermore, the influence of the lipid mixture on the phase preference of Gb₃ was investigated. Five different sphingomyelins (SMs) were chosen to study the phase preference of Gb₃. With increasing SM chain length, solubility of Gb₃ in the *l*_o phase is also increasing.

Concerning STxB binding to Gb₃, STxB binds to head group labeled Gb₃, but a quantitative analysis was not possible, since for STxB binding concentrations of Gb₃ in self quenching amounts were necessary prohibiting a quantitative analysis. The phase preference of STxB binding to head group labeled Gb₃ ranges from the *l*_d phase to the *l*_o phase. Head group labeled Gb₃s are more suitable representations for the natural Gb₃s than fatty acid labeled Gb₃s.

5. Pore-spanning membranes (PSMs)

The cellular membrane is build up with different lipids and proteins and determines the shape of cells. The lipid raft theory says that there are different lipid order in the cellular membrane which are mimicked with the model of liquid ordered (l_o)/liquid disordered (l_d) phase-separated membranes. One important aspect in determining the shape of cells is the strength of the interactions between the membrane and cytoskeleton as well as between membrane and substrate. Examples of these are cell-cell junctions,^[108] glycolipid domain adhesion,^[210,211] neuronal synapses^[212] or the cytoskeleton.^[87,213] These interactions have in common, that the membrane is in an adhesive interaction with other structures and that these interactions strongly influence cellular shape, membrane properties like composition and mechanical stability. To mimic such a heterogeneously adhered membrane, a system with different membrane adhesion properties is required. Pore-spanning membranes (PSMs) are a suitable system to mimic different adhesion states and their influence on lipid membranes. In these models lipid membranes are spanned over nano- to micrometer large cavities, dividing the membrane into free-standing (non adhered) and solid supported (adhered) membrane areas (figure 5.1).

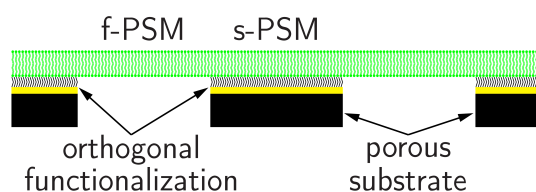


Figure 5.1.: The pore-spanning membrane (PSM) is generated on an orthogonal functionalized porous substrate. PSMs have two different membrane areas with different properties. Freestanding PSMs (f-PSMs) are spanned over the cavities. Solid supported PSMs (s-PSMs) are adhered to the functionalized surface.

With the PSMs, properties of membranes like membrane tension and lipid diffusion as well as their interplay can be studied to gain insights into their importance and effects in cellular systems.

The membrane tension strongly depends on the surface functionalization of the substrates.^[214] Therefore, different functionalization strategies were performed and

the membrane tension was measured by means of atomic force microscopy (AFM) indentation experiments.^[155] These tensions were compared with the membrane tension of cells which ranges from 0.01 to 0.15 mN m⁻¹.^[215,216]

In most common functionalization strategies a gold layer close to the membrane is included. The fluorescence emission is quenched on the s-PSM.^[217–219] In this thesis, different functionalization strategies were studied regarding their fluorescence information. The silicon oxide (SiO_x) functionalization allows to analyze l_o/l_d phase-separated membranes not only in the f-PSM, but also in the s-PSM. The influence of the two adhesion regimes were analyzed to the phase transition of the different lipid phases depending on the cholesterol (Chol) content.

Moreover, diffusion is an important aspect of different lipid species in the cell membrane. The diffusion constant of different lipids was measured in the PSM with interferometric scattering microscopy (iSCAT) or fluorescence correlation spectroscopy (FCS).

5.1. Different functionalization strategies and their effects on pore-spanning membranes (PSMs)

Various functionalization strategies were used to generate the PSMs. The functionalizations were mercaptoalcohols on gold, plasma cleaned silicon nitride (p-Si₃N₄) or SiO_x. The SiO_x functionalization was published in: Teske N., **Sibold J.**, Schumacher J., Teiwes N. K., Gleisner M., Mey I. & Steinem C. Continuous Pore-Spanning Lipid Bilayers On Silicon Oxide-Coated Porous Substrates. *Langmuir* **33**, 14175–14183 (2017). The measurements of the lipid diffusion by iSCAT and of membrane tensions in f-PSMs on 6-mercapto-1-hexanol on gold (6MH-Au) and p-Si₃N₄ functionalized substrates were published in: Spindler S., **Sibold J.**, Gholami Mahmoodabadi R., Steinem C. & Sandoghdar V. High-Speed Microscopy of Diffusion in Pore-Spanning Lipid Membranes. *Nano Lett.* **18**, 5262–5271 (2018).

Crucial for all functionalization methods is that the functionalization is only on the top of the porous substrates which were achieved with a orthogonal evaporation process. The orthogonal evaporation generated a cut off of functionalization at the pore border which is essential, because the membrane sheet, prepared by rupturing giant unilamellar vesicles (GUVs), can suspend over the pores. In contrast, if the cylindrical pore walls were also functionalized, the membrane typically adheres to the cylindrical pore walls and ruptures, instead of creating PSMs. Depending on the functionalization, different materials were used for the evaporation. An orthogonal

gold layer was evaporated on the substrates for the mercaptoalcohols on gold and the p-Si₃N₄ functionalization (chapter 3.2.2). Silicon monooxide (SiO) was orthogonally evaporated on the substrates to generate the SiO_x functionalization (chapter 3.2.2).

The orthogonality of the evaporation for the two different evaporation processes was proven using scanning electron microscopy (SEM). The evaporated gold or SiO on top of the substrates was homogeneous (figure 5.2 A and C). A cross section of the orthogonal evaporated substrate shows the gold as well as the SiO_x layer exclusively on top of the substrate (figure 5.2 B and D). Small gold or SiO_x deposits become discernible also at the inner parts of the cylindrical pore walls. A homogeneous and continuous surface coverage with only small deposits of the material inside the pores is required to induce GUV spreading to form PSMs.^[214]

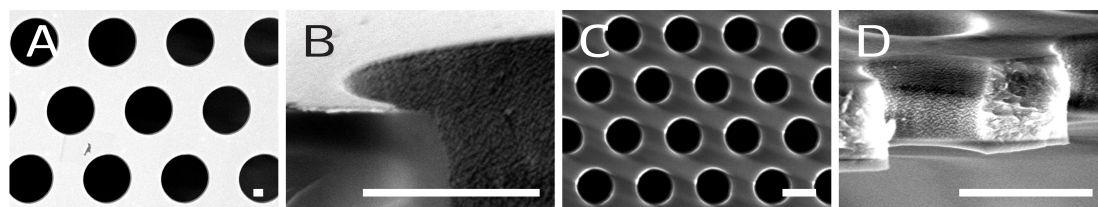


Figure 5.2.: The orthogonal evaporation of gold on porous substrates is shown in A and B. In C and D the evaporation of SiO is shown. A and C are top views which shows the homogeneity of both evaporation processes. B and D are cross sections which shows small clusters of the evaporation material in the pores. Scale bars 1 μm .

The gold and SiO evaporation processes resulted in a homogeneously covered layer on top of the substrates. Just small deposits were observed at the inner pore walls, indicating a successful functionalization to generate PSMs on the porous substrates.

5.1.1. Visualization of pore-spanning membranes (PSMs)

The silicon oxide surface was directly used to generate PSMs by spreading GUVs. The plasma cleaned silicon nitride surface was used to generate PSMs by spreading GUVs, after the cylindrical pore walls was passivated with polyethylene glycol (PEG). After successful physisorption of gold on the surface, chemisorption of thiols like mercaptoalcohols was necessary to establish a surface vesicles can spread on.

A schematic illustration of the three different functionalization is shown in figure 5.3 (top row). All three surface functionalizations resulted in a hydrophilic surface which is covered with hydroxyl-groups. In detail, the surface of 6MH-Au is full of hydroxyl-groups from the 6MH. The functionalization p-Si₃N₄ and SiO_x resulted in a surface with silicon hydroxyl-groups.^[148,220,221]

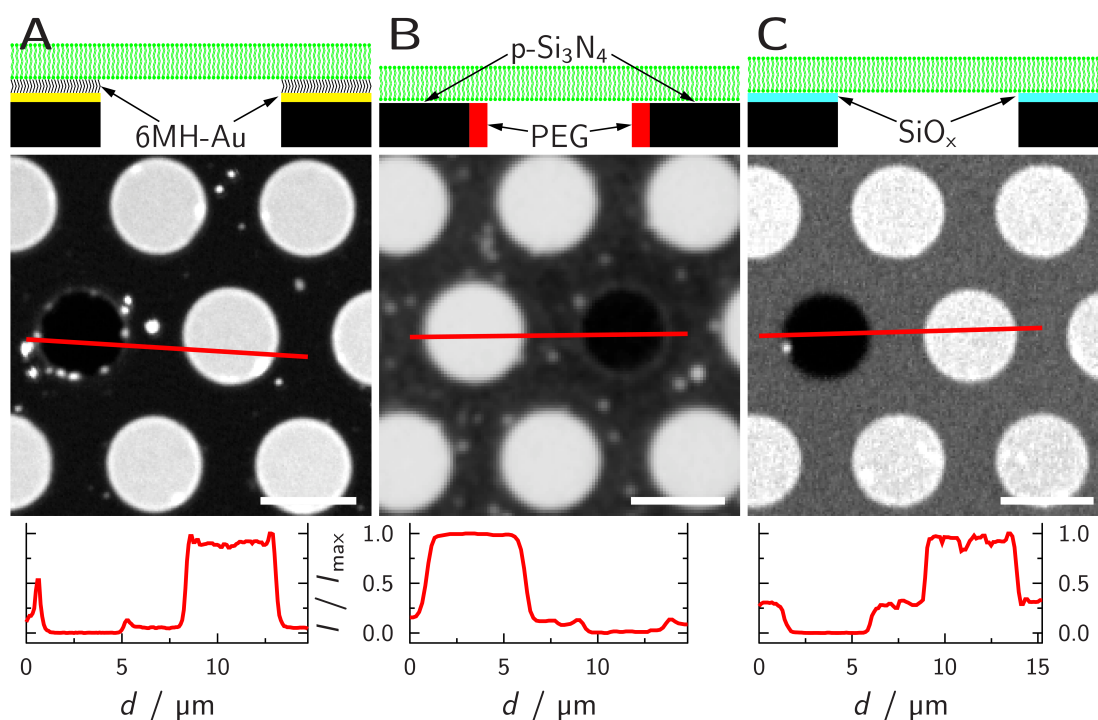


Figure 5.3.: Pore-spanning membranes (PSMs) on three different functionalizations A) 6MH-Au, B) $p\text{-Si}_3\text{N}_4$ and C) SiO_x . In the top row, schematic cross sections of the different functionalizations are shown. In the middle, fluorescence micrographs of PSMs composed of DOPC doped with ATTO488-DOPE on the different functionalizations are shown. From each fluorescent micrograph a profile line was taken at the red line and the intensity profile is plotted underneath. Scale bar 5 μm .

PSMs were generated by spreading of ATTO488-DOPE doped DOPC GUVs on the different functionalizations (figure 5.3 middle row). As expected, the different surface functionalizations influence the fluorescent information on s-PSM. While the f-PSMs are visible on the 6MH-Au functionalization as bright round spots only minor to no fluorescence information on the rims can be gathered (figure 5.3 A). Bright spots on the s-PSM were attributed to adhered, non-spread vesicles. The fluorescence intensity difference between a non-membrane spanned pore, representing the background fluorescence, s-PSM and f-PSM is shown in the cross section. The fluorescence intensity of the s-PSM is only 5% of the intensity measured on the f-PSM. This proves that no information on the s-PSM can be obtained with this system. Quenching of the fluorescence in the s-PSM is happening due to the short distance between membrane and gold surface.^[217–219,222,223] Even if the 6MH builds a layer in between, this layer is only ~ 1 nm thick^[224] and the fluorophores are still in the quenching distance.

A fluorescent micrograph of a PSM with the $p\text{-Si}_3\text{N}_4$ functionalization is shown in figure 5.3 B. Again the f-PSM is detectable as bright round areas with 5 μm in

diameter. In contrast to the 6MH-Au functionalization, the intensity of the s-PSM compared to the f-PSM intensity reaches nearly 15 %, as visualized by the intensity in the cross section (figure 5.3 B). Comparable to the 6MH-Au functionalization, adhered vesicles are visible as bright spots on the membrane.

The last analyzed functionalization strategy to the visualization of the PSM is the SiO_x functionalization. A membrane patch was measured, as shown in figure 5.3 C. As described for the functionalizations 6MH-Au and p-Si₃N₄, the f-PSM is detected as round areas of high fluorescence intensity. The s-PSM reaches a fluorescence intensity of 30 % compared to the f-PSM, showing that this functionalization offers the best possibilities to gather fluorescence information on the s-PSM. A silicon dioxide surface has ideally no quenching,^[217] but dependent on the evaporation techniques, full oxidation of the SiO_x surface was not possible.^[225] SiO_x as a semiconductor still has distance dependent quenching properties,^[226–228] but the highest amount of visible fluorescence on the pore rims compared to the other analyzed functionalizations.

SiO_x functionalized surfaces were used to study the phase separation on PSMs, especially on s-PSM (figure 5.4 and 5.5). Phase-separated GUVs composed of DOPC/SM_{porc}/Chol/porcine erythrocytes globotriaosyl ceramide (Gb_{3porc})/BODIPY-Chol/TexasRed-DHPE (39.5:35:19.5:5:0.5:0.5) were spread at room temperature to generate phase-separated PSMs (chapter 3.2.3). In figure 5.4 A and C the fluorescence intensity of BODIPY-Chol, which is a marker for the l_o phase,^[142,229] is shown as green color while in red the l_d phase is visualized by TexasRed-DHPE (figure 5.4 B and C).^[139,140] An intensity profile line of the corrected and normalized fluorescence intensities (I/I_{\max}) is extracted which includes different f-PSMs (figure 5.4, white). Some f-PSMs are completely composed of l_o phase (green, 0–11 μm), some completely of l_d phase (red, 14.5–16 μm) and some consists of a small l_o phase surrounded by the l_d phase (11–14.5 μm , figure 5.4). The line scans (yellow lines in figure 5.4) derived from the s-PSMs show an area mainly enriched by l_o phase in BODIPY-Chol, simultaneously excluding the l_d phase marker TexasRed-DHPE leading to $I/I_{\max}=0$ at $d=2\text{--}6\ \mu\text{m}$. The l_o phase in the s-PSM is indicated within the white surrounded region in the fluorescence micrographs.

The merged fluorescence image (figure 5.4 C) and profile lines from the two fluorescence intensities BODIPY-Chol (green) and TexasRed-DHPE (red) prove the complete phase separation of l_o and l_d phases in PSMs (figure 5.4 C). When BODIPY-Chol gives a high signal in either image or profile line, no signal from TexasRed-DHPE is detectable and vice versa.

Comparable phase-separated f-PSMs were also described by Schütte *et al.*^[230] They used the 6MH-Au functionalization and were only able to detect the different phase

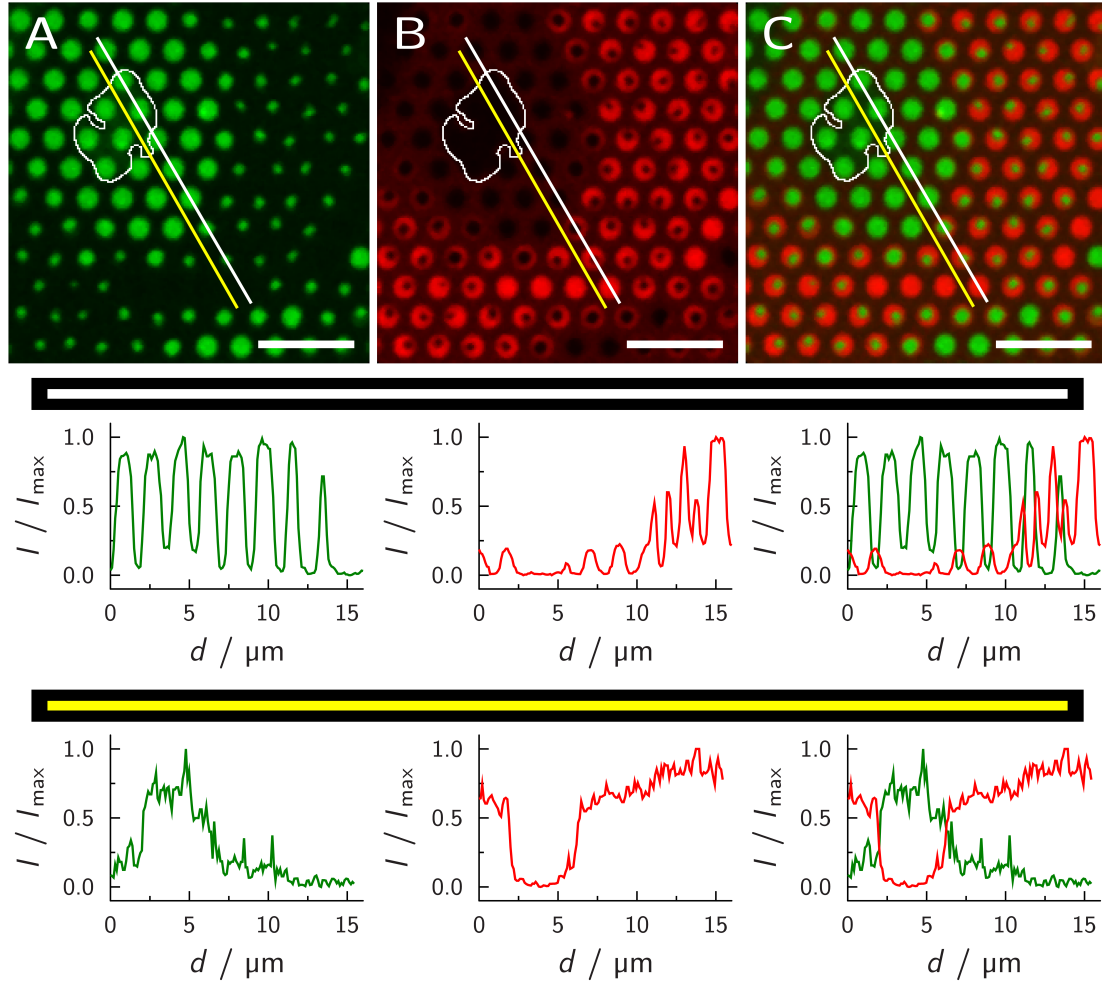


Figure 5.4.: Fluorescent images of phase-separated pore-spanning membrane (PSM) composed of DOPC/ SM_{porc} /Chol/ $\text{Gb}_{3\text{porc}}$ /BODIPY-Chol/TexasRed-DHPE (39.5:35:19.5:5:0.5:0.5). Fluorescence of BODIPY-Chol, labeling the liquid ordered (l_o) phase is shown in green (A, C) and the fluorescence of TexasRed-DHPE, labeling the liquid disordered (l_d) phase is shown in red (B, C). In C, a merged fluorescent image is shown to better visualize the fluorescence intensity differences of both channels. The corresponding yellow lines show the fluorescence intensity profiles of the solid supported pore-spanning membranes (s-PSMs) for the green and red channels, and the white line shows the fluorescence intensity profiles of the freestanding pore-spanning membranes (f-PSMs) for the green and red channels. The white area in the fluorescence images highlights the l_o phase in the s-PSM. Scale bar $5 \mu\text{m}$.

separations in the f-PSM which are: f-PSM was full in l_d phase or l_o phase as well as phase-separated f-PSM. The use of SiO_x extended the information to the description of phase separation in the s-PSM. Phase separation in PSMs was also measured by Sumitomo *et al.*^[231] They visualized only phase separation in the s-PSM and the f-PSM in the l_d phase.

To investigate the possibilities to detect protein binding to PSMs, GUVs composed of DOPC/ SM_{porc} /Chol/ $\text{Gb}_{3\text{porc}}$ /ATTO488-DPPE (39.9:35:20:5:0.1) were spread, generating PSMs on the SiO_x functionalized porous substrates. The PSMs were incubated with 300 nm Cy3 labeled B-subunit of shiga toxin (STxB), which is expected to bind Gb_3 . An exemplary image of these PSMs and the bound proteins is shown in figure 5.5. The fluorescence intensity of the l_d phase marker, ATTO488-DPPE,^[140] is shown in green (figure 5.5 A and C). Interestingly, fluorescence intensity from the l_d phase marker in the f-PSM is only visible near to the border of the f-PSMs. This is analyzed in more detail using intensity profile lines taken from different f-PSMs (figure 5.5 white line). In these profile lines, the intensity is highest at the border of the f-PSM and decreases in the middle of the f-PSM as well as on the s-PSM. While a reduction of fluorescence intensity from f-PSM to s-PSM is expected on the SiO_x quenching effect described earlier, the decrease within the f-PSM seems to gather the l_d phase on the outer borders of the f-PSM while the middle of the pores comprises of l_o phase. l_d phase fluorescence intensity on the s-PSM is very heterogeneous which is shown in the profile line (figure 5.5 yellow line), small areas of low intensity give a strong hint to the existence of l_o phase domains on the s-PSM.

The fluorescence intensity of Cy3 labeled STxB is shown in red (figure 5.5 B and C). The bright round areas in the fluorescence micrograph shows that the STxB binds in the f-PSM (figure 5.5 B and C). This is also seen in the white profile line (figure 5.5 B and C). The merged image of the two channels (figure 5.5 C) shows one spot without any intensity of both channels, this is a non-membrane spanned pore and also detectable in the range from 3.9 to 4.8 μm in the f-PSM profile line (figure 5.5 C, white). Protein intensity is not co-localized with the l_d phase in the s-PSM, which is shown in the profile line (figure 5.5 C, yellow) where the fluorescence of the l_d phase marker decreases from 0.8 to 1.3 μm and from 2.8 to 3.2 μm and the STxB fluorescence was detectable.

The analysis of STxB Cy3 on phase-separated PSMs showed that the STxB Gb_3 binding takes place to the l_o phase in the f-PSM and s-PSM. This was also observed in GUVs^[54] and on solid supported membranes (SSMs).^[162] The l_o/l_d phase separation with no incubation of STxB shows large areas of l_d phases in the s-PSM (figure 5.4). The incubation of STxB on such a system changes the morphology of the l_d phase

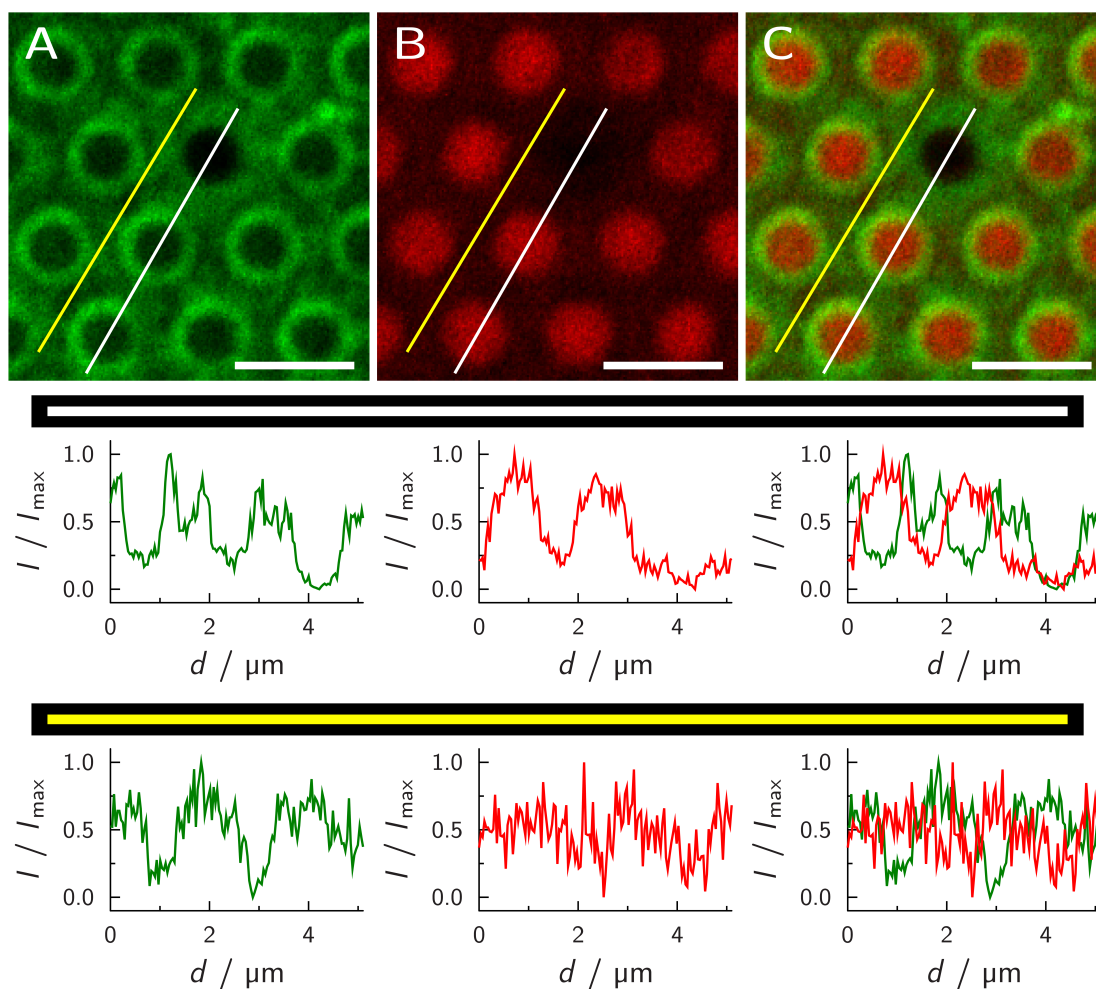


Figure 5.5.: Fluorescence images of phase-separated pore-spanning membrane (PSM) composed of DOPC/ SM_{porc} /Chol/ Gb_{3porc} /ATTO488-DPPE (39.9:35:20:5:0.1) incubated with Cy3 labeled STxB (300 nM, 1 h). Fluorescence of ATTO488-DPPE, labeling the liquid disordered (l_d) phase is shown in green (A, C) and the fluorescence of Cy3 STxB is shown in red (B, C). Corresponding intensity profiles along the yellow line (solid supported pore-spanning membrane (s-PSM)) and along the white line (freestanding pore-spanning membrane (f-PSM)) are plotted below. Scale bar 2 μ m.

on the s-PSM. The l_d phase on the s-PSM was separated by small l_o domains. This can be a hint that the STxB recruits the Gb₃ into the l_o phase.^[55,162]

In this section three different functionalization strategies were analyzed. The possibility to generate PSMs and to detect s-PSM were investigated. The detection of membrane fluorophores in s-PSM is not possible with the 6MH-Au functionalization, because gold quenches the fluorophore. The fluorescence intensity of s-PSM on p-Si₃N₄ functionalized substrates is high enough to distinguish between s-PSM and background. The SiO_x has the best signal-to-noise ratio of s-PSM fluorescence intensity. This enabled to detect phase-separated PSMs. The phase separation was not only visible in the f-PSM, but also in the s-PSM. As described in literature STx is expected to bind exclusively to the l_o phase^[162] which was also found for the model of PSMs. STx binds to the s-PSMs as well as the f-PSMs in co-localization with the l_o phase in both regions.

5.1.2. Membrane tension modulation of pore-spanning membranes (PSMs)

Besides fluorescence intensity, PSMs membrane tension on different surface functionalization was analyzed. Tension was measured by AFM indentation experiments for all mentioned surface functionalizations. The generation of different functionalizations and the generation of PSMs were described in chapter 3.2.2 and 3.2.3. Using correlative fluorescence microscopy, membrane patches were imaged and afterwards investigated by AFM. A topography image of a patch was done in quantitative imaging (QI) mode. In the center of the f-PSM, force-distance curves were measured. Following chapter 3.3.3, the tension of the membranes was derived.

According to Kuhlmann *et al.*, membrane tension of the f-PSM is mainly determined by adhesion of the s-PSM. Lower adhesion is expected to lead to lower membrane tension.^[214] Different functionalizations were investigated to check for the influence of chain length of chemisorbed mercaptoalcohols, plasma cleaned Si₃N₄ and SiO evaporation to the surface hydrophobicity.

To evaluate the influence of chemisorbed thiols, especially the chain length difference of the mercaptoalcohols, GUVs composed of DOPC doped with ATTO488-DPPE were spread on several functionalizations. The functionalizations are chemisorbed 2-mercapto-1-ethanol (2ME), 6MH, 8-mercapto-1-octanol (8MO), 11-mercapto-1-undecanol (11MUD) and 16-mercapto-1-hexadecanol (16MHD) on gold. The length of the thiols is assumed to influence the packing density on the surface and therefore directly influences the hydrophilicity which could result in a higher adhesion. The

5. Pore-spanning membranes (PSMs)

results of the membrane tension measurements with the different mercaptoalcohols gold functionalizations are shown in figure 5.6 and table 5.1. As seen in figure 5.6, there is no direct correlation of length and tension, but different functionalization agents can influence the tension up to a factor of nearly 4. From substrate functionalization 2ME on gold (2ME-Au) ($1.6 \pm 1.1 \text{ mN m}^{-1}$) to 6MH-Au ($0.6 \pm 0.4 \text{ mN m}^{-1}$) membrane tension decreases but increases drastically using 8MO on gold (8MO-Au) ($3.2 \pm 0.9 \text{ mN m}^{-1}$). Over 11MUD on gold (11MUD-Au) ($2.1 \pm 1.4 \text{ mN m}^{-1}$) to 16MHD on gold (16MHD-Au) ($1.0 \pm 0.4 \text{ mN m}^{-1}$) the tension is again decreased. The increase of membrane tension from 6MH-Au to 8MO-Au substrate functionalization interrupts the systematical decrease of membrane tension to the length of the mercaptoalcohols and the membrane tension has no dependency on the chain length from the mercaptoalcohols. The analysis of different membrane tensions was also done with a linear mixed-effects model (LMM), and the differences of membrane tension are not significant (table A.9).

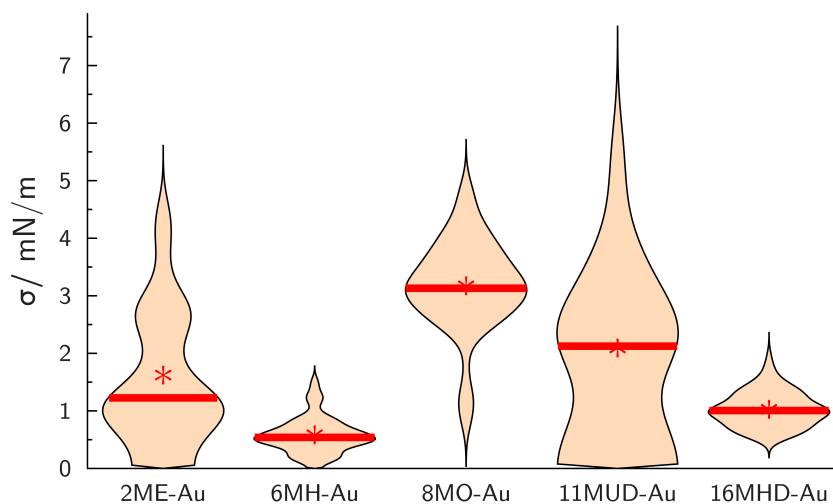


Figure 5.6.: The membrane tension (σ) measured on gold mercaptoalcohol functionalizations. The lipid composition was DOPC/ATTO488-DPPE (99.5:0.5). The surface functionalizations were 2-mercapto-1-ethanol on gold (2ME-Au), 6-mercapto-1-hexanol on gold (6MH-Au), 8-mercapto-1-octanol on gold (8MO-Au), 11-mercapto-1-undecanol on gold (11MUD-Au) and 16-mercapto-1-hexadecanol on gold (16MHD-Au). The stroke indicates the median value in the violin plot and the cross the mean value.

If the chain length has no systematic influence on membrane tension, it seems that the surface density of the mercaptoalcohols is not chain length-dependent. The conformation of chemisorbed 2ME depends on thiol concentration.^[232] A high solution concentration results in more trans conformations of the Au-S-C-C chains which has a higher packing density.^[232] Kudelski described that at concentrations higher than 1 mM, the ratio of the conformations at the surface did not change which means

Table 5.1.: The membrane tension (σ) of the f-PSM composed of DOPC/ATTO488-DPPE (99.5:0.5) was measured on different functionalizations. The lipid composition of the l_o phase on SiO_x functionalized substrate was $\text{SM}_{\text{porc}}/\text{Chol}/\text{ATTO655-DOPE}$ (59.5:39.5:1). The mean value and the standard derivation as the numbers of measurements (N) were listed. The analyze method is described in chapter 3.3.3.

functionalization	σ [mN m^{-1}]	N
2ME-Au	1.6 ± 1.1	251
6MH-Au	0.6 ± 0.4	65
8MO-Au	3.2 ± 0.9	98
11MUD-Au	2.1 ± 1.4	79
16MHD-Au	1.0 ± 0.4	353
p- Si_3N_4	1.6 ± 0.5	77
SiO_x	10.5 ± 4.3	310
SiO_x l_o	6.7 ± 4.0	59

that the surface is packed to a maximum.^[232] In this thesis, the preparation of gold thiol functionalizations was done with a thiol concentration of 1 mM. A high density packing was also found in electrochemical studies. Liu *et al.* analyzed the chemical conductance of gold to ferrocene by increasing the distance of the two materials. The distance was increased using chemisorped mercaptoalcohols with varying chain lengths from 6MH over 8MO and 11MUD to 12-mercapto-1-dodecanol (12MDD).^[233] The electron transfer rate decreased with the elongation of the distance which proves that the mercaptoalcohol density on the gold surface is not dependent on the alkyl length of the mercaptoalcohol. Following this argument, the lateral tension should be the same for all mercaptoalcohols, since all are hydroxy-terminated which should result in equal surface properties. The deviations of the measurements are greater than the differences. It is not possible to find a reason for the differences of the membrane tension with the different mercaptoalcohol gold functionalizations. The high distribution can be an artefact of surface roughness or mobility of the functional groups.

Membrane tensions of different thiol gold functionalized substrates were measured and reported (summarized in table A.2). The membrane tension of DOPC membranes on 2ME-Au functionalization was measured of $1.018 \pm 0.014 \text{ mN m}^{-1}$ ^[234] which is in good agreement with the values found in this work on 2ME-Au with a DOPC bilayer of $1.6 \pm 1.1 \text{ mN m}^{-1}$. The membrane tension with 6MH-Au functionalization was measured by Kuhlmann *et al.* with a membrane composed of DPhPC ($1.4 \pm 0.1 \text{ mN m}^{-1}$).^[214] The range of the measured membrane tension from DOPC includes also the membrane tension value of DPhPC.

5. Pore-spanning membranes (PSMs)

Furthermore, membrane tension of PSMs prepared on p-Si₃N₄ and SiO_x surfaces was determined. Measured membrane tensions from these functionalizations are listed in table 5.1 and are illustrated as violin plots in figure 5.7. The membrane tension of the f-PSM on the p-Si₃N₄ functionalized substrates ($1.6 \pm 0.5 \text{ mN m}^{-1}$) was in the same range as that with 2ME-Au functionalization ($1.6 \pm 1.1 \text{ mN m}^{-1}$). The membrane tension with SiO_x functionalization is more than three times higher than the highest and 18 times higher than the lowest tension found on chemisorbed thiol functionalized substrates.

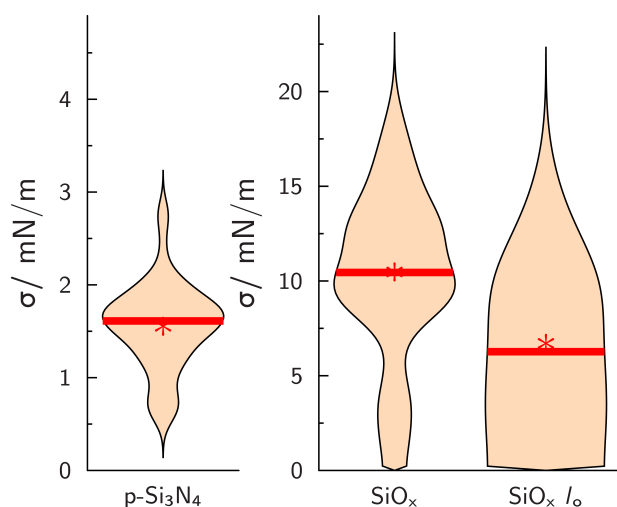


Figure 5.7.: The membrane tension (σ) measured on gold mercaptoalcohol functionalizations. The lipid composition was DOPC/membrane marker (99.5:0.5) and for the l_0 phase measurement SM_{porc}/Chol/membrane marker (59.5:39.5:1). The surface functionalizations were plasma cleaned silicon nitride (p-Si₃N₄) and silicon oxide (SiO_x). The stroke indicates the median value in the violin plot and the cross the mean value.

Mey *et al.* used a porous glass and measured the membrane tension of it.^[235] The membrane tension was $0.15 \pm 0.05 \text{ mN m}^{-1}$ with a DPhPC membrane.^[235] This value is 70 times smaller than the membrane tension with the SiO_x functionalization and the membrane lipid DOPC ($10.5 \pm 4.3 \text{ mN m}^{-1}$) and it is 10 times smaller than the membrane tension with the p-Si₃N₄ functionalization ($1.6 \pm 0.5 \text{ mN m}^{-1}$). It was concluded that the surface interaction of the SiO_x and p-Si₃N₄ functionalizations to the s-PSM are stronger as the surface interaction in the study measured by Mey *et al.*^[235]

As the membrane rupture tension of DOPC is at $\sim 10 \text{ mN m}^{-1}$,^[236,237] the f-PSMs on SiO_x functionalized substrates were assumed to be in a critical state due to huge lateral tension. However, during the measurements, the f-PSMs were stable. The incorporation of Chol is known to stabilize the membrane,^[119] as it was shown that the rupture tension increases to $\sim 19 \text{ mN m}^{-1}$ for membranes containing 50 mol %

Chol.^[237] The measurement of phase-separated membranes with the lipid composition of DOPC/sphingomyelin (SM)/Chol therefore were expected to be less prone to rupture during the experiments compared to pure DOPC membranes.

The SiO_x functionalization has the advantage that the phase separation of l_o/l_d phase-separated membranes is visible in the f-PSM and s-PSM (figure 5.4). The interplay of tension and lipid composition is of great interest, therefore membrane tension of the two phases were also measured on SiO_x functionalized substrates. The two different membrane phases were modeled by different membrane compositions. DOPC/membrane marker (99.5:0.5) was used to mimic the l_d phase and SM_{porc}/Chol/ATTO655-DOPE (59.5:39.5:1) for the l_o phase.^[238] The l_d phase had a membrane tension of $10.5 \pm 4.3 \text{ mN m}^{-1}$ and the l_o phase $6.7 \pm 4.0 \text{ mN m}^{-1}$ (figure 5.7, table 5.1). The membrane tension of the l_d and l_o phase are not distinct within the errors of the measurement, as also seen in the statistical analysis (table A.9).

The l_o phase, high ordered structure, is expected to show higher membrane tension on SiO_x functionalized substrates compared to l_d phase, low ordered structure, because membranes of DOPC PSMs shows lower membrane tensions compared to membranes with a higher ordering like DOPC/Chol.^[119,234] Such an effect was also measured with POPC membranes (table A.2).^[239]

The deviation of the expected result to the obtained results in this work can be explained taking the surface geometry and membrane surface interaction into account. The strength of the surface membrane interaction is not only a factor of surface hydrophobicity, but also roughness,^[240] as known from wetting phenomena. Different studies were done with l_d and l_o phases on curved surfaces. In all studies, the l_d phase is present in areas with the higher curvature compared to the l_o phase.^[241–243] The l_o phase is associated with less curved areas, because it has a higher bending stiffness as the l_d phase and prefers flat surfaces.^[243–254]

The surface roughness of SiO_x functionalized substrates was determined to be $0.49 \pm 0.03 \text{ nm}$.^[148] The differences of the expected and measured membrane tensions on SiO_x functionalized substrates with l_o and l_d mimicking membranes can be explained by surface interactions. The l_o mimicking membrane has a lower adhesion, as it is not able to follow surface topography due to high bending energies needed to do so, while l_d membranes exhibit a low bending energy and therefore gain higher adhesional energies. The measured membrane tensions on SiO_x functionalization are too widely spread to confirm or refute this assumption.

A comparison of membrane tension from different surface functionalizations shows, that membrane tension is affected by functionalization. Gold mercaptoalcohol and p-Si₃N₄ have nearly the same membrane tensions, only SiO_x has higher membrane

tension by a factor of 7; this is close to the rupture tension of DOPC. Surface roughness can have an influence on membrane tension. If membrane is stiffer than the surface interaction can decrease, and the membrane tension also decreases. The physiological cell membrane tension of 0.01 to 0.15 mN m⁻¹^[215,216] could not be reached with the different functionalizations. The membrane tension in f-PSMs is up to 70 times higher as the overall membrane tension of cells. Despite this big difference, the model system PSM is still more cell-similar than many other model systems, due to the different adhesion areas.

5.1.3. Diffusion in pore-spanning membranes (PSMs)

Interferometric scattering microscopy (iSCAT)

As lipid rafts are transient lipid containing structures, diffusion of lipids is a major parameter to study the existence and properties of lipid rafts. The lipid diffusion is a property of each biomimetic membrane system influenced by artificial factors like membrane tension, contact to solid supports, and lipid composition. Therefore, for every surface functionalization, also lipid diffusion was characterized. Since fluorescence-based techniques are not available to quantify the diffusion coefficient of the lipids in the s-PSM, for the mercaptoalcohol gold functionalization due to quenching, interferometric scattering microscopy (iSCAT) measurements were used (chapter 3.3.2). iSCAT is a single particle tracking (SPT) method in which a gold nano particle (GNP) is coupled *via* streptavidin biotinyl to 1,2-dioleoyl-sn-glycero-3-phosphoethanolamine-N-cap-biotinyl (cb-DOPE) and its movement is recorded using interference. A time series was recorded for 5 s with a temporal resolution of 1 kHz. From the trajectories of the GNP, the diffusion coefficient was determined using covariance-based estimation.^[154,255] This measurement was conducted with two different functionalized surfaces, 6MH-Au and p-Si₃N₄.

Three different GNP paths were observed during iSCAT measurements. First, the GNP diffusion was only detected on the s-PSM (figure 5.8 A). Second, the GNP diffused on both membrane areas, the s-PSM and f-PSM (figure 5.8 B). Third, the GNP diffusion was only detectable on the f-PSM (figure 5.8 C).

The GNP diffused freely on both, the f-PSM and s-PSM. The diffusion coefficient from the GNP was determined separately on both parts of the PSM system and is summarized in table 5.2 and figure 5.9. Comparing the diffusion on the f-PSM for both functionalizations (figure 5.9 A), the motion of the GNP on f-PSMs prepared on p-Si₃N₄ functionalized substrates was faster ($2.6 \pm 1.0 \mu\text{m}^2 \text{s}^{-1}$) than on 6MH-Au functionalized substrates ($1.8 \pm 0.7 \mu\text{m}^2 \text{s}^{-1}$, figure 5.9 A, table 5.2).

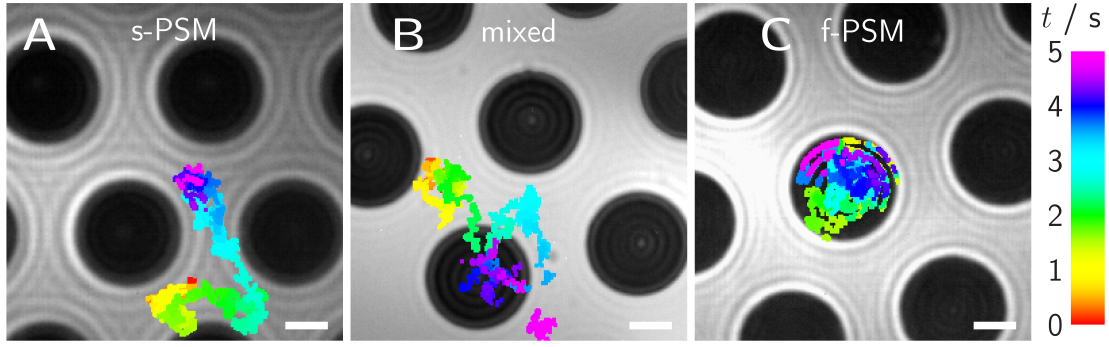


Figure 5.8.: Raw iSCAT images from videos recorded at 1 kHz for 5 s overlaid with trajectories of 40 nm GNPs attached to cb-DOPE lipids diffusing in a DOPC membrane on a p-Si₃N₄ functionalized substrate. A) Trajectory of a GNP on the s-PSM. B) Trajectory of a GNP moving on the s-PSM, crossing over to the f-PSM and return to the s-PSM. C) Trajectory of a GNP trapped in the f-PSM. The color code shows the time evolution in each case. Scale bar 2 μm

Table 5.2.: The diffusion coefficient (D) were measured on different functionalized substrates to generate PSMs composed of DOPC/cb-DOPE/ATTO532-DOPE (98.8:1:0.2). The surface functionalizations were plasma cleaned silicon nitride (p-Si₃N₄) and 6-mercapto-1-hexanol on gold (6MH-Au). The diffusion coefficient was measured with interferometric scattering microscopy (iSCAT) and from gold nano particles (GNPs), which are covered with streptavidin and connected *via* streptavidin biotinyl bond to the cb-DOPE in the membrane. The different freestanding pore-spanning membrane (f-PSM) and solid supported pore-spanning membrane (s-PSM) were analyzed separately. The mean values and the standard deviations were listed with the number of taken trajectories (N).

System / Surface	D [$\mu\text{m}^2 \text{s}^{-1}$]	N
f-PSM / p-Si ₃ N ₄	2.6 ± 1.0	28
s-PSM / p-Si ₃ N ₄	0.8 ± 0.5	745
f-PSM / 6MH-Au	1.8 ± 0.7	89
s-PSM / 6MH-Au	1.9 ± 0.7	279

The differences in f-PSM diffusion constants are explained by the difference in membrane tension of the two different functionalizations. The membrane tension of f-PSM with 6MH-Au functionalized substrates is $0.6 \pm 0.4 \text{ mN m}^{-1}$, which is a factor of 3 lower than found for the p-Si₃N₄ functionalized substrates $1.6 \pm 0.5 \text{ mN m}^{-1}$. The diffusion constant increases from 6MH-Au functionalized substrates with $1.8 \pm 0.5 \mu\text{m}^2 \text{s}^{-1}$ to p-Si₃N₄ functionalized substrates with $2.6 \pm 1.0 \mu\text{m}^2 \text{s}^{-1}$. This dependency of membrane tension on diffusion was also shown in molecular dynamics simulations (MDs)^[256,257] and was also measured using FCS on GUVs, using micro pipette aspiration to tune the GUV tension.^[258] Interestingly, bulk methods like fluorescence recovery after photobleaching (FRAP) on GUVs and the micro pipette aspiration did not enable to measure the increase found in single lipid diffusion studies.^[259]

5. Pore-spanning membranes (PSMs)

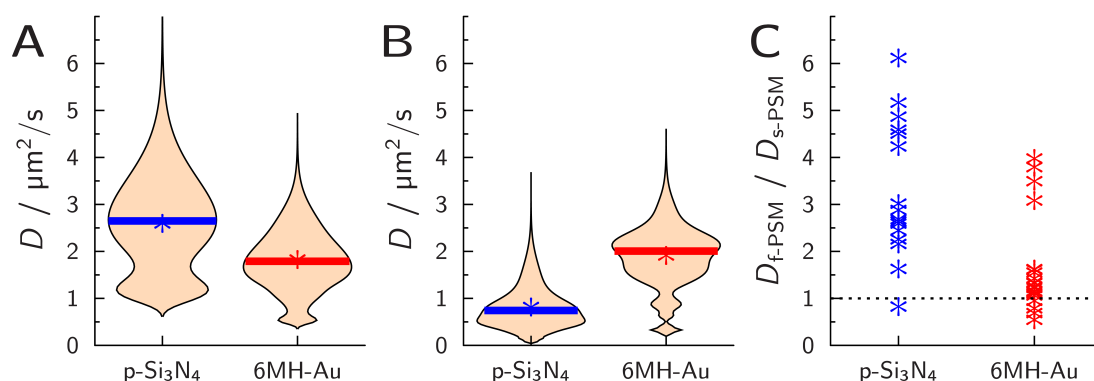


Figure 5.9.: The diffusion coefficient (D) measured with interferometric scattering microscopy (iSCAT) on the pore-spanning membranes (PSMs) composed of DOPC/cb-DOPE/ATTO532-DOPE (98.8:1:0.2). The substrates were functionalized with plasma cleaned silicon nitride (p-Si₃N₄) or 6-mercapto-1-hexanol on gold (6MH-Au). The diffusion coefficient of the freestanding pore-spanning membrane (f-PSM) (A) and solid supported pore-spanning membrane (s-PSM) (B) are compared to the different functionalizations. Some particles were observed in the f-PSM and s-PSM and from these particles the diffusion ratio ($D_{\text{f-PSM}}/D_{\text{s-PSM}}$) were plotted in C ($N(\text{p-Si}_3\text{N}_4)=16$; $N(6\text{MH-Au})=21$). The numbers and mean values are listed in table 5.2.

The GNPs on the s-PSM with the p-Si₃N₄ functionalization were slower than the GNPs on the s-PSM with the 6MH-Au functionalization (figure 5.9 B, table 5.2). The substrate membrane interaction decreases the lipid diffusion. The iSCAT measurements of DOPC membranes supported on glass and or in GUVs show the influence of the membrane support. Hsieh *et al.* measured the diffusion coefficient on SSM to $0.22 \mu\text{m}^2 \text{s}^{-1}$ ^[260] which has an high membrane adhesion, and Spindler *et al.* measured the diffusion coefficient on GUVs without any adhesion to $4.88 \mu\text{m}^2 \text{s}^{-1}$.^[261] Diaz *et al.* showed with protein diffusion directly on glass ($0.3 \pm 0.1 \mu\text{m}^2 \text{s}^{-1}$, high adhesion) or with a PEG cushions between the bilayer and the glass surface ($3.5 \pm 0.4 \mu\text{m}^2 \text{s}^{-1}$, low adhesion) that different membrane surface adhesions had a comparable influence on the diffusion coefficient.^[106] This indicates that the membrane substrate interaction was stronger when the substrate was functionalized with p-Si₃N₄ compared to the 6MH-Au functionalization. The stronger substrate membrane interaction was also shown by measurements of the membrane tension on these systems (table 5.1). High adhesion of the s-PSM is expected to result in a high lateral tension of the f-PSM and vice versa (p-Si₃N₄ functionalization: $\sigma = 1.6 \pm 0.5 \text{ mN m}^{-1}$ and $D = 0.8 \pm 0.5 \mu\text{m}^2 \text{s}^{-1}$; 6MH-Au functionalization: $\sigma = 0.6 \pm 0.4 \text{ mN m}^{-1}$ and $D = 1.9 \pm 0.7 \mu\text{m}^2 \text{s}^{-1}$).

A direct comparison of the GNP diffusion connected to the f-PSM and s-PSM was done using particles which were observed on both regions in one experiment

(figure 5.9 C). The resulting diffusion ratio ($D_{f\text{-PSM}}/D_{s\text{-PSM}}$) describes the factor of how much faster the GNP is on the f-PSM compared to s-PSM. The diffusion ratio on the p-Si₃N₄ functionalized substrates showed different accumulations and ranged from 1 to 6. In contrast to the strong difference between f-PSM and s-PSM, the diffusion ratio of GNPs from membranes prepared on 6MH-Au functionalized surfaces is one. Indicating that the GNP diffusion constant of f-PSM and s-PSM is the same.

With iSCAT, only diffusion in the top leaflet is detectable, which might explain the diffusion constant ratio of one for the 6MH-Au System, when interaction between membrane and surface is mainly influencing the bottom leaflet. A disadvantage of the iSCAT measurements were the unknown connection points from the GNP to the membrane. The GNP is coated with streptavidin which had four binding sides to biotin and two bindings each on the opposite side. So each streptavidin is able to bind two biotin labeled lipids and the GNP is coated with more than one streptavidin. In these results the GNP is able to bind several biotin labeled lipids. Liao *et al.* analyzed different sizes of GNP to evaluate the influence of the unknown GNP membrane binding points.^[262] The smaller GNPs were faster than the greater ones (table A.1) which indicates an influence of the binding sites or size of the GNPs to the diffusion constant.

Fluorescence correlation spectroscopy (FCS)

To investigate the diffusion within both leaflets and ensure only single lipid diffusion is measured, Z-scan FCS measurements were performed (chapter 3.3.1). The measurements were done on SiO_x functionalized substrates, because they had the advantage that l_o/l_d phase-separated PSMs were detectable in the f-PSM and s-PSM (figure 5.4). To be able to distinguish between these phases with Z-scan FCS, different lipid composition were used to mimic the l_d and l_o phase. The l_d phase was mimicked with a DOPC/ATTO488-DOPE (99.5:0.5) membrane and the l_o phase was mimicked with a SM_{porc}/Chol/ATTO655-DOPE (59.5:39.5:1) membrane. The fluorophores for the Z-scan FCS measurements were added in low concentrations (1×10^{-3} – 1×10^{-5} mol %). The fluorophores which were used to measure the diffusion in the l_d phase were ATTO655-DOPE or TexasRed-DHPE and for the l_o phase BODIPY-Chol or naphtho[2,3-a]pyrene (naphthopyrene).^[140] The resulting diffusion coefficients are listed in table 5.3 and visualized in figure 5.10. The measurements demonstrate, that ATTO655-DOPE and TexasRed-DHPE had the same diffusion constants in the f-PSM (figure 5.10 A).

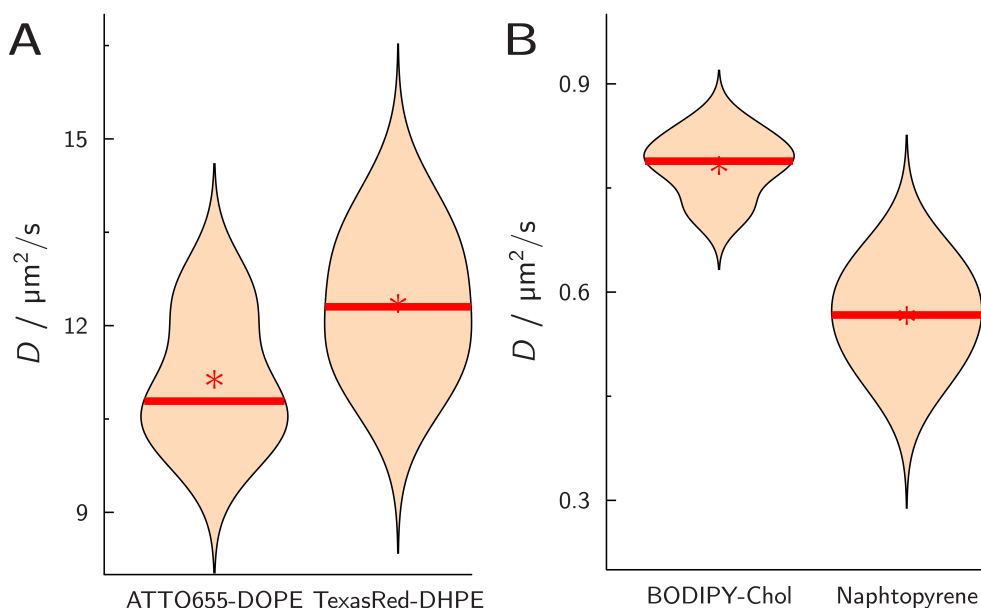


Figure 5.10.: The diffusion coefficient (D) measured with Z-scan fluorescence correlation spectroscopy (Z-scan FCS) on the freestanding pore-spanning membrane (f-PSM). The substrates were functionalized with SiO_x . In A) the lipid composition of the membrane was DOPC/ATTO488-DOPE (99.5:0.5) doped with the Z-scan FCS fluorophores ATTO655-DOPE or TexasRed-DHPE and in B) $\text{SM}_{\text{porc}}/\text{Chol}/\text{ATTO655-DOPE}$ (59.5:39.5:1) doped with the Z-scan FCS fluorophores BODIPY-Chol or naphthopyrene.

The measurement of the diffusion constants in the f-PSM with l_o phase mimicking membrane was done with BODIPY-Chol and naphthopyrene (figure 5.10 B). The diffusion of BODIPY-Chol ($0.78 \pm 0.05 \mu\text{m}^2 \text{s}^{-1}$) was faster than the diffusion of naphthopyrene ($0.57 \pm 0.07 \mu\text{m}^2 \text{s}^{-1}$), but both diffusion coefficients were compared with the lipids in the l_d phase by a factor of 13 to 20 slower, which still allows for qualitative interpretations.

The diffusion coefficient of different phase-separated membranes were measured and reported in previous literature (table A.1). The diffusion coefficient of phase-separated GUVs composed of DOPC/ $\text{SM}_{\text{porc}}/\text{Chol}$ (2:2:1) was $6.1 \mu\text{m}^2 \text{s}^{-1}$ in the l_d phase which was slower by a factor of 20 in the l_o phase ($0.3 \mu\text{m}^2 \text{s}^{-1}$) measured with Z-scan FCS.^[263] A second example with non-adhered membranes (GUVs) composed of DOPC/ $\text{SM}_{\text{C}_{18:0}}/\text{Chol}$ (1:1:1) was measured with FCS. The diffusion was faster by a factor of 20 in the l_d phase compared to the diffusion in the l_o phase. ($5.15 \mu\text{m}^2 \text{s}^{-1}$ l_d and $0.255 \mu\text{m}^2 \text{s}^{-1}$ l_o phase).^[264] The difference in the diffusion coefficient of the l_o and l_d phase in the f-PSM is in agreement with previous literature.

The diffusion coefficient of DOPC f-PSM mimicking the l_d phase ($\sim 11.8 \mu\text{m}^2 \text{s}^{-1}$) is higher than the diffusion coefficient measured in DOPC GUVs. Different FCS measurements were reported in DOPC GUVs with diffusion coefficients from 6.3 to

Table 5.3.: Diffusion coefficients (D) were measured with Z-scan fluorescence correlation spectroscopy (Z-scan FCS) in the freestanding pore-spanning membrane (f-PSM) composed of DOPC/ATTO488-DOPE (99.5:0.5) for the liquid disordered (l_d) phase and SM_{porc}/Chol/ATTO655-DOPE (59.5:39.5:1) for the l_o phase on silicon oxide (SiO_x) functionalized substrates. The different FCS fluorophores were added in 1×10^{-3} to 1×10^{-5} mol %. The mean values and the standard deviations were listed with the number of measured f-PSM trajectories (N).

Phase	Fluorophore	D [$\mu\text{m}^2 \text{s}^{-1}$]	N
l_d	ATTO655-DOPE	11.2 ± 0.9	3
l_d	TexasRed-DHPE	12.4 ± 1.1	6
l_o	BODIPY-Chol	0.78 ± 0.05	4
l_o	naphthopyrene	0.57 ± 0.07	6

$8.5 \mu\text{m}^2 \text{s}^{-1}$ (table A.1).^[170,264–266] However, as stated before this can be explained by the increased membrane tension of f-PSM compared to GUVs.^[256–258] The membrane tension of GUVs can be assumed to be zero and the membrane tension of the f-PSM composed of DOPC on SiO_x functionalized substrates was 10.5 mN m^{-1} (table 5.1).

The diffusion coefficient of the f-PSM composed of DOPC/POPE/POPS/Chol (5:2:1:2) was measured by Schwenen *et al.* with FCS and 6MH-Au functionalized substrates, which were found to be $\sim 7.55 \mu\text{m}^2 \text{s}^{-1}$.^[267] The diffusion coefficient found by Schwenen *et al.* is roughly lower by a factor of 1.5 than the diffusion coefficient measured on f-PSM composed of DOPC on SiO_x functionalized substrates. As described in literature, Chol has an influence on the diffusion constant within the membranes. The increase of the Chol content from 20 to 66 mol % in a DOPC GUVs reduced the diffusion coefficient by a factor of 2, which was measured with FCS.^[264] Schwenen *et al.* used 20 mol % Chol which was expected to decrease lipid diffusion compared to the membrane systems used in this thesis.

In contrast to the literature, the comparison of FCS measurements of Schwenen *et al.* with the iSCAT measurements in the f-PSM on the 6MH-Au functionalized substrates (FCS = $\sim 7.55 \mu\text{m}^2 \text{s}^{-1}$,^[267] iSCAT = $1.8 \mu\text{m}^2 \text{s}^{-1}$), shows that measurements without Chol had a lower diffusion compared to measurements executed on Chol rich membranes in f-PSMs. The measurements were performed with two different techniques. The comparison of the two techniques on the same measurement system (DOPC GUVs), resulted in diffusion coefficients of $4.88 \mu\text{m}^2 \text{s}^{-1}$ ^[261] (iSCAT) and of 6.3 to $8.5 \mu\text{m}^2 \text{s}^{-1}$ (FCS, table A.1).^[170,264–266] The difference of the techniques in GUVs can be sum up due to the effect of the size from the analyzed molecule.^[262] While iSCAT only takes the upper leaflet of the lipid membrane in the f-PSM on a 6MH-Au functionalized substrate into account, FCS considers both leaflets, which

might induce the differences when comparing these techniques as the substrate functionalization also influences the bilayer coupling.

In this work the lipid diffusion was measured with two different techniques, iSCAT and FCS in PSMs. The diffusion coefficients depended on the functionalization of the substrate and the technique. iSCAT is a non-fluorescence technique and was used to measure the diffusion of the s-PSM and f-PSM. FCS is capable of distinguishing l_o and l_d phase within the f-PSM. The measured diffusion constant of the l_o phase was in the range of the lipid diffusion of cellular membranes (from 0.3 to $5.4 \mu\text{m}^2 \text{s}^{-1}$).^[266,268–271] Despite the still too large membrane tension, it matches this model appropriate to study diffusion control mechanisms for processes involved in raft formation.

5.2. Phase separation in pore-spanning membranes (PSMs)

Utilizing SiO_x functionalized substrates, phase separation behavior in dependency of Chol content and temperature was studied on f-PSMs and s-PSMs. Therefore, GUVs composed of DOPC/ SM_{porc} /Chol were spread on these substrates to generate the PSMs. The Chol content was varied between 0 to 50 mol % while keeping DOPC and SM_{porc} content all the time at a 1:1 ratio. To measure phase separation behavior of l_d and l_o phases, TexasRed-DHPE was used as a l_d phase marker^[139,140] and BODIPY-Chol as a l_o phase marker.^[140,142] The temperature was varied between 25 and 55 °C. The measurement of each fluorescence image was done at a certain temperature. Fluorescence images were recorded only once the temperature reached a stable plateau.

Figure 5.11 shows typical fluorescence micrographs of PSMs with BODIPY-Chol (green) and TexasRed-DHPE (red) being in a phase-separated state ($T = 25 \text{ °C}$) and in a non-phase-separated state ($T = 55 \text{ °C}$). To calculate absolute intensities, an uncovered pore was indicated with an x in each fluorescence image which was used for background intensity calculations. Two different lipid compositions are shown, i.e., DOPC/ SM_{porc} /Chol (41.5:41.5:17) (A) and DOPC/ SM_{porc} /Chol (47:47:6) (B). At 55 °C, the non-phase-separated state, the fluorophores show red and green fluorescence co-localized in f-PSM and s-PSM (figure 5.11 A and B, $T = 55 \text{ °C}$). As discussed before, s-PSM intensity was diminished compared to f-PSM intensity due to quenching effects.^[148] Co-localization of both lipid phase markers proves that only one phase exists and both fluorophores are soluble in the l_d phase as well as the temperature was above the miscible temperature. That means that the membrane

was existent in the l_d phase. At 25 °C, a phase-separated state of the PSM was found (figure 5.11 A and B, $T = 25$ °C). While the s-PSMs showed a homogeneous TexasRed-DHPE fluorescence, no TexasRed-DHPE fluorescence intensity was measured in the f-PSMs.

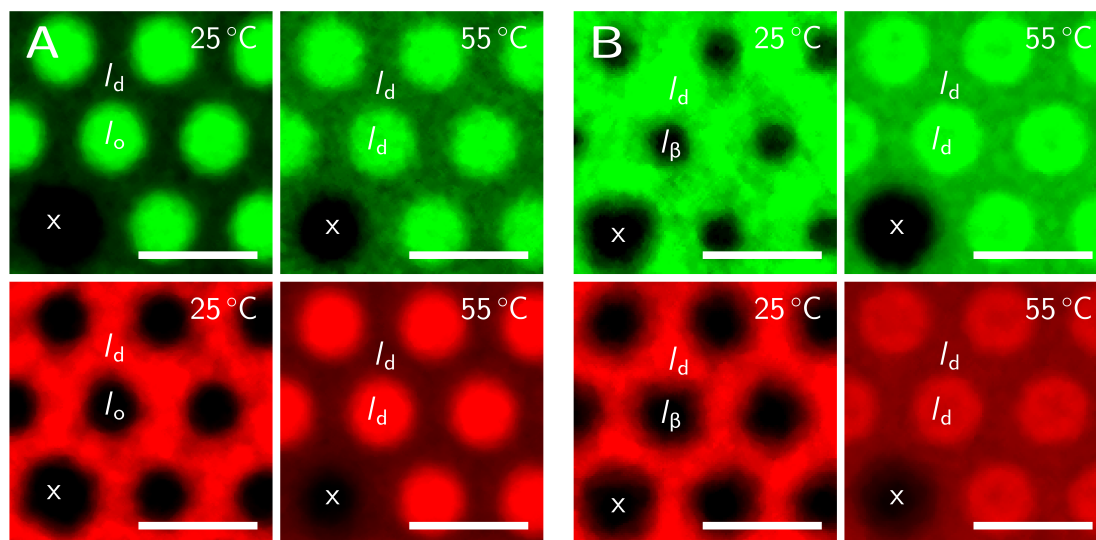


Figure 5.11.: Fluorescence micrographs of phase-separated pore-spanning membranes (PSMs) at 25 °C and 55 °C. The green channel shows the BODIPY-Chol fluorescence, while the red channels shows the TexasRed-DHPE fluorescence. A) PSM composed of DOPC/SM_{porc}/Chol (41.5:41.5:17). B) PSM composed of DOPC/SM_{porc}/Chol (47:47:6). The gel like (l_β), the liquid ordered (l_o) and the liquid disordered (l_d) phases are assigned to the freestanding pore-spanning membrane (f-PSM) and solid supported pore-spanning membrane (s-PSM) according to the partition of the two fluorophores BODIPY-Chol and TexasRed-DHPE. An uncovered pore is marked by an x. Scale bar 2 μ m.

The f-PSMs showed a clear BODIPY-Chol fluorescence signal with higher Chol content (figure 5.11 A, $T = 25$ °C), proving, that a f-PSM was still existent. The BODIPY-Chol fluorescence intensity of the s-PSM was still homogeneously distributed, but compared to the absolute intensity in the non-phase-separated state, the intensity level was lowered. The membrane composition DOPC/SM_{porc}/Chol (41.5:41.5:17) excluded TexasRed-DHPE from the f-PSM while BODIPY-Chol was enriched, indicating that the f-PSM is composed of the l_o phase^[140,142] and the s-PSM of the l_d phase.

Interestingly, a mixture with low Chol content at 25 °C showed no fluorescence intensity in the f-PSM at all, neither from the l_d nor from the l_o phase marker (figure 5.11 B, $T = 25$ °C). By heating up the system to 55 °C, reaching the non-phase-separated state, both fluorophores were co-localized in the f-PSMs. This proves that even if no fluorescence is visible, a membrane suspending the pore is existent at 25 °C and this membrane is excluding both fluorescence markers. Ternary phase

diagrams of DOPC/SM/Chol do not only describe the l_d and l_o phase, but also the gel like (l_β) phase which is present if the content of SM is very high.^[97–99,264,272–275] Both fluorescent lipid phase markers are excluded from the l_β phase.^[140,170] At low Chol content the f-PSM was composed of the l_β phase and the s-PSM was composed of the l_d phase.

Based on the assignment of the three detectable phases, temperature and Chol content were studied systematically to extract the transition temperature (T_M) by analyzing fluorescence images. The TexasRed-DHPE intensity was used to extract quantitative information, as TexasRed-DHPE is known to distribute to almost 100% in the l_d phase.^[139,140] In contrast, BODIPY-Chol partitions only about 50 to 80% into the l_o phase^[142,229] and was used primarily to distinguish between the l_β and l_o phase. To extract the transition temperature, the ratio of fluorescence intensities of the f-PSM ($I_{f\text{-PSM}}$) and s-PSM ($I_{s\text{-PSM}}$) were measured for several temperatures, as explained in chapter 3.4.2. The intensity ratios were plotted against the temperature and showed a sigmoidal curve, where the turning point reflects the transition temperature.

The phase separation l_β/l_d is shown in figure 5.12 with the composition of DOPC/SM_{porc}/Chol (46:46:8) along a rising temperature ramp. The fluorescence micrographs (figure 5.12, top, BODIPY-Chol (green) and TexasRed-DHPE (red)) at $T = 25^\circ\text{C}$ clearly showed that both fluorophores were excluded from the f-PSMs indicating that the f-PSMs were existent in the l_β phase. TexasRed-DHPE fluorescence was found in the s-PSM representing the l_d phase. At 55°C , a homogeneous distribution of the TexasRed-DHPE fluorophore in the f-PSM and in the s-PSM was observed. Hence, at Chol content of 8 mol%, a phase transition between a l_β/l_d phase-separated membrane to a homogeneous l_d phase occurred. From the plotted intensity ratio as a function of temperature (figure 5.12, bottom), a T_M of 40.7°C was extracted. This phase separation were observed for Chol contents of 0 to 10 mol%.

By increasing the Chol content to more than 10 mol%, the f-PSM formed a l_o phase instead of a l_β phase. A PSM composed of DOPC/SM_{porc}/Chol (42.5:42.5:15) is shown in figure 5.13. The fluorescence micrographs (figure 5.13, top, BODIPY-Chol (green) and TexasRed-DHPE (red)) at $T = 25^\circ\text{C}$ demonstrated that TexasRed-DHPE was excluded from the f-PSM, while BODIPY-Chol was enriched proving the existence of the l_o phase in the f-PSM. TexasRed-DHPE fluorescence was found in the s-PSM, highlighting the l_d phase. At 55°C , a homogeneous distribution of the TexasRed-DHPE in the f-PSM and in the s-PSM was observed. Hence, at a Chol content of 15 mol%, a phase transition between a l_o/l_d phase-separated membrane to a homogeneous l_d phase occurred. From the plotted intensity ratio as a function

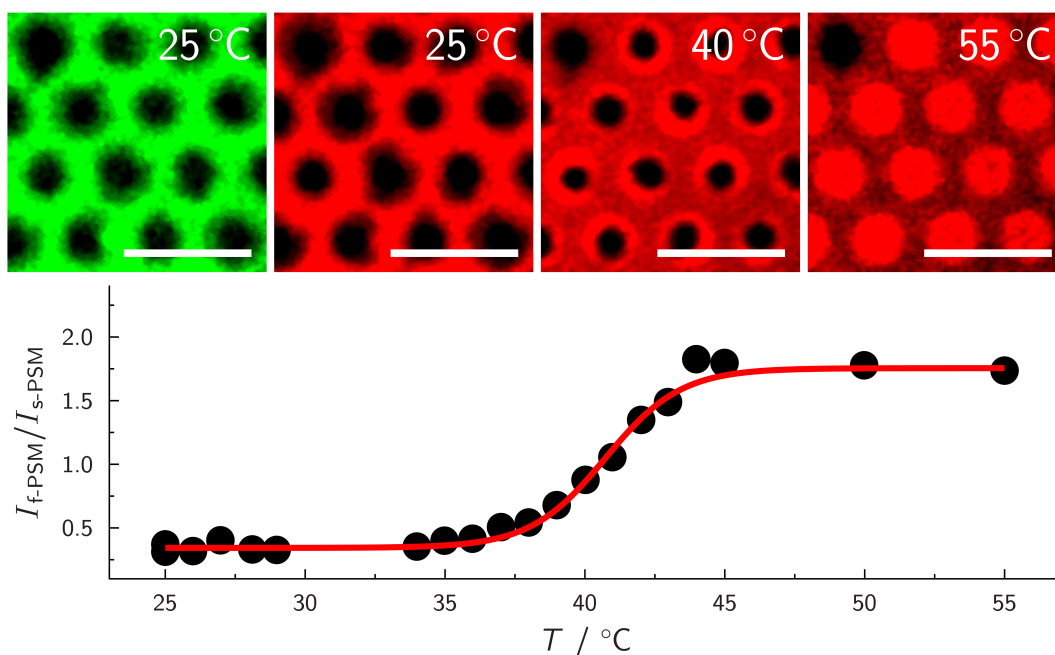


Figure 5.12.: (Top) Fluorescence micrographs of a PSM composed of DOPC/ SM_{porc} /Chol (46:46:8) at different temperatures. The BODIPY-Chol (green) and the TexasRed-DHPE (red) fluorescence images at $T = 25^\circ\text{C}$ indicate that the PSM phase-separates into a l_β and l_d phase. The TexasRed-DHPE fluorescence images (red) at $T = 25, 40$ and 55°C demonstrate the phase transition from the l_β/l_d phase-separated membrane to a homogeneous l_d phase, with the visualization of phase separation in the f-PSM. (Bottom) Fluorescence intensity ratio as a function of temperature resulted in a sigmoidal curve which was fitted to the data resulting in $T_M = 40.7^\circ\text{C}$. Scale bar $3\ \mu\text{m}$.

of temperature (figure 5.14, bottom), a T_M of 39.1°C was extracted. This phase separation behavior was observed for Chol contents of 10 to 50 mol %.

Another phase transition between a l_o/l_d phase-separated membrane to a homogeneous l_d phase was shown in (figure 5.14) for a Chol content of 25 mol %. As shown in figure 5.13, the fluorescence micrographs (figure 5.14, top, BODIPY-Chol (green) and TexasRed-DHPE (red)) at $T = 25^\circ\text{C}$ demonstrate that TexasRed-DHPE was excluded from the f-PSM, while BODIPY-Chol was enriched assigning the f-PSM to the l_o phase and the s-PSM to the l_d phase. At 55°C , a homogeneous distribution of the TexasRed-DHPE fluorophore in the f-PSM and in the s-PSM was observed. Varying the Chol contents between 0 and 18 mol %, a phase separation in the f-PSM was detected (figure 5.12 and 5.13). At higher Chol contents no phase separation in the f-PSM was found, during the temperature ramp measurement (figure 5.14, top, TexasRed-DHPE (red) from 25 to 55°C). The increase of the fluorescence intensity from TexasRed-DHPE in the f-PSM was measured and a T_M of 45.7°C was extracted.

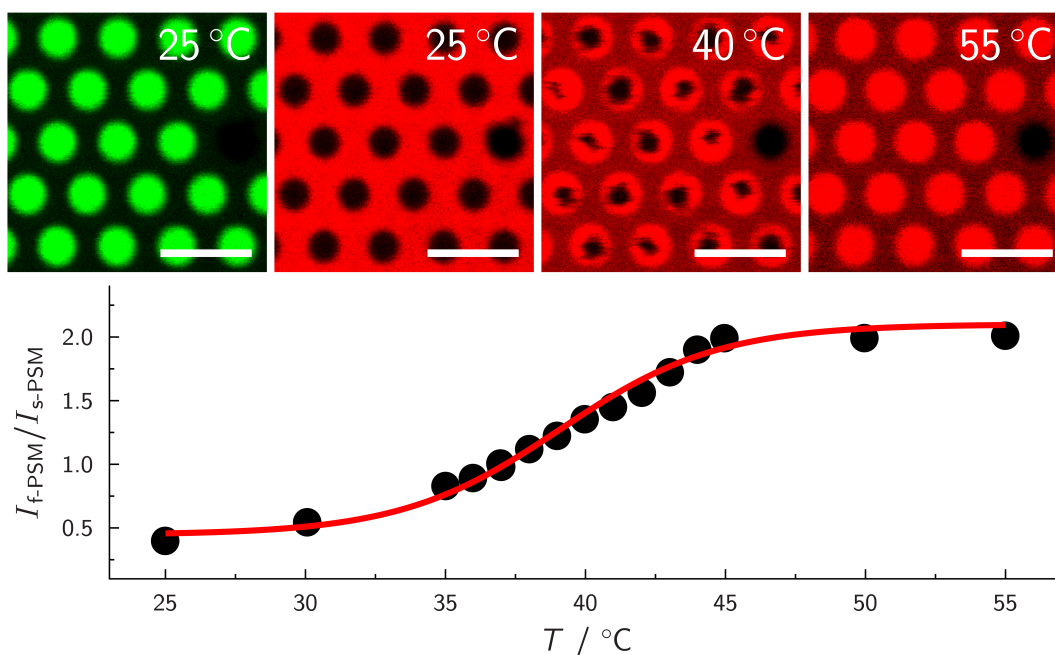


Figure 5.13.: (Top) Fluorescence micrographs of a PSM composed of DOPC/ SM_{porc} /Chol (42.5:42.5:15) at different temperatures. The BODIPY-Chol (green) and the TexasRed-DHPE (red) fluorescence images at $T = 25\text{ }^{\circ}\text{C}$ indicate that the PSM phase-separates into a l_o and l_d phase. The TexasRed-DHPE fluorescence images (red) at $T = 25, 40$ and $55\text{ }^{\circ}\text{C}$ demonstrate the phase transition from the l_o/l_d phase-separated membrane to a homogeneous l_d phase, with the visualization of phase separation in the f-PSM. (Bottom) Fluorescence intensity ratio as a function of temperature resulted in a sigmoidal curve which was fitted to the data resulting in $T_M = 39.1\text{ }^{\circ}\text{C}$. Scale bar $3\text{ }\mu\text{m}$.

T_{MS} for all measured Chol concentrations were plotted in the phase diagram (figure 5.15), indicating the border regions of the already described phase transitions which were possible in the PSM system. At high temperatures, the lipids were homogeneously distributed in the PSMs and independent from the Chol concentration. From 0 mol % Chol up to 8 %, only a l_β/l_d phase separation was found. From 11 mol % to the highest measured Chol concentration, only a l_o/l_d phase separation was detected. At concentrations of 9 mol % and 10 mol % Chol, both phase separation types were measured. This unclear border is a fact of the distribution of the GUVs which have up to 5 % composition fluctuations within the population.^[272,274,276,277] The highest used Chol concentration was 50 mol % which is still below the maximum of soluble Chol that was determined to be 66 mol % for DOPC membranes.^[278,279] The upper limit of 50 mol % for Chol was chosen to ensure that the Chol content in the membranes is unaffected by the maximum incorporation limit of Chol.

In previous literature, different phase diagrams from ternary lipid mixtures were reported on model membrane systems with a homogeneous membrane adhesion.^[201]

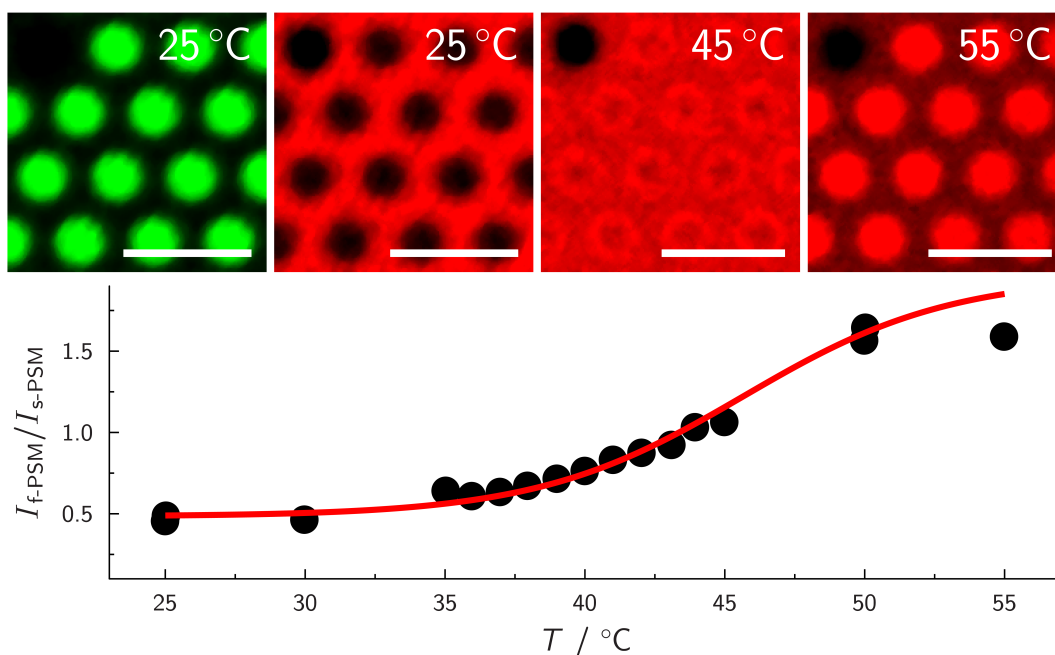


Figure 5.14.: (Top) Fluorescence micrographs of a PSM composed of DOPC/ SM_{porc} /Chol (37.5:37.5:25) at different temperatures. The BODIPY-Chol (green) and the TexasRed-DHPE (red) fluorescence images at $T = 25^\circ\text{C}$ indicate that the PSM phase-separates into a l_o and l_d phase. The TexasRed-DHPE fluorescence images (red) at $T = 25, 40$ and 55°C demonstrate the phase transition from the l_o/l_d phase-separated membrane to a homogeneous l_d phase, without a visualization of phase separation in the f-PSM. (Bottom) Fluorescence intensity ratio as a function of temperature resulted in a sigmoidal curve which was fitted to the data resulting in $T_M = 45.7^\circ\text{C}$. Scale bar $2\ \mu\text{m}$.

The difference of this measured phase diagram (figure 5.15) to ones reported for vesicles or SSM is explainable due to different adhesion properties for the membrane in PSM systems which basically have two different adhesion areas (f-PSM, s-PSM). A theoretical work from Lipowsky *et al.* described the influence of different adhesion areas on continuous membranes composed of POPC/Chol.^[1,280] The phase diagram of the membrane in each adhesion region on its own is equal to the phase diagram of homogeneously adhered membranes. The overall phase diagram is changed, as different lipids show varying preferences to the different adhesion areas, resulting in a kind of lipid sorting induced by the adhesional properties of system. The deviations of the phase diagram for membrane systems with homogeneous adhesion to lipid membranes with heterogeneous adhesion can be summarized in three statements for the system used within this work:^[1,280] First, an increase in the difference of adhesional energy between f-PSM and s-PSM results in a broadening of the overall phase separation region within the phase diagram. Second, the maximum of T_M of the phase-separated region for the whole system does not change by increasing the difference of adhesional

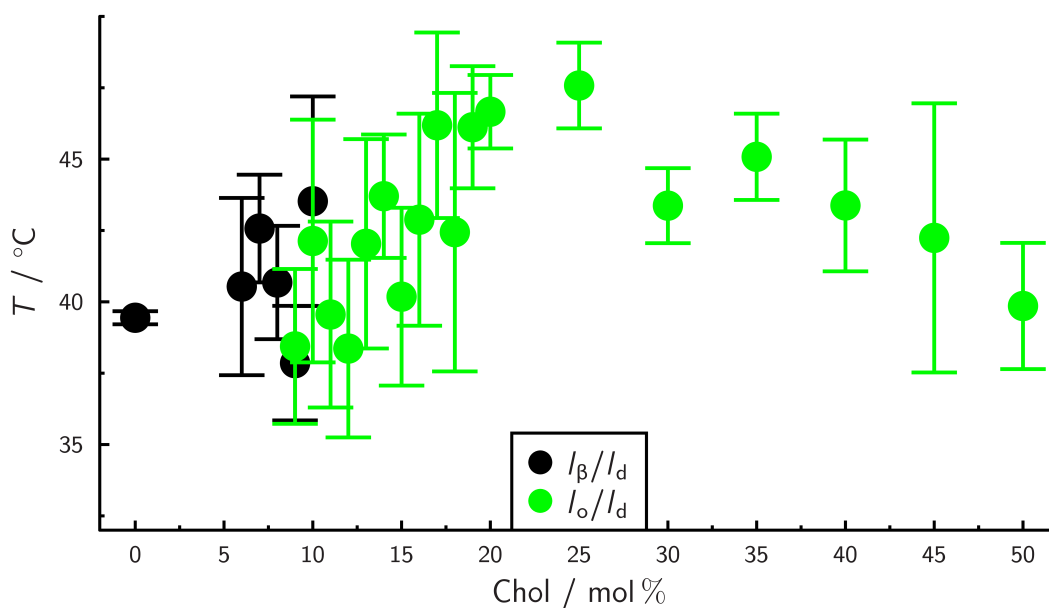


Figure 5.15.: phase diagram by changing the Chol content from 0 to 50 mol% on pore-spanning membranes (PSMs) and the lipid ratio between DOPC and SM_{porc} was one. The different transition temperature (T_M) from gel like (l_β)/liquid disordered (l_d) and liquid ordered (l_o)/ l_d to the homogeneous l_d phase were plotted in black and green respectively.

energy between f-PSM and s-PSM. Third, lipids have a preferential area (f-PSM, s-PSM) depending on their properties within the lipid mixture which can result in differing lipid compositions for the f-PSM and s-PSM. Phase separation will occur either in the f-PSM or the s-PSM, but never in both simultaneously.^[1,280] These three theoretical statements are experimentally studied using the system of PSM as an example for heterogeneous adhesion and comparing these results to previous literature with experiments done with vesicles or SSMs as examples for homogeneously adhered membranes.

Starting with the first statement from Lipowsky *et al.*, an increase in the adhesion difference must result in a broadening of the phase diagram^[1,280] which will be true if the preference of the different lipid phases to the different adhesion regions is stronger than the miscibility of the lipids, leading to the already described effect of lipid sorting. To prove this hypothesis an extreme point of phase separation is used for PSMs and compared to reported lipid mixtures with homogeneous membrane adhesion. Membranes with lipid compositions of DOPC/ SM_{porc} /Chol with high Cholesterol content of 50 mol% were used which showed a clear phase separation as seen in figure 5.15. The same lipid composition was demonstrated in a study of Petruzielo *et al.* using fluorescence resonance energy transfer (FRET) to investigate phase separation in multi-lamellar vesicles (MLVs).^[281] Phase separation

was observed up to 40 mol % Chol,^[281] at higher Chol content no phase separation is reported. This indicates a broadening for this specific membrane mixture when different membrane areas with adhesional energy are present. Another phase diagram, measured with vesicles, was done by Carravilla *et al.*^[282] They analyzed the lipid composition by changing the SM from SM_{porc} to SM_{egg} and visualized the phase separation by Laudan in GUVs. They saw no phase separation with Chol contents higher than 40 mol %.^[282] Aufderhorst-Roberts *et al.* measured phase separation in the SSM using AFM to measure topographic images. In their work, it is reported that DOPC/SM_{egg}/Chol membranes on mica showed phase separation up to 40 mol % Chol at 25 °C.^[283] In all phase diagrams reported for homogeneous membrane adhesion, the phase-separated membrane was found up to 40 mol % of Chol content but not for higher Chol contents. In the phase diagram of the whole PSMs, the phase separation was visible also at Chol contents of 50 mol %. This verifies the theoretical first hypothesis, namely that areas with differing adhesional energies lead to a broadening of the phase separation region in the phase diagram.

The second hypothesis from Lipowsky *et al.* is that a phase diagram of a lipid mixture with different membrane adhesion areas shows the same maximal transition temperature as a phase diagram of the same lipid mixture prepared with a homogeneous membrane adhesion.^[1,280] It is expected that the lipid mixture in the PSM can be sorted into two lipid compositions, one with high membrane adhesion in the s-PSM and one with no surface interaction in the f-PSM. The lipid composition in each of the both regions can be at different positions of the phase diagram, since the phase diagram describes the correct phase distribution behavior of f-PSM as well as s-PSM. If this is true, the maximum transition temperature should not change from each region individually and from the whole system compared to phase diagrams recorded for "classic" systems like SSMs or vesicles. Within this thesis, this statement cannot be verified in general, because only one line of a ternary phase diagram was measured. Still, it is possible to falsify this hypothesis. If in this thesis a phase transition temperature was measured, which is higher than a phase transition temperature in a phase diagram with homogeneous adhered membrane from a comparable lipid mixture, the statement would be rejected. The measurements of the transition temperatures of PSMs at the line DOPC/SM_{porc}/Chol (1:1:x) had a maximum transition temperature of 47.5 °C. Many phase diagrams with a ternary lipid mixture were measured at one specific temperature.^[201] The phase diagrams for DOPC/SMC_{16:0}/Chol show a maximum T_M of around 50 °C.^[99] Pokorny *et al.* found phase separation for the lipid mixture POPC/SM_{porc}/Chol still at 46 °C.^[273] Since in the literature for comparable lipid composition higher transition temperatures as on

the PSMs are reported, the second statement from Lipowsky *et al.* is not rejected for this specific line in the ternary phase diagram but cannot be accepted in general.^[1,280]

The last hypothesis by Lipowsky *et al.* describes competing process based on the local lipid composition concerning exchange of lipid material and phase separation. Since s-PSM and f-PSM are connected and able to exchange lipid material, the process of phase separation is not only dependent on temperature and overall membrane composition, but also on the local lipid composition which is prone to change upon lipid material exchange. The process of phase separation in either f-PSM or s-PSM is in competition with the process of exchanging local lipid compositions. Typically, the lipid composition would change before phase separation happens either in f-PSM or s-PSM. At a certain point, the energy cost of changing the lipid composition from the different adhesion regions is higher compared to one region, with the same membrane adhesion, undergoing a phase separation. This means that due to energetic reasons, phase separation is only possible in one of the regions and never in both at the same time. Phase separation was never observed in both regions (f-PSM and s-PSM) at the same time for the phase diagram measurements. Phase separation was only observed within the f-PSM in measurements with a Chol concentration of ≤ 18 mol % (figure 5.12 and 5.13 at 40 °C). In contrast to this, the visualization of phase separation in both regions was possible if phase-separated GUVs were spread at room temperature (figure 5.4 and 5.5). This is not in contradiction to the hypothesis, since the membranes were kinetically entrapped and not in the thermodynamic equilibrium. This was proven, since heating the membranes above the transition temperature and cooling down lead to membranes without phase separation in both regions. The theory of Lipowsky *et al.* described only membranes in the thermodynamic equilibrium and not in a kinetic entrapment.^[1,280] The theory of Lipowsky *et al.* is not falsified in general but verified for the lipid compositions used within this work.

s-PSM are composed of l_d phase and f-PSM of l_o/l_β phases at all different measured Chol concentrations. From the theory of Lipowsky *et al.*^[1,280] and these findings, it is concluded that the adhesion energy to the SiO_x functionalized substrates is higher for the l_d phase than for the l_o phase. This is in agreement with the measurements of the membrane tensions for the different phases. The results of membrane tension measurements on SiO_x functionalized substrates suggest that the adhesion energy for the l_d phase is higher compared to the adhesion energy for the l_o phase (chapter 5.1.2, page 75). The reason is that the membrane bending stiffness of the l_d phase is lower compared to the l_o phase.^[243-254] Therefore, more surface on the rough SiO_x functionalized substrate, for the membrane adhesion is present for the l_d phase.

5.3. Conclusion of pore-spanning membranes (PSMs)

As found in cellular systems, where the membrane is partly adhered and partly free standing, the PSM models allow to systematically study the influence of adhesion in complex membrane systems. The interaction of membrane and substrate in the s-PSM region influences the membrane properties in the f-PSM region. With higher adhesion in the s-PSM region, the diffusion coefficient in the s-PSM slowed down and the diffusion coefficient in the f-PSM increased as determined by iSCAT measurements. The adhesion of the membrane to the substrate in the s-PSM is the origin of the membrane tension in the f-PSM. The functionalization with gold and different mercaptoalcohols resulted in the tension regime of 0.6 to 3.2 mN m⁻¹. While p-Si₃N₄ functionalized surfaces showed a tension of 1.6 ± 0.5 mN m⁻¹, a tension of 10.5 ± 4.3 mN m⁻¹ was found when SiO_x functionalized substrates were used. The SiO_x surfaces allow the detection of fluorescence signals in f-PSMs as well as s-PSMs and were used to study phase-separated PSMs in dependency of the two regions. The *l_d* and *l_o* phases can be distinguished with a factor of 20 by FCS measurements in the f-PSM.

STxB Gb₃ binding was not effected by the high membrane tension or the high substrate adhesion of the membrane to the SiO_x functionalized substrate, because it binds to the natural *l_o* phase (figure 5.5).

To investigate the influence of the different adhesion properties on the phase-separated membranes, a phase diagram was measured by increasing the Chol content in a membrane with an equimolar of DOPC and SM_{porc}. Two different fluorescent phase markers were used to determine the lipid phases in the f-PSMs and s-PSMs for different temperatures and Chol contents. As it was shown for a low Chol content (≤10 mol %), the phase separation takes place between the *l_β* phase in the f-PSM and the *l_d* phase in the s-PSM at low temperatures (<30 °C) to a homogeneous *l_d* phase in the whole PSM at high temperatures (>50 °C). Another phase separation takes place at a high Chol content (≥9 mol %) from a phase-separated PSM with the *l_o* phase in the f-PSM and the *l_d* phase in the s-PSM to a homogeneous *l_d* phase in the whole PSM. Phase diagrams with a homogeneous adhesion to the membrane showed no phase-separated membrane with 50 mol % Chol. In contrast to this finding, the phase diagram of the PSM showed phase-separated membranes at that Chol content. This confirms the broadening effect of the phase-separated region in the phase diagram from the theoretical work of Lipowsky *et al.*^[1,280]

The cell membrane can be described with the lipid raft model and this model includes a clustering of the membrane. The results of the phase-separated PSMs

5. Pore-spanning membranes (PSMs)

gave a hint that not only the lipid-protein mixture has an effect on the membrane ordering, but also that the different pinning points affect the membrane ordering, membrane dynamic and lipid-protein distribution.

6. Conclusion

Enterohemorrhagic *Escherichia coli* (EHEC) is a bacterial strain, causing diseases like diarrhea, bloody diarrhea, hemorrhagic colitis, haemolytic uraemic syndrome and damage of the central nervous system. All these diseases are triggered by shiga toxin (STx) which is a protein produced by EHEC. STx is known to bind to globotriaosyl ceramide (Gb₃) in the cellular membranes. After binding, STx enters the cell where it inhibits the intracellular protein biosynthesis. The B-subunit of STx (STxB) is responsible for binding while the A-subunit of STx (STxA) inflicts the toxic effect. The STxB is known to bind to the more ordered membrane structure at the cells, but the distribution of Gb₃ before the STxB binding is not known which was investigated in this work. Biomimetic model membranes showing liquid ordered (l_o)/liquid disordered (l_d) phase separation were employed to study Gb₃ phase performance before and after STxB binding.

To quantify the partitioning of Gb₃ in coexisting l_o/l_d phases, fluorescently fatty acid labeled Gb₃s were synthesized, containing pentaene or hexaene moieties that allowed localization of Gb₃ molecules in l_o/l_d membranes by measure of fluorescence microscopy. These Gb₃s were preferentially localized in the l_d phase. STxB binding to these Gb₃-species also takes place in the l_d phase which contradicts the binding behavior of the natural Gb₃. To contain a natural phase preference of Gb₃, a second labeling strategy was employed by connecting a BODIPY fluorophore to the head group of the Gb₃ using polyethylene glycol (PEG) linker. The synthesized head group labeled Gb₃s allowed to address the question how the structure of the fatty acid of a Gb₃ influences its distribution in l_o/l_d phase-separated membranes. The results clearly demonstrate that the unsaturated fatty acid significantly shifts the Gb₃ molecules from the l_o phase to the l_d phase. Which can be explained because the l_o phase is enriched in saturated lipids and the l_d phase enriched unsaturated lipids. An α -hydroxylation at the fatty acid showed no effect on the distribution of Gb₃. Furthermore, the fatty acids of sphingomyelin (SM) impact the distribution of the Gb₃ due to interdigitation. It is conceivable that the overall recruitment of lipids and the STx induced membrane reorganization eventually leads to invagination

of the protein into the host cells and that this can be an influence of the fatty acid composition of Gb₃.

The cell membrane has different interactions like cell-cell junctions, focal adhesions or the cytoskeleton. These adhesional points might influence local lipid compartmentation and therefore could have an impact for the lipid raft hypothesis and also on the Gb₃ distribution in the cellular membrane. A model membrane system with different adhesional energies to the membrane is the pore-spanning membrane (PSM). While established PSM systems are based on gold thiol functionalization. The gold prohibit fluorescence readout in the solid supported PSM (s-PSM). Within this thesis, a silicon oxide (SiO_x) functionalization was established and characterized to enable phase separation on freestanding PSM (f-PSM) and s-PSM.

To investigate the influence of different adhesional properties on phase-separated membranes, a phase diagram was obtained by increasing the cholesterol (Chol) content in an equimolar membrane composed of DOPC and SM_{porc}. The existence of two different adhesion areas (s-PSM and f-PSM) had a dramatic effect on the phase diagram. The region of the phase-separated membrane was broadened in comparison to phase diagrams reported from systems with homogeneous membrane adhesion. Interestingly, the l_d phase was only observed in the s-PSM, while the more ordered membrane was found in the f-PSM. The adhesion of the l_d phase to the rough surface can be favored, as the lower bending energy allows for the l_d phase to get higher adhesion energy.

The results obtained in this thesis suggest that not only the lipid-protein mixture has an effect on the membrane reorganization to nano domains, but also the adhesional points affected the membrane reorganization, membrane dynamic and lipid-protein distribution. This can also influence the phase distribution of the Gb₃ which can be analyzed in further steps using PSMs. This would provide a better biomimetic model compared to giant unilamellar vesicles (GUVs).

7. References

1. Lipowsky R., Rouhiparkouhi T., Discher D. E. & Weikl T. R. Domain formation in cholesterol–phospholipid membranes exposed to adhesive surfaces or environments. *Soft Matter* **9**, 8438–8453 (2013).
2. Scherer W. F., Syverton J. T. & Gey G. O. Studies on the propagation in vitro of poliomyelitis viruses: IV. Viral multiplication in a stable strain of human malignant epithelial cells (strain HeLa) derived from an epidermoid carcinoma of the cervix. *J. Exp. Med.* **97**, 695–710 (1953).
3. Michino H., Araki K., Minami S., Takaya S., Sakai N., Miyazaki M., Ono A. & Yanagawa H. Massive outbreak of Escherichia coli O157: H7 infection in schoolchildren in Sakai City, Japan, associated with consumption of white radish sprouts. *Am. J. Epidemiol.* **150**, 787–796 (1999).
4. Baljer G. & Wieler L. Enterohaemorrhagic E. coli (EHEC)-recent information on a new medically important zoonotic agent. *Lohman Information* **22**, 21–6 (1999).
5. Bettelheim K. A., Whipp M., Djordjevic S. P. & Ramachandran V. First isolation outside Europe of sorbitol-fermenting verocytotoxigenic Escherichia coli (VTEC) belonging to O group O157. *J. Med. Microbiol.* **51**, 713 (2002).
6. Croxen M. A., Law R. J., Scholz R., Keeney K. M., Wlodarska M. & Finlay B. B. Recent advances in understanding enteric pathogenic Escherichia coli. *Clin. Microbiol. Rev.* **26**, 822–880 (2013).
7. Konowalchuk J., Speirs J. & Stavric S. Vero response to a cytotoxin of Escherichia coli. *Infect. Immun.* **18**, 775–779 (1977).
8. Riley L. W., Remis R. S., Helgerson S. D., McGee H. B., Wells J. G., Davis B. R., Hebert R. J., Olcott E. S., Johnson L. M., Hargrett N. T., *et al.* Hemorrhagic colitis associated with a rare Escherichia coli serotype. *New Engl. J. Med.* **308**, 681–685 (1983).

7. References

9. Grant J., Wendelboe A. M., Wendel A., Jepson B., Torres P., Smelser C. & Rolfs R. T. Spinach-associated *Escherichia coli* O157: H7 outbreak, Utah and New Mexico, 2006. *Emerg. Infect. Dis.* **14**, 1633 (2008).
10. Sartz L., De Jong B., Hjertqvist M., Plym-Forsell L., Alsterlund R., Löfdahl S., Osterman B., Ståhl A., Eriksson E., Hansson H.-B., *et al.* An outbreak of *Escherichia coli* O157: H7 infection in southern Sweden associated with consumption of fermented sausage; aspects of sausage production that increase the risk of contamination. *Epidemiol. Infect.* **136**, 370–380 (2008).
11. Schimmer B., Nygard K., Eriksen H.-M., Lassen J., Lindstedt B., Brandal L. T., Kapperud G. & Aavitsland P. Outbreak of haemolytic uraemic syndrome in Norway caused by stx 2-positive *Escherichia coli* O103: H25 traced to cured mutton sausages. *BMC Infect. Dis.* **8**, 41 (2008).
12. Ammon A., Petersen L. R. & Karch H. A Large Outbreak of Hemolytic Uremic Syndrome Caused by an Unusual Sorbitol-Fermenting Strain of *Escherichia coli* O157: H-. *J. Infect. Dis.* **179**, 1274–1277 (1999).
13. Buchholz U., Bernard H., Werber D., Böhmer M. M., Remschmidt C., Wilking H., Deleré Y., an der Heiden M., Adlhoch C., Dreesman J., *et al.* German outbreak of *Escherichia coli* O104: H4 associated with sprouts. *New Engl. J. Med.* **365**, 1763–1770 (2011).
14. Bielaszewska M., Mellmann A., Zhang W., Köck R., Fruth A., Bauwens A., Peters G. & Karch H. Characterisation of the *Escherichia coli* strain associated with an outbreak of haemolytic uraemic syndrome in Germany, 2011: a microbiological study. *Lancet Infect. Dis.* **11**, 671–676 (2011).
15. Karch H. EHEC O104: H4 und die Folgen. *Biospektrum* **17**, 616–620 (2011).
16. Appel B., Böhl G., Greiner M., Lahrssen-Wiederholt M. & Hensel A. EHEC outbreak 2011. Investigation of the outbreak along the food chain. *Berlin: Bundesinstitut für Risikobewertung* (2012).
17. Burger R. in *Improving Food Safety Through a One Health Approach: Workshop Summary, 2012* 115–130 (Robert Koch-Institut, 2012).
18. Frank C., Faber M., Askar M., Bernard H., Fruth A., Gilsdorf A., Höhle M., Karch H., Krause G., Prager R., *et al.* Large and ongoing outbreak of haemolytic uraemic syndrome, Germany, May 2011. *Eurosurveillance* **16**, 19878 (2011).
19. Alpers K., Stark K., Hellenbrand W. & Ammon A. Zoonotische Infektionen beim Menschen. *Bundesgesundheitsbla.* **47**, 622–632 (2004).

-
20. Robert Koch-Institut. *SurvStat@RKI 2.0* German. <https://survstat.rki.de> (July 30, 2019).
 21. Villysson A., Tontanahal A. & Karpman D. Microvesicle Involvement in Shiga Toxin-Associated Infection. *Toxins* **9**, 376 (2017).
 22. Onyenweaku Florence C., Ifeanyi O. E. & Nwandikor Uzoije U. A Review on Hemolytic Uremic Syndrome. *Int. J. Curr. Res. Med. Sci.* **4**, 80–92 (2018).
 23. Tarr P. I., Gordon C. A. & Chandler W. L. Shiga-toxin-producing *Escherichia coli* and haemolytic uraemic syndrome. *Lancet* **365**, 1073–1086 (2005).
 24. Spinale J. M., Ruebner R. L., Copelovitch L. & Kaplan B. S. Long-term outcomes of Shiga toxin hemolytic uremic syndrome. *Pediatr. Nephrol.* **28**, 2097–2105 (2013).
 25. Melton-Celsa A. R. Shiga toxin (Stx) classification, structure, and function. *Microbiol. Spectrum* **2** (2014).
 26. Tesh V. L., Burris J., Owens J., Gordon V., Wadolkowski E., O’Brien A. & Samuel J. Comparison of the relative toxicities of Shiga-like toxins type I and type II for mice. *Infect. Immun.* **61**, 3392–3402 (1993).
 27. Wadolkowski E., Sung L., Burris J., Samuel J. & O’Brien A. Acute renal tubular necrosis and death of mice orally infected with *Escherichia coli* strains that produce Shiga-like toxin type II. *Infect. Immun.* **58**, 3959–3965 (1990).
 28. O’Brien A., Lively T., Chen M., Rothman S. & Formal S. *Escherichia coli* 0157:H7 strains associated with haemorrhagic colitis in the United States produce a *Shigella dysenteriae* 1 (Shiga) like cytotoxin. *Lancet* **321**, 702 (1983).
 29. Manitz J., Kneib T., Schlather M., Helbing D. & Brockmann D. Origin detection during food-borne disease outbreaks—a case study of the 2011 ehec/hus outbreak in Germany. *PLoS Curr.* **6** (2014).
 30. Trachtman H., Austin C., Lewinski M. & Stahl R. A. Renal and neurological involvement in typical Shiga toxin-associated HUS. *Nat. Rev. Nephrol.* **8**, 658 (2012).
 31. Karch H., Tarr P. I. & Bielaszewska M. Enterohaemorrhagic *Escherichia coli* in human medicine. *Int. J. Med. Microbiol.* **295**, 405–418 (2005).
 32. Karpman D., Loos S., Tati R. & Arvidsson I. Haemolytic uraemic syndrome. *J. Intern. Med.* **281**, 123–148 (2017).
-

7. References

33. Exeni R. A., Fernandez-Brando R. J., Santiago A. P., Fiorentino G. A., Exeni A. M., Ramos M. V. & Palermo M. S. Pathogenic role of inflammatory response during Shiga toxin-associated hemolytic uremic syndrome (HUS). *Pediatr. Nephrol.* 1–15 (2018).
34. Obata F., Tohyama K., Bonev A. D., Kolling G. L., Keepers T. R., Gross L. K., Nelson M. T., Sato S. & Obrig T. G. Shiga toxin 2 affects the central nervous system through receptor globotriaosylceramide localized to neurons. *J. Infect. Dis.* **198**, 1398–1406 (2008).
35. Friedrich A. W., Bielaszewska M., Zhang W.-L., Pulz M., Kuczius T., Ammon A. & Karch H. Escherichia coli harboring Shiga toxin 2 gene variants: frequency and association with clinical symptoms. *J. Infect. Dis.* **185**, 74–84 (2002).
36. Fuller C. A., Pellino C. A., Flagler M. J., Strasser J. E. & Weiss A. A. Shiga toxin subtypes display dramatic differences in potency. *Infect. Immun.* **79**, 1329–1337 (2011).
37. Shiga K. Studien über die epidemische Dysenterie in Japan, unter besonderer Berücksichtigung des Bacillus dysenteriae (Schluss aus No. 44.) *Deut. Med. Wochenschr.* **27**, 783–786 (1901).
38. Orihuel A., Terán L., Renaut J., Planchon S., Valacco M. P., Masias E., Minahk C., Vignolo G., Moreno S., De Almeida A. M., *et al.* Physiological and proteomic response of Escherichia coli O157: H7 to a bioprotective lactic acid bacterium in a meat environment. *Food Res. Int.* 108622 (2019).
39. Zoja C., Buelli S. & Morigi M. Shiga toxin-associated hemolytic uremic syndrome: pathophysiology of endothelial dysfunction. *Pediatr. Nephrol.* **25**, 2231–2240 (2010).
40. Lee M.-S. & Tesh V. L. Roles of Shiga Toxins in Immunopathology. *Toxins* **11**, 212 (2019).
41. Mahfoud R., Manis A. & Lingwood C. A. Fatty acid-dependent globotriaosyl ceramide receptor function in detergent resistant model membranes. *J. Lipid Res.* **50**, 1744–1755 (2009).
42. Mahfoud R., Manis A., Binnington B., Ackerley C. & Lingwood C. A. A major fraction of glycosphingolipids in model and cellular cholesterol-containing membranes is undetectable by their binding proteins. *J. Biol. Chem.* **285**, 36049–36059 (2010).

-
43. Lindberg A., Brown J., Strömberg N., Westling-Ryd M., Schultz J. & Karlsson K. Identification of the carbohydrate receptor for Shiga toxin produced by *Shigella dysenteriae* type 1. *J. Biol. Chem.* **262**, 1779–1785 (1987).
 44. Ramegowda B., Samuel J. E. & Tesh V. L. Interaction of Shiga toxins with human brain microvascular endothelial cells: cytokines as sensitizing agents. *J. Infect. Dis.* **180**, 1205–1213 (1999).
 45. Legros N., Pohlentz G., Runde J., Dusny S., Humpf H.-U., Karch H. & Müthing J. Colocalization of receptors for Shiga toxins with lipid rafts in primary human renal glomerular endothelial cells and influence of D-PDMP on synthesis and distribution of glycosphingolipid receptors. *Glycobiology* **27**, 947–965 (2017).
 46. Legros N., Dusny S., Humpf H.-U., Pohlentz G., Karch H. & Müthing J. Shiga toxin glycosphingolipid receptors and their lipid membrane ensemble in primary human blood–brain barrier endothelial cells. *Glycobiology* **27**, 99–109 (2016).
 47. Legros N., Pohlentz G., Steil D. & Müthing J. Shiga toxin-glycosphingolipid interaction: Status quo of research with focus on primary human brain and kidney endothelial cells. *Int. J. Med. Microbiol.* **308**, 1073–1084 (2018).
 48. Steil D., Bonse R., Meisen I., Pohlentz G., Vallejo G., Karch H. & Müthing J. A topographical atlas of Shiga toxin 2e receptor distribution in the tissues of weaned piglets. *Toxins* **8**, 357 (2016).
 49. Kale R. R., McGannon C. M., Fuller-Schaefer C., Hatch D. M., Flagler M. J., Gamage S. D., Weiss A. A. & Iyer S. S. Differentiation between structurally homologous Shiga 1 and Shiga 2 toxins by using synthetic glycoconjugates. *Angew. Chem. Int. Ed.* **47**, 1265–1268 (2008).
 50. Ling H., Boodhoo A., Hazes B., Cummings M. D., Armstrong G. D., Brunton J. L. & Read R. J. Structure of the shiga-like toxin I B-pentamer complexed with an analogue of its receptor Gb₃. *Biochemistry* **37**, 1777–1788 (1998).
 51. Jacobson J. M., Yin J., Kitov P. I., Mulvey G., Griener T. P., James M. N., Armstrong G. & Bundle D. R. The crystal structure of Shiga toxin type 2 with bound disaccharide guides the design of a heterobifunctional toxin inhibitor. *J. Biol. Chem.* **289**, 885–894 (2014).
 52. Mobassaleh M., Donohue-Rolfe A., Jacewicz M., Grand R. J. & Keusch G. T. Pathogenesis of shigella diarrhea: evidence for a developmentally regulated glycolipid receptor for shigella toxin involved in the fluid secretory response of rabbit small intestine. *J. Infect. Dis.* **157**, 1023–1031 (1988).
-

53. Reisbig R., Olsnes S. & Eiklid K. The cytotoxic activity of Shigella toxin. Evidence for catalytic inactivation of the 60 S ribosomal subunit. *J. Biol. Chem.* **256**, 8739–8744 (1981).
54. Windschiegl B., Orth A., Romer W., Berland L., Stechmann B., Bassereau P., Johannes L. & Steinem C. Lipid reorganization induced by Shiga toxin clustering on planar membranes. *PLoS One* **4**, e6238 (2009).
55. Safouane M., Berland L., Callan-Jones A., Sorre B., Römer W., Johannes L., Toombes G. E. & Bassereau P. Lipid cosorting mediated by shiga toxin induced tubulation. *Traffic* **11**, 1519–1529 (2010).
56. Pezeshkian W., Hansen A. G., Johannes L., Khandelia H., Shillcock J., Kumar P. S. & Ipsen J. Membrane invagination induced by Shiga toxin B-subunit: from molecular structure to tube formation. *Soft Matter* **12**, 5164–5171 (2016).
57. Römer W., Berland L., Chambon V., Gaus K., Windschiegl B., Tenza D., Aly M. R., Fraissier V., Florent J.-C., Perrais D., Lamaze C., Raposo G., Steinem C., Sens P., Bassereau P. & Johannes L. Shiga toxin induces tubular membrane invaginations for its uptake into cells. *Nature* **450**, 670–675 (2007).
58. Sandvig K., Olsnes S., Brown J. E., Petersen O. W. & van Deurs B. Endocytosis from coated pits of Shiga toxin: a glycolipid-binding protein from Shigella dysenteriae 1. *J. Cell Biol.* **108**, 1331–1343 (1989).
59. Sandvig K. & Van Deurs B. Endocytosis, intracellular transport, and cytotoxic action of Shiga toxin and ricin. *Physiol. Rev.* **76**, 949–966 (1996).
60. Lauvrak S. U., Torgersen M. L. & Sandvig K. Efficient endosome-to-Golgi transport of Shiga toxin is dependent on dynamin and clathrin. *J. Cell Sci.* **117**, 2321–2331 (2004).
61. Saint-Pol A., Yélamos B., Amessou M., Mills I. G., Dugast M., Tenza D., Schu P., Antony C., McMahon H. T., Lamaze C., *et al.* Clathrin adaptor epsinR is required for retrograde sorting on early endosomal membranes. *Dev. Cell* **6**, 525–538 (2004).
62. Johannes L. & Römer W. Shiga toxins from cell biology to biomedical applications. *Nat. Rev. Microbiol.* **8**, 105–116 (2010).
63. Spooner R. A. & Lord J. M. in *Ricin and Shiga Toxins* 19–40 (Springer, 2011).
64. Johannes L. Shiga Toxin-A Model for Glycolipid-Dependent and Lectin-Driven Endocytosis. *Toxins* **9**, 340 (2017).

-
65. Kovbasnjuk O., Mourtažina R., Baibakov B., Wang T., Elowsky C., Choti M. A., Kane A. & Donowitz M. The glycosphingolipid globotriaosylceramide in the metastatic transformation of colon cancer. *Proc. Natl. Acad. Sci. U.S.A.* **102**, 19087–19092 (2005).
 66. Amessou M., Carrez D., Patin D., Sarr M., Grierson D. S., Croisy A., Tedesco A. C., Maillard P. & Johannes L. Retrograde delivery of photosensitizer (TPPp-O- β -GluOH) 3 selectively potentiates its photodynamic activity. *Bioconjugate Chem.* **19**, 532–538 (2008).
 67. Distler U., Souady J., Hülsewig M., Drmić-Hofman I., Haier J., Friedrich A. W., Karch H., Senninger N., Dreisewerd K., Berkenkamp S., *et al.* Shiga toxin receptor Gb₃Cer/CD77: tumor-association and promising therapeutic target in pancreas and colon cancer. *PLoS One* **4**, e6813 (2009).
 68. Engedal N., Skotland T., Torgersen M. L. & Sandvig K. Shiga toxin and its use in targeted cancer therapy and imaging. *Microb. Biotechnol.* **4**, 32–46 (2011).
 69. Luginbuehl V., Meier N., Kovar K. & Rohrer J. Intracellular drug delivery: Potential usefulness of engineered Shiga toxin subunit B for targeted cancer therapy. *Biotechnol. Adv.* **36**, 613–623 (2018).
 70. LaCasse E., Bray M., Patterson B., Lim W.-M., Perampalam S., Radvanyi L., Keating A., Stewart A., Buckstein R., Sandhu J., Miller N., Banerjee D., Singh D., Belch A., Pilarski L. & Gariépy J. Shiga-like toxin-1 receptor on human breast cancer, lymphoma, and myeloma and absence from CD34+ hematopoietic stem cells: implications for ex vivo tumor purging and autologous stem cell transplantation. *Blood* **94**, 2901–2910 (1999).
 71. Tarragó-Trani M. T. & Storrie B. Alternate routes for drug delivery to the cell interior: pathways to the Golgi apparatus and endoplasmic reticulum. *Adv. Drug Deliver. Rev.* **59**, 782–797 (2007).
 72. Batisse C., Dransart E., Sarkouh R. A., Brulle L., Bai S.-K., Godefroy S., Johannes L. & Schmidt F. A new delivery system for auristatin in STxB-drug conjugate therapy. *Eur. J. Med. Chem.* **95**, 483–491 (2015).
 73. Maak M., Nitsche U., Keller L., Wolf P., Sarr M., Thiebaud M., Rosenberg R., Langer R., Kleeff J., Friess H., *et al.* Tumor-specific targeting of pancreatic cancer with Shiga toxin B-subunit. *Mol. Cancer Ther.* **10**, 1918–1928 (2011).
 74. Tarragó-Trani M. T., Jiang S., Harich K. C. & Storrie B. Shiga-like toxin subunit B (SLTB)-enhanced delivery of chlorin e6 (Ce6) improves cell killing. *Photochem. Photobiol.* **82**, 527–537 (2006).
-

7. References

75. Ryou J.-H., Sohn Y.-K., Hwang D.-E. & Kim H.-S. Shiga-like toxin-based high-efficiency and receptor-specific intracellular delivery system for a protein. *Biochem. Biophys. Res. Commun.* **464**, 1282–1289 (2015).
76. Bouter A., Delord B., Dransart E., Poirier C., Johannes L. & Van Effenterre D. Intracellular trafficking of Shiga-toxin-B-subunit-functionalized spherulites. *Biol. Cell* **100**, 717–728 (2008).
77. Singer S. J. & Nicolson G. L. The fluid mosaic model of the structure of cell membranes. *Science* **175**, 720–731 (1972).
78. Van Meer G. & de Kroon A. I. Lipid map of the mammalian cell. *J. Cell Sci.* **124**, 5–8 (2011).
79. Harayama T. & Riezman H. Understanding the diversity of membrane lipid composition. *Nat. Rev. Mol. Cell Biol.* **19**, 281 (2018).
80. Simons K. & Ikonen E. Functional rafts in cell membranes. *Nature* **387**, 569–572 (1997).
81. Goñi F. M. “Rafts”: a nickname for putative transient nanodomains. *Chem. Phys. Lipids* **218**, 34–39 (2019).
82. Cebecauer M., Amaro M., Jurkiewicz P., Sarmiento M. J., Šachl R., Cwiklik L. & Hof M. Membrane Lipid Nanodomains. *Chem. Rev.* **118**, 11259–11297 (2018).
83. Raghunathan K. & Kenworthy A. K. Dynamic pattern generation in cell membranes: Current insights into membrane organization. *Biochim. Biophys. Acta, Biomembr.* **1860**, 2018–2031 (2018).
84. Pike L. J. Rafts defined: a report on the Keystone Symposium on Lipid Rafts and Cell Function. *J. Lipid Res.* **47**, 1597–1598 (2006).
85. Sezgin E., Levental I., Mayor S. & Eggeling C. The mystery of membrane organization: composition, regulation and roles of lipid rafts. *Nat. Rev. Mol. Cell Biol.* **18**, 361 (2017).
86. Cheng X. & Smith J. C. Biological Membrane Organization and Cellular Signaling. *Chem. Rev.* **119**, 5849–5880 (2019).
87. Liu A. P. & Fletcher D. A. Actin polymerization serves as a membrane domain switch in model lipid bilayers. *Biophys. J.* **91**, 4064–4070 (2006).
88. Marushchak D., Gretskeya N., Mikhalyov I. & Johansson L. B.-Å. Self-aggregation—an intrinsic property of GM1 in lipid bilayers. *Mol. Membr. Biol.* **24**, 102–112 (2007).

-
89. Van Zanten T. S. & Mayor S. Current approaches to studying membrane organization. *F1000Res.* **4** (2015).
 90. Brown D. A. & London E. Structure and function of sphingolipid- and cholesterol-rich membrane rafts. *J. Biol. Chem.* **275**, 17221–17224 (2000).
 91. Rao M. & Mayor S. Use of Förster’s resonance energy transfer microscopy to study lipid rafts. *Biochim. Biophys. Acta, Mol. Cell Res.* **1746**, 221–233 (2005).
 92. Loura L. M., Fedorov A. & Prieto M. Fluid–fluid membrane microheterogeneity: a fluorescence resonance energy transfer study. *Biophys. J.* **80**, 776–788 (2001).
 93. Krieger J. W., Singh A. P., Bag N., Garbe C. S., Saunders T. E., Langowski J. & Wohland T. Imaging fluorescence (cross-) correlation spectroscopy in live cells and organisms. *Nat. Protoc.* **10**, 1948 (2015).
 94. Bag N., Ng X. W., Sankaran J. & Wohland T. Spatiotemporal mapping of diffusion dynamics and organization in plasma membranes. *Method. Appl. Fluoresc.* **4**, 034003 (2016).
 95. Nickels J. D., Chatterjee S., Stanley C. B., Qian S., Cheng X., Myles D. A., Standaert R. F., Elkins J. G. & Katsaras J. The in vivo structure of biological membranes and evidence for lipid domains. *PLoS Biol.* **15**, e2002214 (2017).
 96. Bernardino de la Serna J., Schütz G. J., Eggeling C. & Cebecauer M. There is no simple model of the plasma membrane organization. *Front. Cell Dev. Biol.* **4**, 106 (2016).
 97. Feigenson G. W. Phase diagrams and lipid domains in multicomponent lipid bilayer mixtures. *Biochim. Biophys. Acta, Biomembr.* **1788**, 47–52 (2009).
 98. London E. How principles of domain formation in model membranes may explain ambiguities concerning lipid raft formation in cells. *Biochim. Biophys. Acta, Mol. Cell Res.* **1746**, 203–220 (2005).
 99. Veatch S. L. & Keller S. L. Miscibility phase diagrams of giant vesicles containing sphingomyelin. *Phys. Rev. Lett.* **94**, 148101 (2005).
 100. Dimova R. Giant vesicles and their use in assays for assessing membrane phase state, curvature, mechanics, and electrical properties. *Annu. Rev. Biophys.* **48**, 93–119 (2019).
 101. Aoki P., Schroder A., Constantino C. & Marques C. Bioadhesive giant vesicles for monitoring hydroperoxidation in lipid membranes. *Soft Matter* **11**, 5995–5998 (2015).
-

7. References

102. Janshoff A. & Steinem C. Mechanics of lipid bilayers: What do we learn from pore-spanning membranes? *Biochim. Biophys. Acta, Mol. Cell Res.* **1853**, 2977–2983 (2015).
103. Chan Y.-H. M. & Boxer S. G. Model membrane systems and their applications. *Curr. Opin. Chem. Biol.* **11**, 581–587 (2007).
104. Kubsch B., Robinson T., Lipowsky R. & Dimova R. Solution asymmetry and salt expand fluid-fluid coexistence regions of charged membranes. *Biophys. J.* **110**, 2581–2584 (2016).
105. Kubsch B., Robinson T., Steinkühler J. & Dimova R. Phase Behavior of Charged Vesicles Under Symmetric and Asymmetric Solution Conditions Monitored with Fluorescence Microscopy. *J. Vis. Exp.* **128**, e56034 (2017).
106. Diaz A. J., Albertorio F., Daniel S. & Cremer P. S. Double cushions preserve transmembrane protein mobility in supported bilayer systems. *Langmuir* **24**, 6820–6826 (2008).
107. Tanaka M. & Sackmann E. Polymer-supported membranes as models of the cell surface. *Nature* **437**, 656 (2005).
108. Sheetz M. P. Cell control by membrane–cytoskeleton adhesion. *Nat. Rev. Mol. Cell Biol.* **2**, 392–396 (2001).
109. Nambiar R., McConnell R. E. & Tyska M. J. Control of cell membrane tension by myosin-I. *Proc. Natl. Acad. Sci. U.S.A.* **106**, 11972–11977 (2009).
110. Gleisner M., Kroppen B., Fricke C., Teske N., Kliesch T.-T., Janshoff A., Meinecke M. & Steinem C. Epsin N-terminal homology domain (ENTH) activity as a function of membrane tension. *J. Biol. Chem.* **291**, 19953–19961 (2016).
111. Van Dijck P., De Kruijff B., Van Deenen L., De Gier J. & Demel R. The preference of cholesterol for phosphatidylcholine in mixed phosphatidylcholine-phosphatidylethanolamine bilayers. *Biochim. Biophys. Acta, Biomembr.* **455**, 576–587 (1976).
112. Ulrich A. S., Sami M. & Watts A. Hydration of DOPC bilayers by differential scanning calorimetry. *Biochim. Biophys. Acta, Biomembr.* **1191**, 225–230 (1994).

-
113. Lewis R. N., Sykes B. D. & McElhaney R. N. Thermotropic phase behavior of model membranes composed of phosphatidylcholines containing cis-mono-unsaturated acyl chain homologs of oleic acid: differential scanning calorimetric and phosphorus-31 NMR spectroscopic studies. *Biochemistry* **27**, 880–887 (1988).
 114. Koynova R. & Caffrey M. Phases and phase transitions of the phosphatidylcholines. *Biochim. Biophys. Acta, Rev. Biomembr.* **1376**, 91–145 (1998).
 115. Lynch D. V. & Steponkus P. L. Lyotropic phase behavior of unsaturated phosphatidylcholine species: relevance to the mechanism of plasma membrane destabilization and freezing injury. *Biochim. Biophys. Acta, Biomembr.* **984**, 267–272 (1989).
 116. Coolbear K., Berde C. & Keough K. Gel to liquid-crystalline phase transitions of aqueous dispersions of polyunsaturated mixed-acid phosphatidylcholines. *Biochemistry* **22**, 1466–1473 (1983).
 117. Barton P. G. & Gunstone F. Hydrocarbon chain packing and molecular motion in phospholipid bilayers formed from unsaturated lecithins. Synthesis and properties of sixteen positional isomers of 1, 2-dioctadecenoyl-sn-glycero-3-phosphorylcholine. *J. Biol. Chem.* **250**, 4470–4476 (1975).
 118. Ladbroke B. & Chapman D. Thermal analysis of lipids, proteins and biological membranes a review and summary of some recent studies. *Chem. Phys. Lipids* **3**, 304–356 (1969).
 119. Ipsen J., Mouritsen O. & Bloom M. Relationships between lipid membrane area, hydrophobic thickness, and acyl-chain orientational order. The effects of cholesterol. *Biophys. J.* **57**, 405–412 (1990).
 120. Shaw K. P., Brooks N. J., Clarke J. A., Ces O., Seddon J. M. & Law R. V. Pressure–temperature phase behaviour of natural sphingomyelin extracts. *Soft Matter* **8**, 1070–1078 (2012).
 121. Byrdwell W. C. & Perry R. H. Liquid chromatography with dual parallel mass spectrometry and ³¹P nuclear magnetic resonance spectroscopy for analysis of sphingomyelin and dihydrosphingomyelin: I. Bovine brain and chicken egg yolk. *J. Chromatogr., A* **1133**, 149–171 (2006).
 122. Koynova R. & Caffrey M. Phases and phase transitions of the sphingolipids. *Biochim. Biophys. Acta, Lipids Lipid Metab.* **1255**, 213–236 (1995).
-

7. References

123. Kawasaki Y., Nishikido H., Kuboki A., Ohira S. & Kodama M. Unilamellar vesicle-forming property of N-nervonoylsphingomyelin (C24: 1-SM) as studied by differential scanning calorimetry and negative stain electron microscopy. *Thermochim. Acta* **431**, 188–194 (2005).
124. Aoki H., Kosakabe S., Inumaru M., Kuboki A., Ohira S. & Kodama M. Structural property and function of D-erythro asymmetric chain sphingomyelins as studied by microcalorimetry and electron microscopy. *J. Therm. Anal. Calorim.* **92**, 443 (2008).
125. Kodama M. & Kawasaki Y. Structural role of mismatched C–C bonds in a series of d-erythro-sphingomyelins as studied by DSC and electron microscopy. *Chem. Phys. Lipids* **163**, 514–523 (2010).
126. Kodama M., Kawasaki Y. & Ohtaka H. The main transition enthalpy of the gel-to-liquid crystal phases for a series of asymmetric chain length D-erythro (2S, 3R) sphingomyelins. *Thermochim. Acta* **532**, 22–27 (2012).
127. Sripada P., Maulik P., Hamilton J. & Shipley G. Partial synthesis and properties of a series of N-acyl sphingomyelins. *J. Lipid Res.* **28**, 710–718 (1987).
128. Björkqvist Y. J. E., Brewer J., Bagatolli L. A., Slotte J. P. & Westerlund B. Thermotropic behavior and lateral distribution of very long chain sphingolipids. *Biochim. Biophys. Acta, Biomembr.* **1788**, 1310–1320 (2009).
129. Calhoun W. I. & Shipley G. G. Sphingomyelin-lecithin bilayers and their interaction with cholesterol. *Biochemistry* **18**, 1717–1722 (1979).
130. Barenholz Y., Suurkuusk J., Mountcastle D., Thompson T. & Biltonen R. A calorimetric study of the thermotropic behavior of aqueous dispersions of natural and synthetic sphingomyelins. *Biochemistry* **15**, 2441–2447 (1976).
131. Li X.-M., Smaby J. M., Momsen M. M., Brockman H. L. & Brown R. E. Sphingomyelin interfacial behavior: the impact of changing acyl chain composition. *Biophys. J.* **78**, 1921–1931 (2000).
132. Cohen R., Barenholz Y., Gatt S. & Dagan A. Preparation and characterization of well defined D-erythro sphingomyelins. *Chem. Phys. Lipids* **35**, 371–384 (1984).
133. Jimenez-Rojo N., Garcia-Arribas A. B., Sot J., Alonso A. & Goni F. M. Lipid bilayers containing sphingomyelins and ceramides of varying N-acyl lengths: a glimpse into sphingolipid complexity. *Biochim. Biophys. Acta, Biomembr.* **1838**, 456–464 (2014).

-
134. Jaikishan S., Björkbom A. & Slotte J. P. Sphingomyelin analogs with branched N-acyl chains: the position of branching dramatically affects acyl chain order and sterol interactions in bilayer membranes. *Biochim. Biophys. Acta, Biomembr.* **1798**, 1987–1994 (2010).
 135. Epand R. M. & Moscarello M. A. The effect of bovine myelin basic protein on the phase transition properties of sphingomyelin. *Biochim. Biophys. Acta, Biomembr.* **685**, 230–232 (1982).
 136. Ohtaka H., Kawasaki Y. & Kodama M. Phase transitions of highly asymmetric chain-length N-lignocerylsphingomyelin (C24: 0-SM) bilayer. *J. Therm. Anal. Calorim.* **113**, 1593–1602 (2013).
 137. Maulik P. R. & Shipley G. G. X-ray diffraction and calorimetric study of N-lignoceryl sphingomyelin membranes. *Biophys. J.* **69**, 1909–1916 (1995).
 138. McIntosh T. J., Simon S. A., Needham D. & Huang C. H. Structure and cohesive properties of sphingomyelin/cholesterol bilayers. *Biochemistry* **31**, 2012–2020 (1992).
 139. Baumgart T., Hunt G., Farkas E. R., Webb W. W. & Feigenson G. W. Fluorescence probe partitioning between L_o/L_d phases in lipid membranes. *Biochim. Biophys. Acta, Biomembr.* **1768**, 2182–2194 (2007).
 140. Klymchenko A. S. & Kreder R. Fluorescent probes for lipid rafts: from model membranes to living cells. *Chem. Biol.* **21**, 97–113 (2014).
 141. Patalag L. J., Sibold J., Schütte O. M., Steinem C. & Werz D. B. Gb₃ Glycosphingolipids with Fluorescent Oligoene Fatty Acids: Synthesis and Phase Behavior in Model Membranes. *ChemBioChem* **18**, 2171–2178 (2017).
 142. Sezgin E., Levental I., Grzybek M., Schwarzmann G., Mueller V., Honigsmann A., Belov V. N., Eggeling C., Coskun Ü., Simons K. & Schwille P. Partitioning, diffusion, and ligand binding of raft lipid analogs in model and cellular plasma membranes. *Biochim. Biophys. Acta, Biomembr.* **1818**, 1777–1784 (2012).
 143. Sibold J., Kettelhoit K., Vuong L., Liu F., Werz D. B. & Steinem C. Synthesis of Head Group Labeled Gb₃ Glycosphingolipids and Their Distribution in Phase-Separated Giant Unilamellar Vesicles. *Angew. Chem. Int. Ed.* **58**, 17805–17813 (2019).
 144. Johannes L., Tenza D., Antony C. & Goud B. Retrograde transport of KDEL-bearing B-fragment of Shiga toxin. *J. Biol. Chem.* **272**, 19554–19561 (1997).
-

7. References

145. Falguières T., Römer W., Amessou M., Afonso C., Wolf C., Tabet J.-C., Lamaze C. & Johannes L. Functionally different pools of Shiga toxin receptor, globotriaosyl ceramide, in HeLa cells. *FEBS J.* **273**, 5205–5218 (2006).
146. Bosse M., Sibold J., Scheidt H. A., Patalag L. J., Kettelhoit K., Ries A., Werz D. B., Steinem C. & Huster D. Shiga Toxin Binding Alters Lipid Packing and Domain Structure of Gb₃-Containing Membranes: A Solid-State NMR Study. *Phys. Chem. Chem. Phys.* **21**, 15630–15638 (2019).
147. Spindler S., Sibold J., Gholami Mahmoodabadi R., Steinem C. & Sandoghdar V. High-Speed Microscopy of Diffusion in Pore-Spanning Lipid Membranes. *Nano Lett.* **18**, 5262–5271 (2018).
148. Teske N., Sibold J., Schumacher J., Teiwes N. K., Gleisner M., Mey I. & Steinem C. Continuous Pore-Spanning Lipid Bilayers On Silicon Oxide-Coated Porous Substrates. *Langmuir* **33**, 14175–14183 (2017).
149. Klostermeier D. & Rudolph M. G. *Biophysical Chemistry* 1. Aufl. ISBN: 978-1-482-25224-8 (CRC Press, Boca Raton, Fla, 2018).
150. Benda A., Beneš M., Marecek V., Lhotský A., Hermens W. T. & Hof M. How to determine diffusion coefficients in planar phospholipid systems by confocal fluorescence correlation spectroscopy. *Langmuir* **19**, 4120–4126 (2003).
151. Lakowicz J. R. *Principles of fluorescence spectroscopy* 3rd ed. 954 pp. ISBN: 978-0-387-31278-1 (Springer, New York, 2006).
152. Geddes C. D. *Reviews in Fluorescence 2009* (Springer Science & Business Media, 2011).
153. Wohland T., Rigler R. & Vogel H. The standard deviation in fluorescence correlation spectroscopy. *Biophys. J.* **80**, 2987–2999 (2001).
154. Vestergaard C. L., Blainey P. C. & Flyvbjerg H. Optimal estimation of diffusion coefficients from single-particle trajectories. *Phys. Rev. E: Stat., Nonlinear, Soft Matter Phys.* **89**, 022726 (2014).
155. Nehls S. & Janshoff A. Elastic Properties of Pore-Spanning Apical Cell Membranes Derived from MDCK II Cells. *Biophys. J.* **113**, 1822–1830 (2017).
156. Schwamborn M., Schumacher J., Sibold J., Teiwes N. K. & Steinem C. Monitoring ATPase induced pH changes in single proteoliposomes with the lipid-coupled fluorophore Oregon Green 488. *Analyst* **142**, 2670–2677 (2017).

-
157. Fuchs G., Mobassaleh M., Donohue-Rolfe A., Montgomery R., Grand R. & Keusch G. Pathogenesis of Shigella diarrhea: rabbit intestinal cell microvillus membrane binding site for Shigella toxin. *Infect. Immun.* **53**, 372–377 (1986).
 158. Eiklid K. & Olsnes S. Interaction of Shigella shigae cytotoxin with receptors on sensitive and insensitive cells. *J. Receptor Res.* **1**, 199–213 (1980).
 159. Pina D. G. & Johannes L. Cholera and Shiga toxin B-subunits: thermodynamic and structural considerations for function and biomedical applications. *Toxicon* **45**, 389–393 (2005).
 160. Schütte O. M., Patalag L. J., Weber L. M., Ries A., Römer W., Werz D. B. & Steinem C. 2-Hydroxy Fatty Acid Enantiomers of Gb 3 Impact Shiga Toxin Binding and Membrane Organization. *Biophys. J.* **108**, 2775–2778 (2015).
 161. Head S. C., Karmali M. A. & Lingwood C. A. Preparation of VT1 and VT2 hybrid toxins from their purified dissociated subunits. Evidence for B subunit modulation of a subunit function. *J. Biol. Chem.* **266**, 3617–3621 (1991).
 162. Schütte O. M., Ries A., Orth A., Patalag L. J., Römer W., Steinem C. & Werz D. B. Influence of Gb 3 glycosphingolipids differing in their fatty acid chain on the phase behaviour of solid supported membranes: chemical syntheses and impact of Shiga toxin binding. *Chem. Sci.* **5**, 3104–3114 (2014).
 163. Castanho M., Coutinho A. & Prieto M. Absorption and fluorescence spectra of polyene antibiotics in the presence of cholesterol. *J. Biol. Chem.* **267**, 204–209 (1992).
 164. Nieves I., Artetxe I., Abad J. L., Alonso A., Busto J. V., Fajarí L., Montes L. R., Sot J., Delgado A. & Goñi F. M. Fluorescent Polyene Ceramide Analogues as Membrane Probes. *Langmuir* **31**, 2484–2492 (2015).
 165. Johnson I. D., Kang H. C. & Haugland R. P. Fluorescent membrane probes incorporating dipyrrometheneboron difluoride fluorophores. *Anal. Biochem.* **198**, 228–237 (1991).
 166. Boldyrev I. A., Zhai X., Momsen M. M., Brockman H. L., Brown R. E. & Molotkovsky J. G. New BODIPY lipid probes for fluorescence studies of membranes. *J. Lipid Res.* **48**, 1518–1532 (2007).
 167. Kaiser R. D. & London E. Determination of the depth of BODIPY probes in model membranes by parallax analysis of fluorescence quenching. *Biochim. Biophys. Acta, Biomembr.* **1375**, 13–22 (1998).
-

168. Karolin J., Johansson L. B.-A., Strandberg L. & Ny T. Fluorescence and absorption spectroscopic properties of dipyrrometheneboron difluoride (BODIPY) derivatives in liquids, lipid membranes, and proteins. *J. Am. Chem. Soc.* **116**, 7801–7806 (1994).
169. Mikhalyov I., Gretskaya N. & Johansson L. B.-Å. Fluorescent BODIPY-labelled G M1 gangliosides designed for exploring lipid membrane properties and specific membrane-target interactions. *Chem. Phys. Lipids* **159**, 38–44 (2009).
170. Ariola F. S., Li Z., Cornejo C., Bittman R. & Heikal A. A. Membrane fluidity and lipid order in ternary giant unilamellar vesicles using a new bodipy-cholesterol derivative. *Biophys. J.* **96**, 2696–2708 (2009).
171. O’Connor D., Byrne A. & Keyes T. E. Linker length in fluorophore–cholesterol conjugates directs phase selectivity and cellular localisation in GUVs and live cells. *RSC Adv.* **9**, 22805–22816 (2019).
172. Collot M., Boutant E., Lehmann M. & Klymchenko A. S. BODIPY with Tuned Amphiphilicity as a Fluorogenic Plasma Membrane Probe. *Bioconjugate Chem.* **30**, 192–199 (2018).
173. MacDonald R. I. Characteristics of self-quenching of the fluorescence of lipid-conjugated rhodamine in membranes. *J. Biol. Chem.* **265**, 13533–13539 (1990).
174. London E. & Brown D. A. Insolubility of lipids in triton X-100: physical origin and relationship to sphingolipid/cholesterol membrane domains (rafts). *Biochim. Biophys. Acta, Biomembr.* **1508**, 182–195 (2000).
175. Lingwood D. & Simons K. Detergent resistance as a tool in membrane research. *Nat. Protoc.* **2**, 2159 (2007).
176. Manni M. M., Cano A., Alonso C. & Goñi F. M. Lipids that determine detergent resistance of MDCK cell membrane fractions. *Chem. Phys. Lipids* **191**, 68–74 (2015).
177. Komura N., Suzuki K. G., Ando H., Konishi M., Koikeda M., Imamura A., Chadda R., Fujiwara T. K., Tsuboi H., Sheng R., *et al.* Raft-based interactions of gangliosides with a GPI-anchored receptor. *Nat. Chem. Biol.* (2016).
178. Sengupta P., Hammond A., Holowka D. & Baird B. Structural determinants for partitioning of lipids and proteins between coexisting fluid phases in giant plasma membrane vesicles. *Biochim. Biophys. Acta, Biomembr.* **1778**, 20–32 (2008).

-
179. Bacia K., Schwille P. & Kurzchalia T. Sterol structure determines the separation of phases and the curvature of the liquid-ordered phase in model membranes. *Proc. Natl. Acad. Sci. U.S.A.* **102**, 3272–3277 (2005).
 180. Rissanen S., Grzybek M., Orłowski A., Róg T., Cramariuc O., Levental I., Eggeling C., Sezgin E. & Vattulainen I. Phase Partitioning of GM1 and Its Bodipy-Labeled Analog Determine Their Different Binding to Cholera Toxin. *Front. Physiol.* **8**, 252 (2017).
 181. Kahya N., Brown D. A. & Schwille P. Raft partitioning and dynamic behavior of human placental alkaline phosphatase in giant unilamellar vesicles. *Biochemistry* **44**, 7479–7489 (2005).
 182. Hammond A., Heberle F., Baumgart T., Holowka D., Baird B. & Feigenson G. Crosslinking a lipid raft component triggers liquid ordered-liquid disordered phase separation in model plasma membranes. *Proc. Natl. Acad. Sci. U.S.A.* **102**, 6320–6325 (2005).
 183. Kitov P. I. & Bundle D. R. Synthesis and structure–activity relationships of di- and trisaccharide inhibitors for Shiga-like toxin Type 1. *J. Chem. Soc., Perkin Trans. 1*, 838–853 (2001).
 184. Kitov P. I., Shimizu H., Homans S. W. & Bundle D. R. Optimization of tether length in nonglycosidically linked bivalent ligands that target sites 2 and 1 of a Shiga-like toxin. *J. Am. Chem. Soc.* **125**, 3284–3294 (2003).
 185. Römer W., Pontani L.-L., Sorre B., Rentero C., Berland L., Chambon V., Lamaze C., Bassereau P., Sykes C. & Gaus K. Actin dynamics drive membrane reorganization and scission in clathrin-independent endocytosis. *Cell* **140**, 540–553 (2010).
 186. Smith D. C., Sillence D. J., Falguieres T., Jarvis R. M., Johannes L., Lord J. M., Platt F. M. & Roberts L. M. The association of Shiga-like toxin with detergent-resistant membranes is modulated by glucosylceramide and is an essential requirement in the endoplasmic reticulum for a cytotoxic effect. *Mol. Biol. Cell* **17**, 1375–1387 (2006).
 187. Raa H., Grimmer S., Schwudke D., Bergan J., Wälchli S., Skotland T., Shevchenko A. & Sandvig K. Glycosphingolipid requirements for endosome-to-Golgi transport of Shiga toxin. *Traffic* **10**, 868–882 (2009).

7. References

188. Honigmann A., Mueller V., Hell S. W. & Eggeling C. STED microscopy detects and quantifies liquid phase separation in lipid membranes using a new far-red emitting fluorescent phosphoglycerolipid analogue. *Faraday Discuss.* **161**, 77–89 (2013).
189. Bordovsky S. S., Wong C. S., Bachand G. D., Stachowiak J. C. & Sasaki D. Y. Engineering lipid structure for recognition of the liquid ordered membrane phase. *Langmuir* **32**, 12527–12533 (2016).
190. Momin N., Lee S., Gadok A. K., Busch D. J., Bachand G. D., Hayden C. C., Stachowiak J. C. & Sasaki D. Y. Designing lipids for selective partitioning into liquid ordered membrane domains. *Soft Matter* **11**, 3241–3250 (2015).
191. Stefaniu C., Ries A., Gutowski O., Ruett U., Seeberger P. H., Werz D. B. & Brezesinski G. Impact of Structural Differences in Galactocerebrosides on the Behavior of 2D Monolayers. *Langmuir* **32**, 2436–2444 (2016).
192. Blume A. A comparative study of the phase transitions of phospholipid bilayers and monolayers. *Biochim. Biophys. Acta, Biomembr.* **557**, 32–44 (1979).
193. Morrow M. R., Singh D. M. & Grant C. W. Glycosphingolipid acyl chain order profiles: substituent effects. *Biochim. Biophys. Acta, Biomembr.* **1235**, 239–248 (1995).
194. Sáenz J. P., Sezgin E., Schwille P. & Simons K. Functional convergence of hopanoids and sterols in membrane ordering. *Proc. Natl. Acad. Sci. U.S.A.* **109**, 14236–14240 (2012).
195. Maté S., Busto J. V., García-Arribas A. B., Sot J., Vazquez R., Herlax V., Wolf C., Bakás L. & Goni F. M. N-Nervonoylsphingomyelin (c24: 1) prevents lateral heterogeneity in cholesterol-containing membranes. *Biophys. J.* **106**, 2606–2616 (2014).
196. Morrow M. R., Singh D. M. & Grant C. W. Glycosphingolipid headgroup orientation in fluid phospholipid/cholesterol membranes: similarity for a range of glycolipid fatty acids. *Biophys. J.* **69**, 955–964 (1995).
197. Ekholm O., Jaikishan S., Lönnfors M., Nyholm T. K. & Slotte J. P. Membrane bilayer properties of sphingomyelins with amide-linked 2-or 3-hydroxylated fatty acids. *Biochim. Biophys. Acta, Biomembr.* **1808**, 727–732 (2011).
198. Lingwood D., Binnington B., Róg T., Vattulainen I., Grzybek M., Coskun Ü., Lingwood C. A. & Simons K. Cholesterol modulates glycolipid conformation and receptor activity. *Nat. Chem. Biol.* **7**, 260–262 (2011).

-
199. Yahi N., Aulas A. & Fantini J. How Cholesterol Constrains Glycolipid Conformation for Optimal Recognition of Alzheimer's β Amyloid Peptide ($A\beta$ 1-40). *PLoS One* **5**, e9079 (2010).
 200. Balleza D., Mescola A., Marín–Medina N., Ragazzini G., Pieruccini M., Facci P. & Alessandrini A. Complex phase behavior of GUVs containing different Sphingomyelins. *Biophys. J.* **116**, 503–517 (2019).
 201. Marsh D. *Handbook of lipid bilayers* (CRC press, 2013).
 202. Ramstedt B. & Slotte J. P. Interaction of cholesterol with sphingomyelins and acyl-chain-matched phosphatidylcholines: a comparative study of the effect of the chain length. *Biophys. J.* **76**, 908–915 (1999).
 203. Niemelä P. S., Hyvönen M. T. & Vattulainen I. Influence of chain length and unsaturation on sphingomyelin bilayers. *Biophys. J.* **90**, 851–863 (2006).
 204. Maulik P., Sripada P. & Shipley G. Structure and thermotropic properties of hydrated N-stearoyl sphingomyelin bilayer membranes. *Biochim. Biophys. Acta, Biomembr.* **1062**, 211–219 (1991).
 205. Maulik P., Atkinson D. & Shipley G. X-ray scattering of vesicles of N-acyl sphingomyelins. Determination of bilayer thickness. *Biophys. J.* **50**, 1071–1077 (1986).
 206. Takahashi H., Hayakawa T., Kawasaki Y., Ito K., Fujisawa T., Kodama M. & Kobayashi T. Structural characterization of N-lignoceroyl (C24: 0) sphingomyelin bilayer membranes: a re-evaluation. *Appl. Crystallogr.* **40**, s312–s317 (2007).
 207. Róg T., Orłowski A., Llorente A., Skotland T., Sylvänne T., Kauhanen D., Ekroos K., Sandvig K. & Vattulainen I. Interdigitation of long-chain sphingomyelin induces coupling of membrane leaflets in a cholesterol dependent manner. *Biochim. Biophys. Acta, Biomembr.* **1858**, 281–288 (2016).
 208. Jaikishan S. & Slotte J. P. Effect of hydrophobic mismatch and interdigitation on sterol/sphingomyelin interaction in ternary bilayer membranes. *Biochim. Biophys. Acta, Biomembr.* **1808**, 1940–1945 (2011).
 209. Orth A., Johannes L., Römer W. & Steinem C. Creating and Modulating Microdomains in Pore-Spanning Membranes. *ChemPhysChem* **13**, 108–114 (2012).
 210. Hasegawa T. in *Glycobiophysics* 21–39 (Springer, 2018).
-

7. References

211. Todeschini A. R. & Hakomori S.-i. Functional role of glycosphingolipids and gangliosides in control of cell adhesion, motility, and growth, through glycosynaptic microdomains. *Biochim. Biophys. Acta, Gen. Subj.* **1780**, 421–433 (2008).
212. Missler M., Südhof T. C. & Biederer T. Synaptic cell adhesion. *Cold Spring Harb. Perspect. Biol.* **4**, a005694 (2012).
213. Honigsmann A., Sadeghi S., Keller J., Hell S. W., Eggeling C. & Vink R. A lipid bound actin meshwork organizes liquid phase separation in model membranes. *eLife* **3**, e01671 (2014).
214. Kuhlmann J. W., Mey I. P. & Steinem C. Modulating the lateral tension of solvent-free pore-spanning membranes. *Langmuir* **30**, 8186–8192 (2014).
215. Dai J. & Sheetz M. P. Membrane tether formation from blebbing cells. *Biophys. J.* **77**, 3363–3370 (1999).
216. Lieber A. D., Yehudai-Resheff S., Barnhart E. L., Theriot J. A. & Keren K. Membrane tension in rapidly moving cells is determined by cytoskeletal forces. *Curr. Biol.* **23**, 1409–1417 (2013).
217. Reineck P., Gómez D., Ng S. H., Karg M., Bell T., Mulvaney P. & Bach U. Distance and wavelength dependent quenching of molecular fluorescence by Au@ SiO₂ core-shell nanoparticles. *ACS Nano* **7**, 6636–6648 (2013).
218. Dulkeith E., Morteani A., Niedereichholz T., Klar T., Feldmann J., Levi S., Van Veggel F., Reinhoudt D., Möller M. & Gittins D. Fluorescence quenching of dye molecules near gold nanoparticles: radiative and nonradiative effects. *Phys. Rev. Lett.* **89**, 203002 (2002).
219. Dulkeith E., Ringler M., Klar T., Feldmann J., Munoz Javier A. & Parak W. Gold nanoparticles quench fluorescence by phase induced radiative rate suppression. *Nano Lett.* **5**, 585–589 (2005).
220. Kennedy G., Bui O. & Taylor S. Oxidation of silicon nitride films in an oxygen plasma. *J. Appl. Phys.* **85**, 3319–3326 (1999).
221. Hair M. L. Hydroxyl groups on silica surface. *J. Non-Cryst. Solids* **19**, 299–309 (1975).
222. Jennings T., Singh M. & Strouse G. Fluorescent lifetime quenching near d= 1.5 nm gold nanoparticles: probing NSET validity. *J. Am. Chem. Soc.* **128**, 5462–5467 (2006).

-
223. Kittredge K. W., Fox M. A. & Whitesell J. K. Effect of alkyl chain length on the fluorescence of 9-alkylfluorenyl thiols as self-assembled monolayers on gold. *J. Phys. Chem. B* **105**, 10594–10599 (2001).
224. Hiasa T. & Onishi H. Mercaptohexanol assembled on gold: FM-AFM imaging in water. *Colloid. Surface. A.* **441**, 149–154 (2014).
225. Fogarassy E., Slaoui A., Fuchs C. & Regolini J. Rapid thermal oxidation of silicon monoxide. *Appl. Phys. Lett.* **51**, 337–339 (1987).
226. Baumgärtel T., von Borczyskowski C. & Graaf H. Fluorescence studies of Rhodamine 6G functionalized silicon oxide nanostructures. *Nanotechnology* **21**, 475205 (2010).
227. Hayashi T., Castner T. & Boyd R. W. Quenching of molecular fluorescence near the surface of a semiconductor. *Chem. Phys. Lett.* **94**, 461–466 (1983).
228. Whitmore P., Alivisatos A. & Harris C. Distance Dependence of Electronic Energy Transfer to Semiconductor Surfaces: $n \rightarrow \pi^*$ Pyrazine/GaAs (110). *Phys. Rev. Lett.* **50**, 1092 (1983).
229. Sezgin E., Schneider F., Zilles V., Urbančič I., Garcia E., Waithe D., Klymchenko A. S. & Eggeling C. Polarity-Sensitive Probes for Superresolution Stimulated Emission Depletion Microscopy. *Biophys. J.* **113**, 1321–1330 (2017).
230. Schütte O. M., Mey I., Enderlein J., Savić F., Geil B., Janshoff A. & Steinem C. Size and mobility of lipid domains tuned by geometrical constraints. *Proc. Natl. Acad. Sci. U.S.A.* 201704199 (2017).
231. Sumitomo K. & Oshima A. Liquid-Ordered/Liquid-Crystalline Phase Separation at a Lipid Bilayer Suspended over Microwells. *Langmuir* **33**, 13277–13283 (2017).
232. Kudelski A. Chemisorption of 2-mercaptoethanol on silver, copper, and gold: direct Raman evidence of acid-induced changes in adsorption/desorption equilibria. *Langmuir* **19**, 3805–3813 (2003).
233. Liu J., Paddon-Row M. N. & Gooding J. J. Heterogeneous electron-transfer kinetics for flavin adenine dinucleotide and ferrocene through alkanethiol mixed monolayers on gold electrodes. *J. Phys. Chem. B* **108**, 8460–8466 (2004).
234. Kocun M., Lazzara T. D., Steinem C. & Janshoff A. Preparation of solvent-free, pore-spanning lipid bilayers: modeling the low tension of plasma membranes. *Langmuir* **27**, 7672–7680 (2011).
-

7. References

235. Mey I., Stephan M., Schmitt E. K., Müller M. M., Ben Amar M., Steinem C. & Janshoff A. Local membrane mechanics of pore-spanning bilayers. *J. Am. Chem. Soc.* **131**, 7031–7039 (2009).
236. Rawicz W., Olbrich K., McIntosh T., Needham D. & Evans E. Effect of chain length and unsaturation on elasticity of lipid bilayers. *Biophys. J.* **79**, 328–339 (2000).
237. Rawicz W., Smith B., McIntosh T., Simon S. & Evans E. Elasticity, strength, and water permeability of bilayers that contain raft microdomain-forming lipids. *Biophys. J.* **94**, 4725–4736 (2008).
238. Bezlyepkina N., Gracià R., Shchelokovskyy P., Lipowsky R. & Dimova R. Phase diagram and tie-line determination for the ternary mixture DOPC/eSM/cholesterol. *Biophys. J.* **104**, 1456–1464 (2013).
239. Kocun M. & Janshoff A. Pulling Tethers from Pore-Spanning Bilayers: Towards Simultaneous Determination of Local Bending Modulus and Lateral Tension of Membranes. *Small* **8**, 847–851 (2012).
240. Fuhrmans M. & Müller M. Mechanisms of vesicle spreading on surfaces: coarse-grained simulations. *Langmuir* **29**, 4335–4349 (2013).
241. Hoopes M. I., Faller R. & Longo M. L. Lipid domain depletion at small localized bends imposed by a step geometry. *Langmuir* **27**, 2783–2788 (2011).
242. Yoon T.-Y., Jeong C., Lee S.-W., Kim J. H., Choi M. C., Kim S.-J., Kim M. W. & Lee S.-D. Topographic control of lipid-raft reconstitution in model membranes. *Nat. Mater.* **5**, 281–285 (2006).
243. Parthasarathy R., Yu C.-h. & Groves J. T. Curvature-modulated phase separation in lipid bilayer membranes. *Langmuir* **22**, 5095–5099 (2006).
244. Callan-Jones A., Sorre B. & Bassereau P. Curvature-driven lipid sorting in biomembranes. *Cold Spring Harb. Perspect. Biol.* a004648 (2011).
245. Callan-Jones A. & Bassereau P. Curvature-driven membrane lipid and protein distribution. *Curr. Opin. Solid State Mater. Sci.* **17**, 143–150 (2013).
246. Gracià R. S., Bezlyepkina N., Knorr R. L., Lipowsky R. & Dimova R. Effect of cholesterol on the rigidity of saturated and unsaturated membranes: fluctuation and electrodeformation analysis of giant vesicles. *Soft Matter* **6**, 1472–1482 (2010).

-
247. Sorre B., Callan-Jones A., Manneville J.-B., Nassoy P., Joanny J.-F., Prost J., Goud B. & Bassereau P. Curvature-driven lipid sorting needs proximity to a demixing point and is aided by proteins. *Proc. Natl. Acad. Sci. U.S.A.* **106**, 5622–5626 (2009).
 248. Hu J., Weigl T. & Lipowsky R. Vesicles with multiple membrane domains. *Soft Matter* **7**, 6092–6102 (2011).
 249. McIntosh T. J., Vidal A. & Simon S. A. Sorting of lipids and transmembrane peptides between detergent-soluble bilayers and detergent-resistant rafts. *Biophys. J.* **85**, 1656–1666 (2003).
 250. Dimova R. Recent developments in the field of bending rigidity measurements on membranes. *Adv. Colloid Interfac.* **208**, 225–234 (2014).
 251. Baumgart T., Das S., Webb W. & Jenkins J. Membrane elasticity in giant vesicles with fluid phase coexistence. *Biophys. J.* **89**, 1067–1080 (2005).
 252. Kollmitzer B., Heftberger P., Podgornik R., Nagle J. F. & Pabst G. Bending rigidities and interdomain forces in membranes with coexisting lipid domains. *Biophys. J.* **108**, 2833–2842 (2015).
 253. Zhao Y., Das S. & Du Q. Adhesion of multicomponent vesicle membranes. *Phys. Rev. E: Stat., Nonlinear, Soft Matter Phys.* **81**, 041919 (2010).
 254. Semrau S., Idema T., Holtzer L., Schmidt T. & Storm C. Accurate determination of elastic parameters for multicomponent membranes. *Phys. Rev. Lett.* **100**, 088101 (2008).
 255. Vestergaard C. L. Optimizing experimental parameters for tracking of diffusing particles. *Phys. Rev. E: Stat., Nonlinear, Soft Matter Phys.* **94**, 022401 (2016).
 256. Muddana H. S., Gullapalli R. R., Manias E. & Butler P. J. Atomistic simulation of lipid and DiI dynamics in membrane bilayers under tension. *Phys. Chem. Chem. Phys.* **13**, 1368–1378 (2011).
 257. Reddy A. S., Warshaviak D. T. & Chachisvilis M. Effect of membrane tension on the physical properties of DOPC lipid bilayer membrane. *Biochim. Biophys. Acta, Biomembr.* **1818**, 2271–2281 (2012).
 258. Muddana H. S., Gullapalli R. R., Tabouillot T. & Butler P. J. Physiological membrane tension causes an increase in lipid diffusion: a single molecule fluorescence study. *Biophys. J.* **96**, 197a–198a (2009).

7. References

259. Thoms V. L., Hormel T. T., Reyer M. A. & Parthasarathy R. Tension Independence of Lipid Diffusion and Membrane Viscosity. *Langmuir* **33**, 12510–12515 (2017).
260. Hsieh C.-L., Spindler S., Ehrig J. & Sandoghdar V. Tracking single particles on supported lipid membranes: multimobility diffusion and nanoscopic confinement. *J. Phys. Chem. B* **118**, 1545–1554 (2014).
261. Spindler S., Ehrig J., König K., Nowak T., Piliarik M., Stein H. E., Taylor R. W., Garanger E., Lecommandoux S., Alves I. D., *et al.* Visualization of lipids and proteins at high spatial and temporal resolution via interferometric scattering (iSCAT) microscopy. *J. Phys. D: Appl. Phys.* **49**, 274002 (2016).
262. Liao Y.-H., Lin C.-H., Cheng C.-Y., Wong W. C., Juo J.-Y. & Hsieh C.-L. Monovalent and Oriented Labeling of Gold Nanoprobes for the High-Resolution Tracking of a Single Membrane Molecule. *ACS Nano* **13**, 10918–10928 (2019). accepted.
263. Carrer D. C., Schmidt A. W., Knölker H.-J. & Schwille P. Membrane domain-disrupting effects of 4-substitued cholesterol derivatives. *Langmuir* **24**, 8807–8812 (2008).
264. Kahya N., Scherfeld D., Bacia K., Poolman B. & Schwille P. Probing lipid mobility of raft-exhibiting model membranes by fluorescence correlation spectroscopy. *J. Biol. Chem.* **278**, 28109–28115 (2003).
265. Przybylo M., Sýkora J., Humpolíčková J., Benda A., Zan A. & Hof M. Lipid diffusion in giant unilamellar vesicles is more than 2 times faster than in supported phospholipid bilayers under identical conditions. *Langmuir* **22**, 9096–9099 (2006).
266. Schneider F., Waithe D., Clausen M. P., Galiani S., Koller T., Ozhan G., Eggeling C. & Sezgin E. Diffusion of lipids and GPI-anchored proteins in actin-free plasma membrane vesicles measured by STED-FCS. *Mol. Biol. Cell* **28**, 1507–1518 (2017).
267. Schwenen L. L., Hubrich R., Milovanovic D., Geil B., Yang J., Kros A., Jahn R. & Steinem C. Resolving single membrane fusion events on planar pore-spanning membranes. *Sci. Rep.* **5** (2015).
268. Schütz G. J., Kada G., Pastushenko V. P. & Schindler H. Properties of lipid microdomains in a muscle cell membrane visualized by single molecule microscopy. *EMBO J.* **19**, 892–901 (2000).

-
269. Feder T. J., Brust-Mascher I., Slattery J. P., Baird B. & Webb W. W. Constrained diffusion or immobile fraction on cell surfaces: a new interpretation. *Biophys. J.* **70**, 2767–2773 (1996).
270. Fujiwara T., Ritchie K., Murakoshi H., Jacobson K. & Kusumi A. Phospholipids undergo hop diffusion in compartmentalized cell membrane. *J. Cell Biol.* **157**, 1071–1082 (2002).
271. Eggeling C., Ringemann C., Medda R., Schwarzmann G., Sandhoff K., Polyakova S., Belov V. N., Hein B., von Middendorff C., Schönle A., *et al.* Direct observation of the nanoscale dynamics of membrane lipids in a living cell. *Nature* **457**, 1159–1162 (2009).
272. Veatch S. L. & Keller S. L. Seeing spots: complex phase behavior in simple membranes. *Biochim. Biophys. Acta, Mol. Cell Res.* **1746**, 172–185 (2005).
273. Pokorny A., Yandek L. E., Elegbede A. I., Hinderliter A. & Almeida P. F. Temperature and composition dependence of the interaction of δ -lysin with ternary mixtures of sphingomyelin/cholesterol/POPC. *Biophys. J.* **91**, 2184–2197 (2006).
274. Konyakhina T. M. & Feigenson G. W. Phase diagram of a polyunsaturated lipid mixture: brain sphingomyelin/1-stearoyl-2-docosahexaenoyl-sn-glycero-3-phosphocholine/cholesterol. *Biochim. Biophys. Acta, Biomembr.* **1858**, 153–161 (2016).
275. Kahya N., Scherfeld D., Bacia K. & Schwille P. Lipid domain formation and dynamics in giant unilamellar vesicles explored by fluorescence correlation spectroscopy. *J. Struct. Biol.* **147**, 77–89 (2004).
276. Veatch S. L. & Keller S. L. A Closer Look at the Canonical ‘Raft Mixture’ in Model Membrane Studies. *Biophys. J.* **84**, 725 (2003).
277. Baykal-Caglar E., Hassan-Zadeh E., Saremi B. & Huang J. Preparation of giant unilamellar vesicles from damp lipid film for better lipid compositional uniformity. *Biochim. Biophys. Acta, Biomembr.* **1818**, 2598–2604 (2012).
278. Huang J., Buboltz J. T. & Feigenson G. W. Maximum solubility of cholesterol in phosphatidylcholine and phosphatidylethanolamine bilayers. *Biochim. Biophys. Acta, Biomembr.* **1417**, 89–100 (1999).
279. Stevens M. M., Honerkamp-Smith A. R. & Keller S. L. Solubility limits of cholesterol, lanosterol, ergosterol, stigmaterol, and β -sitosterol in electroformed lipid vesicles. *Soft Matter* **6**, 5882–5890 (2010).
-

7. References

280. Rouhiparkouhi T., Weikl T. R., Discher D. E. & Lipowsky R. Adhesion-induced phase behavior of two-component membranes and vesicles. *Int. J. Mol. Sci.* **14**, 2203–2229 (2013).
281. Petruzielo R. S., Heberle F. A., Drazba P., Katsaras J. & Feigenson G. W. Phase behavior and domain size in sphingomyelin-containing lipid bilayers. *Biochim. Biophys. Acta, Biomembr.* **1828**, 1302–1313 (2013).
282. Carravilla P., Nieva J. L., Goñi F. M., Requejo-Isidro J. & Huarte N. Two-photon Laurdan studies of the ternary lipid mixture DOPC: SM: cholesterol reveal a single liquid phase at sphingomyelin: cholesterol ratios lower than 1. *Langmuir* **31**, 2808–2817 (2015).
283. Aufderhorst-Roberts A., Chandra U. & Connell S. D. Three-phase coexistence in lipid membranes. *Biophys. J.* **112**, 313–324 (2017).
284. Kuhlmann J. W., Junius M., Diederichsen U. & Steinem C. SNARE-Mediated Single-Vesicle Fusion Events with Supported and Freestanding Lipid Membranes. *Biophys. J.* **112**, 2348–2356 (2017).
285. Oshima A., Nakashima H. & Sumitomo K. Evaluation of lateral diffusion of lipids in continuous membrane between freestanding and supported areas by fluorescence recovery after photobleaching. *Langmuir* (2019).
286. Bacia K., Scherfeld D., Kahya N. & Schwille P. Fluorescence correlation spectroscopy relates rafts in model and native membranes. *Biophys. J.* **87**, 1034–1043 (2004).
287. Scherfeld D., Kahya N. & Schwille P. Lipid dynamics and domain formation in model membranes composed of ternary mixtures of unsaturated and saturated phosphatidylcholines and cholesterol. *Biophys. J.* **85**, 3758–3768 (2003).
288. Kahya N., Scherfeld D. & Schwille P. Differential lipid packing abilities and dynamics in giant unilamellar vesicles composed of short-chain saturated glycerol-phospholipids, sphingomyelin and cholesterol. *Chem. Phys. Lipids* **135**, 169–180 (2005).
289. Guo L., Har J. Y., Sankaran J., Hong Y., Kannan B. & Wohland T. Molecular diffusion measurement in lipid bilayers over wide concentration ranges: a comparative study. *ChemPhysChem* **9**, 721–728 (2008).
290. Levental I., Byfield F. J., Chowdhury P., Gai F., Baumgart T. & Janmey P. A. Cholesterol-dependent phase separation in cell-derived giant plasma-membrane vesicles. *Biochem. J.* **424**, 163–167 (2009).

-
291. Dietrich C., Bagatolli L., Volovyk Z., Thompson N., Levi M., Jacobson K. & Gratton E. Lipid rafts reconstituted in model membranes. *Biophys. J.* **80**, 1417–1428 (2001).
 292. Korlach J., Schwille P., Webb W. W. & Feigenson G. W. Characterization of lipid bilayer phases by confocal microscopy and fluorescence correlation spectroscopy. *Proc. Natl. Acad. Sci. U.S.A.* **96**, 8461–8466 (1999).
 293. Solanko L. M., Honigmann A., Midtiby H. S., Lund F. W., Brewer J. R., Dekaris V., Bittman R., Eggeling C. & Wüstner D. Membrane orientation and lateral diffusion of BODIPY-cholesterol as a function of probe structure. *Biophys. J.* **105**, 2082–2092 (2013).
 294. Wu H.-M., Lin Y.-H., Yen T.-C. & Hsieh C.-L. Nanoscopic substructures of raft-mimetic liquid-ordered membrane domains revealed by high-speed single-particle tracking. *Sci. Rep.* **6**, 20542 (2016).
 295. Ries J., Chiantia S. & Schwille P. Accurate determination of membrane dynamics with line-scan FCS. *Biophys. J.* **96**, 1999–2008 (2009).
 296. Chiantia S., Kahya N. & Schwille P. Raft domain reorganization driven by short-and long-chain ceramide: a combined AFM and FCS study. *Langmuir* **23**, 7659–7665 (2007).
 297. Schindelin J., Arganda-Carreras I., Frise E., Kaynig V., Longair M., Pietzsch T., Preibisch S., Rueden C., Saalfeld S., Schmid B., *et al.* Fiji: an open-source platform for biological-image analysis. *Nat. Methods* **9**, 676 (2012).
 298. Sibold J., Tewaag V., Vagedes T., Mey I. & Steinem C. Phase separation induced by surface adhesion (2019). in preparation.

A. Appendix

A.1. List of figures

1.1. Reported EHEC disease in Germany in the last five years.	1
1.2. Protein structure of STx.	3
1.3. The uptake of STx into the cell.	4
1.4. A schematically draw of the cell membrane.	6
1.5. Four different model membrane systems.	7
3.1. A SPR measurement.	29
3.2. Example GUV slide to show the analysis of the labeled Gb ₃ s.	31
3.3. The fluorophore marker distribution in the l_o/l_d and l_β/l_d phase separation in PSMs.	33
4.1. Schagger gel of different STxB purification's.	38
4.2. Adsorption isotherms of different STxB purification's.	40
4.3. Excitation and emission spectra of labeled Gb ₃ s.	42
4.4. Emission spectra of labeled Gb ₃ s with different l_d phase markers.	44
4.5. Self-quenching of labeled Gb ₃ s.	44
4.6. Liquid ordered phase distribution of the different fatty acid labeled Gb ₃ s without STxB.	46
4.7. Liquid ordered phase distribution of the different fatty acid labeled Gb ₃ s with STxB.	47
4.8. Visualization the binding of STxB to fatty acid labeled Gb ₃ s.	48
4.9. Phase distribution of head group labeled Gb ₃ s comparing the linker length.	51
4.10. Phase distribution of head group labeled Gb ₃ s comparing the saturation of the fatty acid.	53
4.11. Phase distribution of head group labeled Gb ₃ s comparing the hydroxylation of α position at the fatty acid.	54
4.12. Phase distribution of head group labeled Gb ₃ s with different sphingomyelins.	56

4.13. Visualization the binding of STxB to head group labeled Gb ₃ s.	59
5.1. Model of the pore-spanning membrane.	63
5.2. SEM images of different orthogonality evaporated substrates.	65
5.3. The different functionalizations for generating PSMs and there fluo- rescent properties.	66
5.4. Phase separation on pore-spanning membrane (PSM) with the SiO _x preparation.	68
5.5. The binding of STxB on phase-separated PSMs with the SiO _x func- tionalization.	70
5.6. The membrane tension of the pore-spanning membrane (PSM) from the gold mercaptoalcohol functionalization.	72
5.7. The membrane tension of the pore-spanning membrane (PSM) from the p-Si ₃ N ₄ and SiO _x functionalization.	74
5.8. The different Diffusion pathways of GNPs on PSMs	77
5.9. The different diffusion constant of GNPs on different functionalized PSMs.	78
5.10. The different diffusion coefficient for the l_d and l_o phase on PSMs. . .	80
5.11. Fluorescence micrographs of phase-separated PSMs at 25 °C and 55 °C. 83	
5.12. Phase separation on PSM with Chol 8 mol %.	85
5.13. Phase separation on PSM with Chol 15 mol %.	86
5.14. Phase separation on PSM with Chol 25 mol %.	87
5.15. The phase diagram in PSM with the lipid compositions DOPC/SM _{porc} / Chol (1;1;x).	88

A.2. List of schemes

3.1. Structure of DOPC.	11
3.2. Structure of Chol.	12
3.3. Structure of sphingomyelin.	12
3.4. Structure of ATTO655-DOPE.	14
3.5. Structure of TexasRed-DHPE.	14
3.6. Structure of ATTO655-DOPE.	15
3.7. Structure of Dy731-DOPE.	15
3.8. Structure of naphthopyrene.	16
3.9. Structure of BODIPY-Chol.	16
3.10. Structure of Gb ₃	17

3.11. Structures of fatty acid labeled Gb ₃ s.	18
3.12. Structures of head group labeled Gb ₃	19
3.13. A process chart to calculate the different intensities of the PSMs.	35
3.14. A schematically draw of the T_M calcualtion.	36
A.1. All labeled Gb ₃ s	129

A.3. List of tables

3.1. SM distribution of SM _{porc}	12
3.2. Sphingomyelins and their phase transition temperature.	13
4.1. K_d for the different STxB purification's.	39
4.2. Liquid ordered phase distribution of the different fatty acid labeled Gb ₃ s.	47
4.3. Liquid ordered phase distribution of the different head group labeled Gb ₃ s.	50
4.4. Head group labeled Gb ₃ s and their influence of the structure properties on liquid ordered phase distribution.	51
4.5. Liquid ordered phase distribution of the different head group labeled Gb ₃ s compared with different SMs.	57
5.1. The membrane tension from f-PSM on different functionalized substrates.	73
5.2. The diffusion coefficients from the PSM functionalization measured with iSCAT.	77
5.3. The diffusion coefficients from the PSM measured with FCS.	81
A.1. Comparison of different lipid diffusion constants.	126
A.2. Comparison of different membrane tensions in PSMs.	128
A.3. LMM result of fatty acid labeled Gb ₃ with no STxB.	130
A.4. LMM result of fatty acid labeled Gb ₃ with STxB.	131
A.5. LMM result of head group labeled Gb ₃ with SM _{porc}	131
A.6. LMM result of head group labeled Gb ₃ with PEG ₁₃ linker and SM _{porc}	132
A.7. LMM result of head group labeled Gb ₃ with different SMs.	132
A.8. LMM result of head group labeled Gb ₃ with PEG ₁₃ linker and different SMs.	133
A.9. LMM result of membrane tension.	134

A.4. Lipid diffusion constants

Table A.1.: Comparison of measured diffusion coefficients for different lipid model systems and lipid phases obtained by different methods. Lipid mixtures are: A=SM_{porc}/Chol, B=DOPC/POPE/POPS/Chol, C=DOPC/SM_{porc}/Chol, D=DOPC/Chol, E=DOPC/SM C_{18:0}/Chol, F=DLPC/DPPC/Chol, G=DLPC/SM C_{18:0}/Chol, H=DMPC/SM C_{18:0}/Chol, I=DOPC/SM_{egg}/Chol, J=DPPC/Chol, K=POPC/Chol, L=DPhPC/DPPC/Chol.

System/Surface	Lipids	Method	Phase	Fluorophore	$D/\mu\text{m}^2 \text{s}^{-1}$
f-PSM/SiO _x ¹	DOPC	Z-scan FCS	l_d	ATTO655-DOPE	11.2 ± 0.9
f-PSM/SiO _x ¹	DOPC	Z-scan FCS	l_d	TexasRed-DHPE	12.4 ± 1.1
f-PSM/SiO _x ¹	A (3:2)	Z-scan FCS	l_o	BODIPY-Chol	0.78 ± 0.05
f-PSM/SiO _x ¹	A (3:2)	Z-scan FCS	l_o	naphthopyrene	0.57 ± 0.07
f-PSM/p-Si ₃ N ₄ ²	DOPC	SPT	l_d	40 nm GNP	2.6 ± 1.0
s-PSM/p-Si ₃ N ₄ ²	DOPC	SPT	l_d	40 nm GNP	0.8 ± 0.5
f-PSM/6MH-Au ²	DOPC	SPT	l_d	40 nm GNP	1.8 ± 0.7
s-PSM/6MH-Au ²	DOPC	SPT	l_d	40 nm GNP	1.9 ± 0.7
f-PSM/6MH-Au ^[267]	B (5:2:1:2)	FCS	l_d	ATTO488-DPPE	7.7 ± 0.4
f-PSM/6MH-Au ^[267]	B (5:2:1:2)	FCS	l_d	DPPE-KK114	7.4 ± 0.3
s-PSM/6MH-Au ^[284]	B (5:2:1:2)	FRAP	l_d	ATTO488-DPPE	2.8 ± 0.4
f-PSM/SiO ₂ ^[285]	DOPC	FRAP	l_d	Rhod-DOPE	5.2
s-PSM/SiO ₂ ^[285]	DOPC	FRAP	l_d	Rhod-DOPE	0.26,2.6
GUV ^[261]	DOPC	SPT	l_d	40 nm GNP	4.88 ± 0.04
GUV ^[265]	DOPC	Z-scan FCS	l_d	BODIPY 500/510-PC	7.8 ± 0.8
GUV ^[266]	DOPC	FCS	l_d	ATTO647N-DOPE	~ 8.5
GUV ^[266]	DOPC	FCS	l_d	BODIPY-Chol	~ 8.5
GUV ^[170]	DOPC	FCS	l_d	BODIPY-Chol	7.23
GUV ^[264]	DOPC	FCS	l_d	DiI-C ₁₈	6.3 ± 0.2
GUV ^[263]	C (2:2:1)	Z-scan FCS	l_d	DiD-C ₁₈	6.1 ± 0.5
GUV ^[263]	C (2:2:1)	Z-scan FCS	l_o	DiD-C ₁₈	0.3 ± 0.1
GUV ^[264]	D (4:1)	FCS	l_d	DiI-C ₁₈	4.8
GUV ^[264]	D (1:2)	FCS	l_d	DiI-C ₁₈	2.4
GUV ^[264]	E (2:2:1)	FCS	l_d	DiI-C ₁₈	5.15 ± 0.15
GUV ^[264]	E (2:2:1)	FCS	l_o	DiI-C ₁₈	0.255 ± 0.058
GUV ^[286]	DOPC	FCS	l_d	DiI-C ₁₈	7.0 ± 1.2
GUV ^[286]	E (1:1:1)	FCS	l_d	DiI-C ₁₈	4.8 ± 0.9
GUV ^[286]	E (1:1:1)	FCS	l_o	DiI-C ₁₈	2.0 ± 1.0
GUV ^[287]	F (2:2:1)	FCS	l_d	DiI-C ₁₈	~ 4.5
GUV ^[287]	F (2:2:1)	FCS	l_o	DiI-C ₁₈	~ 0.4
GUV ^[288]	G (1:1:2)	FCS	l_d	DiI-C ₁₈	0.80

¹Measurements were performed by Thomas Vagedes during his master thesis (table 5.3).

²Measurements were done in cooperation with Prof. Dr. Vahid Sandoghdar and were performed by Susann Spindler. The results are published (table 5.2).^[147]

A.4. Lipid diffusion constants

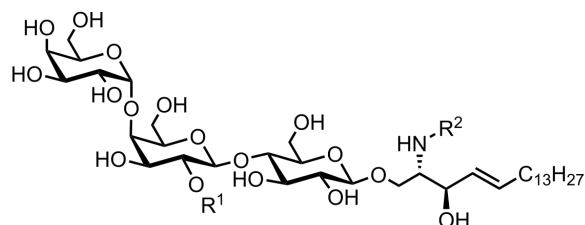
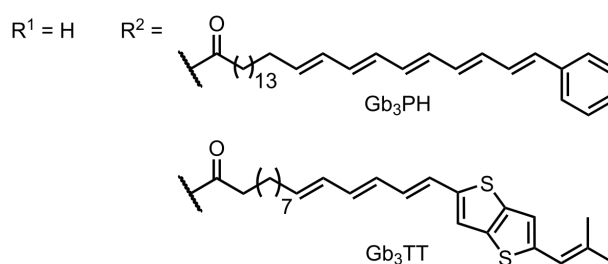
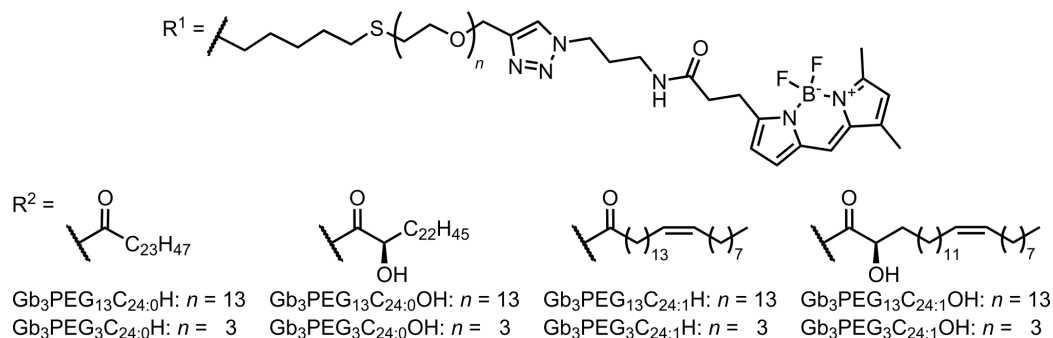
System/Surface	Lipids	Method	Phase	Fluorophore	$D/\mu\text{m}^2\text{s}^{-1}$
GUV ^[288]	G (1:1:2)	FCS	l_o	DiI-C ₁₈	0.55
GUV ^[288]	H (1:1:2)	FCS	l_d	DiI-C ₁₈	0.60
GUV ^[288]	H (1:1:2)	FCS	l_o	DiI-C ₁₈	0.36
GUV ^[170]	I (7:1:2)	FCS	l_o	BODIPY-Chol	4.98
GUV ^[289]	POPC	FCS	l_d	Rhod-PE-POPC	6.2 ± 1.1
GUV ^[289]	POPC	FRAP	l_d	Rhod-PE-POPC	3.3 ± 1.8
GUV ^[259]	DOPC	FRAP	l_d	TexasRed-DHPE	~ 5
GPMV ^[266]	GPMV	FCS	l_d	ATTO647N-DOPE	~ 2.5
GPMV ^[290]	GPMV	FCS	l_d	Rhod-PE-SOPC	5.6
GPMV ^[290]	GPMV	FCS	l_o	Rhod-PE-SOPC	1.8
SSM/glass ^[262]	DOPC	SPT	l_d	10 nm GNP	3.01 ± 0.35
SSM/glass ^[262]	DOPC	SPT	l_d	15 nm GNP	2.87 ± 0.33
SSM/glass ^[262]	DOPC	SPT	l_d	20 nm GNP	2.37 ± 0.17
SSM/glass ^[262]	DOPC	SPT	l_d	30 nm GNP	2.28 ± 0.16
SSM/glass ^[262]	DOPC	SPT	l_d	40 nm GNP	2.01 ± 0.17
SSM/glass ^[262]	DOPC	SPT	l_d	ATTO647N-DOPE	2.15 ± 0.67
SSM/glass ^[262]	DOPC	SPT	l_d	ATTO532-DOPE	2.63 ± 0.92
SSM/glass ^[260]	DOPC	SPT	l_d	40 nm GNP	0.22
SSM/glass ^[291]	C (1:1:1)	SPT	l_d	40 nm GNP	1.1
SSM/glass ^[291]	C (1:1:1)	SPT	l_o	40 nm GNP	0.38
GUV/glass ^[292]	DLPC	FCS	l_d	BODIPY-PC	3
GUV/glass ^[292]	F (9:9:2)	FCS	l_o	BODIPY-PC	0.3
GUV/glass ^[292]	J (2:3)	FCS	l_o	BODIPY-PC	0.15
SSM/glass ^[293]	DOPC	FCS	l_d	BODIPY-Chol	3.2
SSM/glass ^[293]	K (7:3)	FCS	l_o	BODIPY-Chol	1.7
SSM/mica ^[294]	L (2:2:1)	SPT	l_d	20 nm GNP	1.43 ± 0.50
SSM/mica ^[294]	L (2:2:1)	SPT	l_o	20 nm GNP	0.24 ± 0.12
SSM/mica ^[265]	DOPC	Z-scan FCS	l_d	BODIPY 500/510-PC	3.1 ± 0.3
SSM/mica ^[295]	C (10:10:7)	L-scan FCS	l_d	BODIPY-Chol	6.2 ± 0.4
SSM/mica ^[295]	C (10:10:7)	L-scan FCS	l_o	BODIPY-Chol	0.42 ± 0.02
SSM/mica ^[188]	L (20:20:17)	FCS	l_d	DSPE-KK114	1.9
SSM/mica ^[188]	DOPC	FCS	l_d	DSPE-PEG-KK114	9
SSM/mica ^[188]	D (7:3)	FCS	l_d	DSPE-PEG-KK114	2.6
SSM/mica ^[188]	L (20:20:17)	FCS	l_d	DSPE-PEG-KK114	1.8
SSM/mica ^[188]	L (20:20:17)	FCS	l_o	DSPE-PEG-KK114	0.7
SSM/mica ^[296]	E (3:3:2)	FCS	l_d	BODIPY-Chol	6
SSM/mica ^[296]	E (3:3:2)	FCS	l_o	BODIPY-Chol	0.15

A.5. Membrane tension of pore-spanning membranes

Table A.2.: Comparison measured different membrane tension on different functionalizations of the porous substrates, 2-mercapto-1-ethanol on gold (2ME-Au), 6-mercapto-1-hexanol on gold (6MH-Au), 6MH-Au + *O*-cholesteryl *N*-(8'-mercapto-3',6'-dioxaoctyl)carbamate (CPEO3), 8-mercapto-1-octanol on gold (8MO-Au), octan-1-thiol on gold (OT-Au), 11-mercapto-1-undecanol on gold (11MUD-Au), 6-mercapto-1-hexanol on gold (6MH-Au), plasma cleaned silicon nitride (p-Si₃N₄) or silicon oxide (SiO_x) and different preparation methods, spreading of GUVs or painting the membrane over the porous substrate. The membrane tension (σ) was measured also with different lipids and lipid compositions, A=POPC/Chol, B=DOPC/Chol, C=DPPC/Chol, D=SM_{porc}/Chol.

Functionalization	Lipids	Preparation	$\sigma/\text{mN m}^{-1}$
2ME-Au	DOPC	GUV	1.6 ± 1.1
2ME-Au ^[239]	POPC	GUV	2.4 ± 0.5
2ME-Au ^[239]	A (3:1)	GUV	2.6 ± 0.9
2ME-Au ^[234]	POPC	GUV	2.00 ± 0.09
2ME-Au ^[234]	DOPC	GUV	1.018 ± 0.014
2ME-Au ^[234]	B (7:3)	GUV	3.50 ± 0.15
6MH-Au	DOPC	GUV	0.6 ± 0.4
6MH-Au ³	DOPC	GUV	0.4 ± 0.1
6MH-Au ^[214]	DPhPC	GUV	1.4
6MH-Au + 9.1 % CPEO3 ^[214]	DPhPC	GUV	5.0
OT-Au ^[235]	DPhPC	GUV	26 ± 4
OT-Au ^[235]	DPhPC	painting	18 ± 3
OT-Au ^[235]	DPPC	painting	31 ± 3
OT-Au ^[235]	C (3:1)	painting	23 ± 3
8MO-Au	DOPC	GUV	3.2 ± 0.9
11MUD-Au	DOPC	GUV	2.1 ± 1.4
16MHD-Au	DOPC	GUV	1.0 ± 0.4
p-Si ₃ N ₄	DOPC	GUV	1.6 ± 0.5
p-Si ₃ N ₄ ³	DOPC	GUV	1.2 ± 0.4
SiO _x	DOPC	GUV	10.5 ± 4.3
SiO _x	D (3:2)	GUV	6.7 ± 4.0
SiO ₂ ^[235]	DPhPC	GUV	0.15 ± 0.05

³Measurements were done in cooperation with Prof. Dr. Vahid Sandoghdar. The results are published.^[147]

A.6. Fluorescence labeled Gb₃Gb₃fatty acid labeled Gb₃head group labeled Gb₃

Scheme A.1.: A schematic overview from all labeled globotriaosyl ceramides (Gb₃s). The ground structure is a Gb₃ with two different residues one at the head group (R¹) and the second the fatty acid (R²). The fatty acid labeled Gb₃s have no modification at the head group (R¹=H), but there are two different fatty acids, which resulted in the globotriaosyl ceramid phenyl-modified fatty acid (Gb₃PH) and globotriaosyl ceramid thienothiopyran-modified fatty acid (Gb₃TT). The head group labeled Gb₃s are modified at the head group with a PEG linker with the linker length (n=3,13) and a BODIPY. The fatty acid varied also in four different solutions. In total there are eight different structures which were shorten to Gb₃PEG_nC_{24:Δ}X.

A.7. Statistical analyses

A linear mixed-effects model (LMM) was fitted to the data in order to evaluate effects of the data.

$$\text{Data} = X\beta + Zu + \epsilon \quad (\text{A.1})$$

The measured data are listed in a long vector. The data belongs to different groups of interest which is set in the fixed effect coefficient matrix X . The fixed effects are the influences of interest and stands in the vector β . The distribution of the data are broadened by systematical distributions (random effects). The coefficient matrix of this systematical errors is Z and the vector of the systematical distribution which has normal distributions as elements is u . Additionally a vector of random error (ϵ) was included which is normal distributed. The equation is optimized by optimizing the normal distributions with a maximum likelihood estimation.

A.7.1. Results of the linear mixed-effects model for the fatty acid labeled globotriaosyl ceramide

The statistical analysis of the different LMM models are summarized in the following short tables. The differences are calculated as following $\Delta\text{FattyAcid} = \%l_o(\text{Gb}_3\text{PH}) - \%l_o(\text{Gb}_3\text{TT})$, $\Delta\text{STxB} = \%l_o(+ \text{STxB}) - \%l_o(- \text{STxB})$. The LMM has a starting population, which were influenced by fixed-effects and random-effects. The effects with fixed influences, like the influence of the fatty acid to the l_o phase distribution ($\%l_o$) of the head group labeled Gb_3 , were shorten in the LMM equation as an addend. Effects, which influences the distribution of the statistic are random-effects, like the preparation days or the different GUVs. This random effects were written in the LMM equation like (1 | <random effect>).

Table A.3.: The used model: liquid ordered phase distribution ($\%l_o$)= $\text{Gb}_3\text{PH} + \Delta\text{FattyAcid} + (1 | \text{Day}) + (1 | \text{GUV})$. All two different fatty acid labeled Gb_3 were used in GUV composed of DOPC/ SM_{porc} /Chol/ Gb_3 /Dy731-DOPE (39:35:20:5:1) before STxB incubation; $R^2 = 0.6710$

Difference	$\Delta\%l_o$	p-Value
Gb_3PH	0.40 ± 0.02	2.4×10^{-205}
$\Delta\text{FattyAcid}$	0.16 ± 0.02	3.1×10^{-22}

Table A.4.: The used model: liquid ordered phase distribution ($\%l_o$)= $Gb_3PH + \Delta FattyAcid + \Delta STxB$ (1 | Day) + (1 | GUV). All two different fatty acid labeled Gb_3 were used in GUV composed of DOPC/ SM_{porc} /Chol/ Gb_3 /Dy731-DOPE (39:35:20:5:1) before and after STxB incubation; $R^2 = 0.6266$

Difference	$\Delta\%l_o$	p-Value
Gb_3PH	0.39 ± 0.02	3.9×10^{-286}
$\Delta FattyAcid$	0.16 ± 0.02	1.7×10^{-44}
$\Delta STxB$	-0.01 ± 0.02	0.19

A.7.2. Results of the linear mixed-effects model for the head group labeled globotriaosyl ceramide

The statistical analysis of the different LMM models are summarized in the following short tables. The differences are calculated as following $\Delta PEG = \%l_o(PEG_{13}) - \%l_o(PEG_3)$, $\Delta C_{24} = \%l_o(C_{24:0}) - \%l_o(C_{24:1})$ and $\Delta OH = \%l_o(H) - \%l_o(OH)$. The LMM has a starting population, which were influenced by fixed-effects and random-effects. The effects with fixed influences, like the influence of the linker length to the $\%l_o$ of the head group labeled Gb_3 , were shorten in the LMM equation as an addend. Effects, which influences the distribution of the statistic are random-effects, like the preparation days or the different GUVs. This random effects were written in the LMM equation like (1 | <random effect>).

Measurements with SM_{porc}

Table A.5.: The used model: liquid ordered phase distribution ($\%l_o$)= $Gb_3PEG_{13}C_{24:0}H + \Delta PEG + \Delta C_{24} + \Delta OH$ + (1 | Day) + (1 | GUV). All eight different head group labeled Gb_3 were used in GUV with the lipid mixture DOPC/ SM_{porc} /Chol/ Gb_3 /Dy731-DOPE (39:39:20:1:1); $R^2 = 0.9201$

Difference	$\Delta\%l_o$	p-Value
$Gb_3PEG_{13}C_{24:0}H$	0.72 ± 0.03	1.4×10^{-250}
ΔPEG	0.27 ± 0.03	1.3×10^{-32}
ΔC_{24}	0.19 ± 0.03	1.6×10^{-16}
ΔOH	0.01 ± 0.03	0.67

Table A.6.: The used model: liquid ordered phase distribution ($\%l_o$)= $\text{Gb}_3\text{PEG}_{13}\text{C}_{24:0}\text{H} + \Delta\text{C}_{24} + \Delta\text{OH} + (1 | \text{Day}) + (1 | \text{GUV})$. The head group labeled Gb_3 with the long PEG linker were used in GUV with the lipid mixture $\text{DOPC}/\text{SM}_{\text{porc}}/\text{Chol}/\text{Gb}_3/\text{Dy731-DOPE}$ (39:39:20:1:1); $R^2 = 0.8695$

Difference	$\Delta\%l_o$	p-Value
$\text{Gb}_3\text{PEG}_{13}\text{C}_{24:0}\text{H}$	0.74 ± 0.03	9.4×10^{-186}
ΔC_{24}	0.24 ± 0.04	3.7×10^{-15}
ΔOH	0.01 ± 0.04	0.76

Measurements with different sphingomyelin species

Table A.7.: The used model: liquid ordered phase distribution ($\%l_o$) = $\text{Gb}_3\text{PEG}_{13}\text{C}_{24:0}\text{H}$ in $\text{SM C}_{16:0} + \Delta\text{SM} + \Delta\text{PEG} + \Delta\text{C}_{24} + \Delta\text{OH} + (1 | \text{Day}) + (1 | \text{GUV})$. All eight different head group labeled Gb_3 were used in GUV with the lipid mixture $\text{DOPC}/\text{SM}/\text{Chol}/\text{Gb}_3/\text{Dy731-DOPE}$ (39:39:20:1:1); $R^2 = 0.9495$

Difference	$\Delta\%l_o$	p-Value
$\text{Gb}_3\text{PEG}_{13}\text{C}_{24:0}\text{H}$ in $\text{SM C}_{16:0}$	0.48 ± 0.03	1.2×10^{-75}
$\Delta\text{SM C}_{16:0}-\text{SM C}_{18:0}$	-0.03 ± 0.03	0.36
$\Delta\text{SM C}_{16:0}-\text{SM C}_{20:0}$	-0.21 ± 0.03	1.8×10^{-12}
$\Delta\text{SM C}_{16:0}-\text{SM C}_{22:0}$	-0.19 ± 0.03	4.7×10^{-11}
$\Delta\text{SM C}_{16:0}-\text{SM C}_{24:0}$	-0.19 ± 0.03	8.1×10^{-12}
$\Delta\text{SM C}_{18:0}-\text{SM C}_{20:0}$	-0.18 ± 0.03	7.4×10^{-10}
$\Delta\text{SM C}_{18:0}-\text{SM C}_{22:0}$	-0.17 ± 0.03	1.2×10^{-8}
$\Delta\text{SM C}_{18:0}-\text{SM C}_{24:0}$	-0.17 ± 0.03	2.9×10^{-9}
$\Delta\text{SM C}_{20:0}-\text{SM C}_{22:0}$	0.01 ± 0.04	0.65
$\Delta\text{SM C}_{20:0}-\text{SM C}_{24:0}$	0.01 ± 0.03	0.78
$\Delta\text{SM C}_{22:0}-\text{SM C}_{24:0}$	-0.01 ± 0.03	0.86
ΔPEG	0.31 ± 0.02	2.6×10^{-65}
ΔC_{24}	0.16 ± 0.02	6.3×10^{-18}
ΔOH	-0.03 ± 0.02	0.15

Table A.8.: The used model: liquid ordered phase distribution ($\%l_o$)= $\text{Gb}_3\text{PEG}_{13}\text{C}_{24:0}\text{H}$ in $\text{SM C}_{16:0} + \Delta\text{SM} + \Delta\text{C}_{24} + \Delta\text{OH} + (1 \mid \text{Day}) + (1 \mid \text{GUV})$. The head group labeled Gb_3 with the long PEG linker were used in GUV with the lipid mixture $\text{DOPC}/\text{SM}/\text{Chol}/\text{Gb}_3/\text{Dy731-DOPE}$ (39:39:20:1:1); $R^2 = 0.9178$

Difference	$\Delta\%l_o$	p-Value
$\text{Gb}_3\text{PEG}_{13}\text{C}_{24:0}\text{H}$ in $\text{SM C}_{16:0}$	0.46 ± 0.03	3.3×10^{-53}
$\Delta\text{SM C}_{16:0} - \text{SM C}_{18:0}$	-0.09 ± 0.04	8.8×10^{-3}
$\Delta\text{SM C}_{16:0} - \text{SM C}_{20:0}$	-0.25 ± 0.04	1.1×10^{-11}
$\Delta\text{SM C}_{16:0} - \text{SM C}_{22:0}$	-0.25 ± 0.04	4.7×10^{-12}
$\Delta\text{SM C}_{16:0} - \text{SM C}_{24:0}$	-0.29 ± 0.04	2.5×10^{-15}
$\Delta\text{SM C}_{18:0} - \text{SM C}_{20:0}$	-0.16 ± 0.04	1.0×10^{-5}
$\Delta\text{SM C}_{18:0} - \text{SM C}_{22:0}$	-0.16 ± 0.04	5.4×10^{-6}
$\Delta\text{SM C}_{18:0} - \text{SM C}_{24:0}$	-0.20 ± 0.04	2.6×10^{-8}
$\Delta\text{SM C}_{20:0} - \text{SM C}_{22:0}$	-0.00 ± 0.04	0.90
$\Delta\text{SM C}_{20:0} - \text{SM C}_{24:0}$	-0.04 ± 0.04	0.27
$\Delta\text{SM C}_{22:0} - \text{SM C}_{24:0}$	-0.04 ± 0.04	0.33
ΔC_{24}	0.22 ± 0.03	6.4×10^{-21}
ΔOH	0.02 ± 0.03	0.52

A.7.3. Statistical analyzing of Membrane tension by using the LMM

The statistical analysis of the LMM model is summarized in the following short tables. The differences of the membrane tension according there functionalization is explained in the tables. The LMM has a starting population, which were influenced by fixed-effects and random-effects. The effects with fixed influences were shorten in the LMM equation as an addend. Effects, which influences the distribution of the statistic are random-effects, like the preparation days. This random effects were written in the LMM equation like $(1 \mid \langle \text{random effect} \rangle)$.

Table A.9.: The used model was, membrane tension (σ)=2ME-Au+ Δ functionalization + (1 | Day). $R^2= 0.8628$. The membrane tension (σ) of the f-PSM composed of DOPC/ ATTO488-DPPE (99.5:0.5) was measured on different functionalizations. The lipid composition of the l_o phase on SiO_x functionalized substrate was $\text{SM}_{\text{porc}}/\text{Chol}/\text{ATTO655-DOPE}$ (59.5:39.5:1). The analyze method is described in chapter 3.3.3.

Difference	$\Delta\sigma \text{ mN m}^{-1}$	p-Value
2ME-Au	2.1 ± 1.1	0.047
Δ 2ME-Au-6MH-Au	1.3 ± 2.0	0.50
Δ 2ME-Au-8MO-Au	-1.3 ± 1.7	0.52
Δ 2ME-Au-11MUD-Au	0.2 ± 1.9	0.42
Δ 2ME-Au-16MHD-Au	1.0 ± 1.7	0.92
Δ 2ME-Au-p-Si ₃ N ₄	-0.5 ± 2.5	0.84
Δ 2ME-Au-SiO _x	-7.0 ± 1.5	1.4×10^{-6}
Δ 2ME-Au-SiO _x l_o	5.1 ± 1.5	4.5×10^{-4}
6MH-Au	0.73 ± 1.70	0.66
Δ 6MH-Au-8MO-Au	-2.7 ± 2.2	0.21
Δ 6MH-Au-11MUD-Au	-1.1 ± 2.3	0.62
Δ 6MH-Au-16MHD-Au	-0.3 ± 2.1	0.89
Δ 6MH-Au-p-Si ₃ N ₄	0.8 ± 2.8	0.77
Δ 6MH-Au-SiO _x	-8.3 ± 2.0	2.0×10^{-5}
Δ 6MH-Au-SiO _x l_o	-6.4 ± 2.0	1.0×10^{-3}
8MO-Au	3.4 ± 1.4	9.6×10^{-4}
Δ 8MO-Au-11MUD-Au	1.5 ± 2.1	0.46
Δ 8MO-Au-16MHD-Au	2.4 ± 1.9	0.20
Δ 8MO-Au-p-Si ₃ N ₄	1.8 ± 2.6	0.48
Δ 8MO-Au-SiO _x	-5.7 ± 1.7	5.9×10^{-4}
Δ 8MO-Au-SiO _x l_o	-3.8 ± 1.7	0.023
Δ 6MH-Au-SiO _x l_o	-6.4 ± 2.0	1.0×10^{-3}
11MUD-Au	1.9 ± 1.6	0.24
Δ 11MUD-Au-16MHD-Au	0.86 ± 2.10	0.67
Δ 11MUD-Au-p-Si ₃ N ₄	0.32 ± 2.80	0.91
Δ 11MUD-Au-SiO _x	-7.2 ± 1.9	1.3×10^{-4}
Δ 11MUD-Au-SiO _x l_o	-5.3 ± 1.9	5.0×10^{-3}
16MHD-Au	1.0 ± 1.3	0.43
Δ 16MHD-Au-p-Si ₃ N ₄	0.54 ± 2.60	0.83
Δ 16MHD-Au-SiO _x	-8.1 ± 1.7	9.4×10^{-7}

Difference	$\Delta\sigma$ mN m ⁻¹	p-Value
Δ 16MHD-Au-SiO _x l _o	-6.1 ± 1.7	1.9×10^{-4}
p-Si ₃ N ₄	1.6 ± 2.2	0.48
Δ p-Si ₃ N ₄ -SiO _x	-7.5 ± 2.5	2.1×10^{-3}
Δ p-Si ₃ N ₄ -SiO _x l _o	-5.6 ± 2.5	0.022
SiO _x	9.07 ± 1.01	1.6×10^{-18}
Δ SiO _x -SiO _x l _o	1.9 ± 1.5	0.18
SiO _x l _o	7.2 ± 1.0	3.9×10^{-12}

A.8. Chemicals and consumables

2-mercapto-1-ethanol	Sigma-Aldrich, Taufkirchen, Germany
3-aminopropyltrimethoxysilane	Sigma-Aldrich, Taufkirchen, Germany
6-mercapto-1-hexanol	Sigma-Aldrich, Taufkirchen, Germany
8-mercapto-1-octanol	Sigma-Aldrich, Taufkirchen, Germany
octan-1-thiol	Sigma-Aldrich, Taufkirchen, Germany
12-mercapto-1-dodecanol	Dojindo EU GmbH, Munich, Germany
16-mercapto-1-hexadecanol	Santa Cruz Biotechnology, Inc., Heidelberg, Germany
Ar	Air Liquide Deutschland GmbH, Düsseldorf, Germany
Au, 99.99 %	Allgemeine Gold- und Silberscheideanstalt, Pforzheim, Germany
ATTO488-DOPE	ATTO-TEC, Siegen, Germany
ATTO488-DPPE	ATTO-TEC, Siegen, Germany
ATTO532-DOPE	ATTO-TEC, Siegen, Germany
ATTO655-DOPE	ATTO-TEC, Siegen, Germany
cb-DOPE	Avanti Polar Lipids, Alabaster, AL, US
BL-AC40TS-C2	Olympus, Tokio, Japan
BODIPY-Chol	Avanti Polar Lipids, Alabaster, AL, US
BSA	Carl Roth GmbH, Karlsruhe, Germany
CaCl ₂ · (H ₂ O) ₂	Merck KGaA, Darmstadt, Germany
Chloroform	VWR International, Darmstadt, Germany
Chol	Sigma-Aldrich, Taufkirchen, Germany
Cu-band	Präzisions Glas & Optik GmbH, Iserlohn, Germany

A. Appendix

Cy3 STxB	Provided by Prof. Dr. Winfried Römer
DOPC	Avanti Polar Lipids, Alabaster, AL, US
Dy731-DOPE	Provided by Prof. Dr. Daniel B. Werz
Ethanol	Carl Roth GmbH, Karlsruhe, Germany
Gb ₃ PEG ₃ C _{24:0} H	Provided by Prof. Dr. Daniel B. Werz
Gb ₃ PEG ₃ C _{24:1} H	Provided by Prof. Dr. Daniel B. Werz
Gb ₃ PEG ₃ C _{24:0} OH	Provided by Prof. Dr. Daniel B. Werz
Gb ₃ PEG ₃ C _{24:1} OH	Provided by Prof. Dr. Daniel B. Werz
Gb ₃ PEG ₁₃ C _{24:0} H	Provided by Prof. Dr. Daniel B. Werz
Gb ₃ PEG ₁₃ C _{24:1} H	Provided by Prof. Dr. Daniel B. Werz
Gb ₃ PEG ₁₃ C _{24:0} OH	Provided by Prof. Dr. Daniel B. Werz
Gb ₃ PEG ₁₃ C _{24:1} OH	Provided by Prof. Dr. Daniel B. Werz
Gb ₃ PH	Provided by Prof. Dr. Daniel B. Werz
Gb _{3porc}	Matreya, State College, PA, US
Gb ₃ TT	Provided by Prof. Dr. Daniel B. Werz
GNP	BBI, Cardiff, UK
<i>iso</i> -propanol	Carl Roth GmbH, Karlsruhe, Germany
ITO-slides	Präzisions Glas & Optik GmbH, Iserlohn, Germany
KCl	Sigma-Aldrich, Taufkirchen, Germany
KH ₂ PO ₄	Merck KGaA, Darmstadt, Germany
Methoxy PEG succinimidyl carbonate (5 kDa)	Nanocs Inc., Boston, MA, US
N ₂	Air Liquide Deutschland GmbH, Düsseldorf, Germany
<i>n</i> -propanol	Carl Roth GmbH, Karlsruhe, Germany
Methanol	Carl Roth GmbH, Karlsruhe, Germany
NaCl	Sigma-Aldrich, Taufkirchen, Germany
Na ₂ HPO ₄	Merck KGaA, Darmstadt, Germany
naphthopyrene	TCI Deutschland GmbH, Eschborn, Germany
O ₂	Air Liquide Deutschland GmbH, Düsseldorf, Germany
PageRuler™	Fisher Scientific GmbH, Schwerte, Germany
Polycarbonate membranes	Avestin, Ottawa, Canada
Porous Si ₃ N ₄ substrates	Aquamarijn Micro Filtration BV, Zutphen, Netherlands
SiO	Merck KGaA, Darmstadt, Germany

SM C _{16:0}	Avanti Polar Lipids, Alabaster, AL, US
SM C _{18:0}	Avanti Polar Lipids, Alabaster, AL, US
SM C _{20:0}	Matreya, State College, PA, US
SM C _{22:0}	Matreya, State College, PA, US
SM C _{24:0}	Avanti Polar Lipids, Alabaster, AL, US
SM _{porc}	Avanti Polar Lipids, Alabaster, AL, US
SPR sensor chips (bare gold)	XanTec bioanalytics GmbH, Düsseldorf, Germany
STxB	Provided by Prof. Dr. Daniel Huster
STxB	Provided by Prof. Dr. Winfried Römer
Sucrose	Carl Roth GmbH, Karlsruhe, Germany
TexasRed-DHPE	Sigma-Aldrich, Taufkirchen, Germany
Ti	Elektronen Optik Service GmbH, Dortmund, Germany
Tris	Carl Roth GmbH, Karlsruhe, Germany
Ultra low range marker	Sigma-Aldrich, Taufkirchen, Germany

A.9. Software

Fiji	Schindelin <i>et al.</i> ^[297]
Matlab 2014b	Mathworks, Natick, MA, US
Matlab 2017b	Mathworks, Natick, MA, US
Origin Pro8.5G	OriginLab Corporation, Northhampton, US

A.10. Equipment

BX 51	Olympus, Tokio, Japan
BX 53	Olympus, Tokio, Japan
Coating system MED020	Bal-TEc, Leica, Wetzlar, Germany
Frequency generator Agilent 33220A	Agilent Technology, Santa Clara, CA, US
FluoView 1200	Olympus, Tokio, Japan
Heating chamber	Binder, Tuttlingen, Germany
LEO supra-35 microscope	Carl Zeiss, Jena, Germany
LSM 710	Carl Zeiss, Jena, Germany
LSM 880	Carl Zeiss, Jena, Germany

A. Appendix

MilliQ Gradient A10	Merck Millipore, Darmstadt, Germany
MFP-3D classic	Asylum Research, Santa Barbara, CA, US
Nanowizard 4	JPK Instruments, Berlin, Germany
pH-meter Calimatic 766	Knick, Berlin, Germany
Sputtercoater	Cressington Scientific Instruments, Watford, UK
Plasma cleaner PDC 32 G-2	Harrick Plasma, Ithaca, NY, US
Tip sonifier Sonoplus HD2070	Bandelin, Berlin, Germany
Ultrasonic bath Sonorex RK 255H	Bandelin, Berlin, Germany
Vacuum drying chamber	Binder, Tuttlingen, Germany

Curriculum vitae

Personal data

Name: Jeremias Sibold
Date of birth: 18.04.1990
Place of birth: Donaueschingen, Germany
Citizenship: German

Carreer

2015-2019 **Ph.D. thesis** at the Georg-August University, Göttingen (Prof. Dr. C. Steinem), title of the thesis: *Phase separation of biomimetic membranes: Influence of the substrate adhesion or the glycosphingolipid structure*

2013-2015 **graduate studies** in chemistry at the Georg-August University, Göttingen, degree: Master of Science, grade: 1.8, title of the master thesis: *Mechanical properties of pore-spanning membranes: Influence of osmolarity gradients*, grade: 1.3

2010-2013 **undergraduate studies** in chemistry at the Georg-August University, Göttingen, degree: Bachelor of Science, grade: 1.9, title of the bachelor thesis: *Theoretical study of β -Peptides*, grade: 1.3

2009-2010 **civilian service** at Hofgemeinschaft für Heilende Arbeit e.V., care of disabled people in Khena, Germany

2006-2009 **Allgemeine Hochschulreife** at Merian Schule Biotechnologisches Gymnasium, Freiburg, degree: Abitur, grade: 1.5

Awards

2018 Best Poster Award 2018 1st at the Biennial Meeting of the German Biophysical Society 2018, Düsseldorf, Germany

2017 Travel grant to the 19th IUPAB and 11th EBSA congress in Edinburgh, UK, from the Deutschen Gesellschaft für Biophysik

Scientific contributions

Manuscript

- 2019 **Sibold J.**, Tewaag V., Vagedes T., Mey I. & Steinem C. Phase separation induced by surface adhesion (2019). in preparation.

Peer-reviewed publications

- 2019 **Sibold J.**, Kettelhoit K., Vuong L., Liu F., Werz D. B. & Steinem C. Synthesis of Head Group Labeled Gb3 Glycosphingolipids and Their Distribution in Phase-Separated Giant Unilamellar Vesicles. *Angew. Chem. Int. Ed.* **58**, 17805–17813 (2019).
- 2019 Bosse M., **Sibold J.**, Scheidt H. A., Patalag L. J., Kettelhoit K., Ries A., Werz D. B., Steinem C. & Huster D. Shiga Toxin Binding Alters Lipid Packing and Domain Structure of Gb₃-Containing Membranes: A Solid-State NMR Study. *Phys. Chem. Chem. Phys.* **21**, 15630–15638 (2019).
- 2018 Spindler S., **Sibold J.**, Gholami Mahmoodabadi R., Steinem C. & Sandoghdar V. High-Speed Microscopy of Diffusion in Pore-Spanning Lipid Membranes. *Nano Lett.* **18**, 5262–5271 (2018).
- 2017 Teske N., **Sibold J.**, Schumacher J., Teiwes N. K., Gleisner M., Mey I. & Steinem C. Continuous Pore-Spanning Lipid Bilayers On Silicon Oxide-Coated Porous Substrates. *Langmuir* **33**, 14175–14183 (2017).
- 2017 Patalag L. J., **Sibold J.**, Schütte O. M., Steinem C. & Werz D. B. Gb₃ Glycosphingolipids with Fluorescent Oligoene Fatty Acids: Synthesis and Phase Behavior in Model Membranes. *Chem-BioChem* **18**, 2171–2178 (2017).
- 2017 Schwamborn M., Schumacher J., **Sibold J.**, Teiwes N. K. & Steinem C. Monitoring ATPase induced pH changes in single proteoliposomes with the lipid-coupled fluorophore Oregon Green 488. *Analyst* **142**, 2670–2677 (2017).

Oral presentations

- 2017 CRC803 Autumnschool, Duderstadt
Diffusion of lipids and lipid domains in PSMs and the influence of STxB binding.

Posters

- 2018 CRC 803 Symposium 2018, Göttingen, Germany
Phase separation of sphingomyelin containing lipid bilayers is controlled by lipid-substrate adhesion as well as chain length and saturation
- 2018 Biennial Meeting of the German Biophysical Society 2018, Düsseldorf, Germany
Phase separation of sphingomyelin containing lipid bilayers is controlled by lipid-substrate adhesion as well as chain length and saturation
- 2017 19th IUPAB and 11th EBSA congress in Edinburgh, UK
Pore spanning membranes as a versatile biomimetic tool to study phase separation and lipid diffusion
- 2016 Biomembrane Days, Berlin, Germany
Lipid diffusion of a biomimetic system
- 2016 Biological Dynamics from Microscopic to Mesoscopic Scales, Grimma, Germany
Lipid diffusion of a biomimetic system

Internship

- 08/2008 German Institute of Human Nutrition Postdam-Rehbruecke, Germany

Danksagung

Prof. Dr. Claudia Steinem möchte ich für die Möglichkeit diese Arbeit zu gestalten danken. Ich danke dir auch dafür, dass du es immer geschafft hast, meinen Blick wieder auf den Fokus zu richten, wenn ich mich wieder an Kleinigkeiten aufgehalten habe.

Prof. Dr. Jörg Enderlein danke ich für die Übernahme des zweiten Gutachtens und die fachlichen Diskussionen in den Thesis Committees.

Besonders möchte ich Prof. Dr. Daniel B. Werz, Dr. Lukas Patalag und Dr. Katharina Kettelhoit für die Synthese zahlreicher Gb₃s danken. Dr. Susann Spindler, Reza Gholami Mahmoodabadi und Prof. Dr. Vahid Sandoghdar möchte ich für die iSCAT Messungen danken. Für die Isolation von STxB möchte ich Mathias Bosse und Prof. Dr. Daniel Huster danken.

In diesem Atemzug möchte ich mich auch bei den Masterstudenten Vera Tewaag und Thomas Vagedes, den Praktikanten Julian Meyer, Thomas Vagedes und Fangyuan Liu, sowie der wissenschaftlichen Hilfskraft Loan Vuong für eure Experimente und Datenanalyse bedanken.

Ein besonderer Dank für die zahlreiche Unterstützung im Laboralltag geht an Jutta Gerber-Nolte und Michaela Klingebiel. Danke für die unermüdliche Herstellung verschiedenster Vesikel.

Dem allerbesten Sekretariat, Melanie Sorhage, Marianne Wagener und Dana Sachs, möchte ich für die Unterstützung in den vielen organisatorischen Fragen danken, ich weiss, dass ihr das hier lest.

Natürlich danke ich meiner Familie für die tatkräftige Unterstützung aus dem Schwarzwald. In der näheren Umgebung möchte ich Rebecca dafür danken, dass du immer für mich da warst.

Tja wer umblättert hat einen Vorteil.

Dem gesamten Arbeitskreis möchte ich durch eine verschlüsselte Nachricht danken: `GrosserBuchstabenSalat='olBölüjTsDANKEdenBas MdftaFÜR zAdusDIE Bs SCHÖNEasd kljZEITft\rsdnasdepyxickjrnewrL';fprintf(GrosserBuchstabenSalat([18 16 17 34 60 31 25 21 22 11 8 82 32 3 61 65])); fprintf(GrosserBuchstabenSalat([10 48 78 52 16 51 24 6 62 20 21 13 1 81 77 79 52 25 34 62 30 5 16 9 79 17]));`

DrIngo danke ich nur für die vielen wissenschaftlichen Diskussionen über MATLAB (Spoiler für den Arbeitskreis, vielleicht hilf es euch) und meine Forschung. Ach was solls, natürlich danke ich dir auch für die sonstigen Diskussionen und witzige Augenblicke.

Für die Studienzeit in Göttingen danke ich meinen Kommilitonen und `adH`.